Standalone Wireless Impedance Matching System for Ultra-High Field Magnetic Resonance Imaging

by

Sri Kirthi Kandala

A Dissertation Presented in Partial Fulfillment
of the Requirements for the Degree
Doctor of Philosophy

Approved October 2023 by the
Graduate Supervisory Committee:

Sung-Min Sohn, Chair
Vikram Kodibagkar
Rosalind J. Sadleir
Scott Beeman
Georgios Trichopoulos

ARIZONA STATE UNIVERSITY

December 2023

ABSTRACT

Magnetic Resonance Imaging has become an increasingly reliable source of medical imaging to obtain high quality detailed images of the human anatomy. Application specific coil or an array of coils when placed closely to the anatomy produces high quality image due to the improved spatial signal to noise ratio. Elastic RF coils have been shown to conform to the shape of the patient's body and drastically reduce the gap between coil and anatomy. First, a major challenge faced by these elastic RF coils is the changing impedance condition as the coil takes a different shape for every individual. Next, an area that could benefit from the improved image quality and patient comfort that comes from flexible RF coil design is endorectal prostate imaging.

Demonstrated in the first part of this dissertation is a modular solution to compensate the impedance mismatch. Standalone Wireless Impedance Matching (SWIM) system is an automatic impedance mismatch compensation system that can function independently of the MR scanner. The matching network consists of a capacitor array with RF switches to electronically cycle through different input impedance conditions. The SWIM system can automatically calibrate an RF coil in 3s with a reflection coefficient of less than -15dB resulting in improved Signal-to-noise ratio (SNR) of the sample image by 12% - 24%, based on sample size, when compared to a loaded coil without retuning.

For the second part, we propose a novel elastic and inflatable RF coil integrated with the SWIM system for endorectal prostate imaging at 9.4T. A silicone polymer substrate filled with liquid metal alloy is designed and fabricated with a cavity to create

inflation. This inflatable RF coil is combined with the SWIM system to automatically tune and match after inflating the RF coil for individual levels of inflation. The imaging results have shown a ~10%, ~19%, and ~25 % increase in SNR due to inflation of RF coil at different ROIs in the acquired image.

Overall, the methods proposed and discussed in this thesis are a step towards a new generation of RF coil systems for both existing applications and upcoming ones.

DEDICATION

To my parents K.V.L Narayana and Perina Devi

and

my love Arpitha

ACKNOWLEDGMENTS

Every young engineer is incomplete without a great advisor. I would like to express my sincere gratitude to my advisor Dr. Sung-Min Sohn for his ability, unwavering guidance, and extraordinary patience throughout my research journey. I would also like to thank my committee members for their insightful feedback and constructive criticism. I joined ASU in 2016 as a naïve engineer with an ambition to conduct exacting standards of research and contribute to the RF community. Your support and motivation pushed me to better myself every day.

I would like to thank Magnetic Resonance Research Center (MRRC) and Barrow Neurological Institute (BNI-ASU) for making it possible to evaluate my SWIM system and RF coils. The technical staff Dakota and Alberto at these institutions, respectively, have been instrumental in providing me with a firsthand learning opportunity to gain experience in scanner operations.

I would like to thank my lab partners and friends without whom this journey would be lackluster. During the last 7 years I came across many bright minds who have challenged and redefined my fundamental notion of being an engineer, Zach was one of them. It was a pleasure to collaborate with him not only in building this lab but also laying groundwork for the students to come. I would certainly miss our whiteboard discussions and chess breaks.

Finally, I would like to thank my family: my parents living in India without their encouragement and emotional support I would not embark on this journey and my fiancé Arpitha, who kept my mind sane and my spirits high, without whom I couldn’t have

completed it. I am deeply grateful to all those who have played a role in this endeavor. Your contributions have been invaluable.

त्यक्त्वा कर्मफलासङ्गं नित्यतृप्तो निराश्रय: |
कर्मण्यभिप्रवृत्तोऽपि नैव किञ्चित्करोति स: ||

TABLE OF CONTENTS

Page

CHAPTER Page

LIST OF TABLES

Table Page

LIST OF FIGURES

Figure Page

Figure Page

Figure Page

Figure Page

Figure Page

Figure Page

CHAPTER 1

INTRODUCTION

1.1 Magnetic Resonance Imaging – History and Trends

Initially developed as a tool to study the magnetic properties of the atomic nuclei by physicists Isidor Rabi, Felix Bloch, and Edward Purcell, NMR spectroscopy was further advanced by Paul Lauterbur and Erwin Hahn in the 1940s and 1950s to create two dimensional images of objects [1-3]. In 1971 physicist Raymon Damadian developed the first whole-body NMR scanner to demonstrate the difference between healthy and cancerous tissue [4]. After the commercialization in the mid-1970s, MRI has continuously evolved and significantly contributed to medical research and diagnosis.

Medical imaging is a compelling and invaluable tool in the field of healthcare and medicine that helps with disease diagnosis, monitoring, and treatment. Non-invasive methods like X-Ray, Computer Tomography (CT) scan, and Magnetic Resonance Imaging (MRI), as shown in Fig1-1, are popular due to reduced patient risk and discomfort. MRI is a powerful non-ionizing imaging technique that is used to obtain detailed high-resolution images of soft tissues [8]. In the last few decades MRI has gained much deserved reputation due to its increased availability, introduction of higher field strengths in medical applications, and its ability to integrate with other modalities like CT and Positron Emission Tomography (PET). MRI also offers the ability to see blood flow, cancer metabolism, tissue structure, incorporate functional-MRI (fMRI) with brain structure, and combine Nuclear Magnetic Resonance (NMR) spectroscopy with

imaging [9-11]. This increased utility makes it a beneficial technique for doctors to not only see the physiology but also understand the biological processes.

a) b)

c) d)

Figure 1-1. Picture of a) a clinical MRI scanner [5] b) a preclinical or animal MRI scanner at MRRC-ASU c) an X-ray machine [6] and d) a CT scanner [7]

In the last decade, there has been a movement towards high field and ultra-high field (UHF) MRI scanners for clinical and research applications. The static magnetic field strength B_0 is measured in Tesla (T). 1.5T scanners were replaced with 3T in clinical scenarios in the last decade. And ever since there has been a push for the use of higher

field scanners in clinical imaging. There has been a tremendous effort in research collaborations where scientists, doctors, and industry partners have advanced UHF MRI capabilities and translated the research findings into clinical applications. So, in 2019 the U.S. Food and Drug Administration (FDA) has approved the use of 7T (7T and above are UHF) scanner for clinical applications which opens the way for improved image contrast and higher spatial resolution [12-18]. Some research facilities in the world have installed 9.4T human research scanner and 10.5T animal research scanner to further explore the capabilities of UHF scanners. The most recent breakthrough in this field is the development of a variable field scanner where a single scanner can switch between different field strengths [19] and advancement towards helium free magnets [20].

There has been tremendous progress in the MRI hardware category to reduce the scan time with the help of parallel imaging and compressed sensing, but the effectiveness is limited by signal-to-noise ratio (SNR). Parallel imaging technique uses multiple RF coils with independent RF channels to acquire signal from location of the sample like phased array technique [21-23]. Accelerated signal acquisition from individual RF coils which are later combined to form an image, leads to reduced scan time and improved spatial resolution. SNR improvements have been recorded by using contrast agents, UHF scanners, and flexible/elastic RF coils [24-26]. Surface coils have evolved from rigid to flexible and progressed towards stretchable coils. As the gap between the coil and the body increases the SNR drops. Flexible and stretchable coils can be placed very close to the body or even conform to the shape of the body, this leads to increased sensitivity and thus improved SNR [27, 28]. Advancement in materials and fabrication techniques

allowed us to develop a new generation of receive coils that can bend, stretch, and conform to the shape of the body. Commercial flexible coils until recently were manufactured using flex printed circuit boards (PCB) or very thin standard PCB. This will lead to a very robust mechanical design for the receive arrays but tend to be bulky and heavy. General Electric Healthcare (GEHC) recent breakthrough with AIR^{TM} has created ripples across the MR community with improved patient comfort, enhanced SNR, and reduced scant time [29]. These coil arrays are designed like a blanket covering the complete body part during imaging and allowing to cover hard to reach parts like shoulders and extremities.

But stretching and flexing a coil changes the impedance and frequency of the RF coil drastically [30]. When RF coils do not resonate at the same frequency as the scanner, they do not capture the maximum possible magnetization signal and change in impedance of the coil leads to sub-optimal input impedance presented to the amplifier. Even while using UHF scanners if the RF coils are underperforming in the above-mentioned manner, we observe a negative impact on the SNR of the acquired image. In this dissertation, we propose a standalone wireless impedance matching system that can compensate for the dynamic impedance mismatch issue related to elastic and flexible RF coils. Elastic and stretchable RF coils conform to joints thus improving the SNR in extremity imaging [31]. One area that is yet to benefit from this design of RF coils is endorectal prostate imaging. Therefore, we propose a novel inflatable RF coil using liquid metal, Eutectic-Gallium Indium (eGaIn), to show the feasibility of coil design and improvement in SNR of endorectal prostate imaging at UHF strength i.e., 9.4T.

1.2 Thesis outline

Chapter 1 introduces the history of MRI along with trends in RF hardware design. Motivation for this thesis and research strategy along with the thesis outline are presented here.

Chapter 2 describes the fundamentals of MR physics needed to understand the process of image acquisition. This chapter includes a system level introduction to MRI hardware such as main magnet, gradient coils, RF coils, and basic pulse sequences. Understanding the role of each component helps the reader appreciate the complexities of system level integration and the significance of RF subsystem in creating detailed anatomical images. Lastly, it dives deeper into the RF hardware involved in the transmit and receive chain along with different types of RF coils (antennas in MRI) and discusses the various electrical parameters in validating an RF coil design and performance.

Chapter 3 presents the proposed automatic impedance matching system while evaluating the previously developed systems. It moves towards a detailed circuit level analysis of the proposed system and the modular design. Lastly, the preliminary MR images acquired by using the SWIM system with a rigid copper RF coil are also reviewed along with bench test results.

Chapter 4 details the novel RF coil design proposed for endorectal prostate imaging. Starting with a comprehensive overview of the current elastic RF coil advancements, it moves towards the fabrication procedure of the proposed inflatable RF coil for endorectal imaging and culminates with a discussion of MR images acquired by integrating the inflatable RF coil with the SWIM system.

Chapter 5 summarizes the contribution presented in this dissertation and examines the future of inflatable RF coils integrated with automatic impedance matching system.

CHAPTER 2

BASICS OF MRI

This chapter reviews the fundamentals of MR physics, signal generation, and detection. The physics behind the image formation in MRI is followed up with the different hardware sub-systems that come together to provide a detailed image of the human body. Finally, a detailed review of the RF sub-system is carried out along with RF coil essentials and basic parameters to evaluate the performance of an RF coil to conclude this chapter.

2.1 Fundamentals of MR Physics

Understanding the fundamentals of MR physics is a crucial parameter to analyze MR images, optimize scan parameters to improve image quality, and appreciate the capabilities/limitations of this powerful imaging technique. NMR is the core of MRI, and it involves interaction of atomic nuclei with magnetic fields and RF signals [32-34]. Going back to the concepts of particle physics, fundamental quantum mechanical properties of the nucleus such as Spin (Spin angular momentum, *S*) and precession lie at the core of NMR. Spin is intrinsic to the particle (electron, proton, and neutron) and is one of the two types of angular momentum, the other being orbital angular momentum. The spin is quantized in discrete units, where the magnitude of *S* is given by

Equation 1

$$S = \sqrt{(s(s+1)}\hbar$$

Where *s* is the spin quantum number, which is ½ for electrons, ħ is the reduced Planck's constant.

Spin is 0 if the nucleus has even number of protons and neutrons, Spin is the integral multiple of ½ if the sum of protons and neutrons is odd. The nucleus with non-zero spins have a non-zero intrinsic magnetic dipole moment, $\vec{\mu}$. This magnetic moment is the measure of the strength and direction of the magnetic field generated by the particle intrinsic properties [35]. If we consider the nucleus to be a small magnet, we can approximate the μ of each nucleus as a bar magnet with north-south pole. The magnetic moment is given by

Equation 2

$$\vec{\mu} = \gamma \vec{S}$$

Where γ is the gyromagnetic ratio of the nucleus.

Gyromagnetic ratio represented with γ (gamma) is a fundamental physical quantity. It is a proportionality constant that is isotope-dependent for individual particles. It describes the relation between magnetic moment μ and angular momentum S when the nucleus interacts with an external magnetic field as shown in the above equation. It is given in the units of radians per second per Tesla (rad. s^{-1}. T^{-1}) [36]. Different types of atomic nuclei have different gyromagnetic ratios and some of the popular ones are listed below in Table-1.

Table 1 Some popular nuclei of interest and their gyromagnetic ratios

Element	**Symbol**	**Gyromagnetic ratio [MHz/T]**
Hydrogen	^{1}H	42.58
Deuterium	^{2}H	6.53

Nitrogen	^{14}N	3.08
Phosphorus	^{31}P	17.25
Sodium	^{23}Na	11.27
Oxygen	^{17}O	5.77
Carbon	^{13}C	10.71

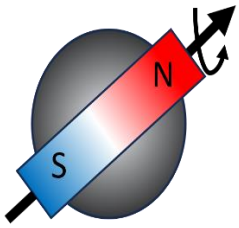

a)

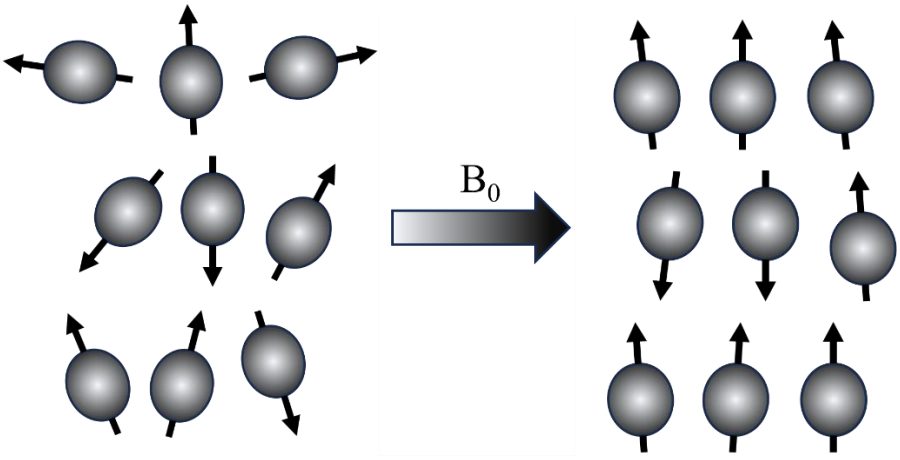

b) c)

Figure 2-1. Pictorial representation of a) a particle rotating along an axis creates magnetic moment (μ) and can be assumed as a tiny bar magnet, b) orientation of spins at thermal equilibrium and c) orientation of the spins after applying an external magnetic field B_0

At thermal equilibrium the spins align themselves in such a manner that there is no net magnetization. However, when an external magnetic field B_0 is applied, they align parallel and anti-parallel to the direction of the field which creates a small net magnetization. The parallel state of the spins requires slightly lesser energy than the anti-

parallel state, thus creating a ratio of 0.999993% parallel to anti-parallel spins [37]. This net magnetization is undetectable due to the constant nature of the static field applied. Therefore, these spins when perturbed by another external magnetic field, perpendicular to the B_0 and at a certain frequency, absorb that energy and get flipped away from the axis of the static magnetic field. Now the spins will precess along the axis of the static magnetic field at a frequency (f_0) called Larmor frequency given by equation below which is proportional to the strength of the static magnetic field B_0 [38].

Equation 3

$$\omega_0 = \gamma B_0$$

Equation 4

$$f_0 = \frac{\gamma}{2\pi} B_0 \, [MHz]$$

Due to γ, some fundamental elements precess at a particular frequency in the presence of an external magnetic field, whereas their isotope counterparts precess at a completely different frequency at same field strength. As most of the human body is made predominantly of ^{1}H, ^{13}C, ^{14}N, and ^{17}O, these particles are of particular interest for MR imaging. ^{1}H or proton has the largest biological abundance at ~63% allowing us to acquire images of soft tissues. Particles such as Phosphorus, Sodium, Carbon, Fluorine etc. are more useful in understanding the biological process when paired with proton imaging [40-45].

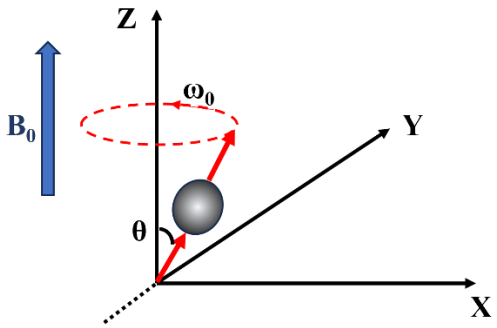

Figure 2-2. Diagram showing the precession of particle along the axis of applied external magnetic field.

The process of flipping the spins is called the RF excitation and the transverse magnetic field is called B_1. Once this B_1 field is removed, the nuclei while precessing around the static magnetic field releases its energy in the process called relaxation to return to its stable state. This net energy released during the relaxation process induces a voltage across an RF coil (Faraday induction) which is then digitized and converted into an image. Bloch equations define the process of excitation and relaxation and the process of detecting the MR signal is explained by Maxwell's equations. Then the Bloch equation in differential form is given as below

Equation 5

$$\frac{d\boldsymbol{M}}{dt} = \boldsymbol{M}(t) \times \gamma \boldsymbol{B}(t) - \frac{\boldsymbol{M}_x \hat{x} + \boldsymbol{M}_y \hat{y}}{T_2} - \frac{(\boldsymbol{M}_z - M_0)\hat{z}}{T_1}$$

At equilibrium

Equation 6

$$\boldsymbol{M}_z = \boldsymbol{M}_0 = \chi \boldsymbol{B_0}$$

$$\boldsymbol{M}_x = \boldsymbol{M}_y = 0$$

Where $\boldsymbol{M}$ is the net nuclear magnetization, M_0 is the net magnetization in equilibrium, and T_1 and T_2 are the relaxation rates. When at equilibrium, the x-y plane spins are randomly oriented out of phase to produce zero net magnetization, but the net magnetization along the z-direction is proportional to proton density, gyromagnetic ratio, and external field strength. Therefore, as B_0 increases the net magnetization M_0 also increases thus increasing the image quality and spatial resolution at higher field strengths. There are two types of relaxations 1) Longitudinal relaxation (T_1) and 2) Transverse relaxation (T_2) [46]. Longitudinal magnetization M_z during relaxation returns to equilibrium of M_0, this rate of relaxation is defined by T_1 as shown below.

Equation 7

$$\boldsymbol{M}_z(t) = \boldsymbol{M}_0\left(1 - e^{-t/T_1}\right)$$

T_2 is defined as the rate at which the transverse magnetization M_{xy} decays to zero and is give below.

Equation 8

$$\boldsymbol{M}_{xy}(t) = \boldsymbol{M}_0 e^{-t/T_2}$$

Both T_1 and T_2 relaxations rates are tissue dependent and play a very crucial role in defining scan parameters to obtain the best possible contrast in the MR image. T1 is also called the spin-lattice relaxation as the interaction of spins with surrounding lattice defines the value of T_1. So, the rate at which the nuclei release the absorbed RF energy to the surrounding lattice is given by T_1 and it is time taken by M_z to reach 63% of M_0 from the equation x. T_2 on the other hand is called the spin-spin relaxation and can be measured as the time taken by the phase of spins in the x-y plane to go 37% out of phase

from original value after the RF pulse is stopped. Give below in table 2 are some of the popular T_1 and T_2 values at 3T for various parts of the body. Taking into consideration the relaxation rates and magnetization vectors, the MR signal that is generated during relaxation can be mathematically written as shown below.

Equation 9

$$\boldsymbol{M}_{xy}(t) = \boldsymbol{M}_0 e^{-t/T_2^*}(\cos \omega_0 t)$$

This signal is called the Free Induction Decay (FID) initially introduced in the NMR study. The T_2^* here is a complex parameter which is based on T_2. T_2^* can defined as the decay of transverse magnetization Mxy to 37% of its original value due to magnetic field inhomogeneities and susceptibility effects [47]. T_2^* is always smaller than T_2. The FID signal or MR signal induces current on an RF coil which is further down converted, digitized, and processed to form an MR image.

Tabel 2 T_1 and T_2 values of some tissues at 3T

Tissue	**3T**	
	T1 (ms)	**T2(ms)**
White matter	832	80
Gray matter	1331	110
Muscle	898	29
Fat	382	68
Blood	1932	275

The electrical interaction between MR signal and MR detector (RF coils) can be defined with the help of Maxwell's equations given below in differential form [48].

Equation 10 - Gauss's Law - electric fields

$$\nabla . \boldsymbol{E} = \frac{1}{\epsilon_0}\rho$$

Equation 11 - Gauss's Law – magnetic fields

$$\nabla . \boldsymbol{B} = 0$$

Equation 12 - Faraday's Law

$$\nabla \times \boldsymbol{E} = -\frac{\partial \boldsymbol{B}}{\partial t}$$

Equation 13 - Ampere-Maxwell Law

$$\nabla \times \boldsymbol{B} = \mu_0 \left(J_0 + \epsilon_0 \frac{\partial \boldsymbol{E}}{\partial t} \right)$$

2.2 MRI hardware

An MR system broadly consists of three major subsystems namely Main magnet and shim coil, Gradient coil subsystem, and RF subsystem. These three hardware pieces are placed in concentric circles with main magnet strength defining the bore diameter. Inside the main magnetic is a shim coil to adjust the uniformity of the B_0 field generated. The gradients are responsible to spatially identify the MR signal in the imaging volume and RF subsystem is responsible to excite the protons and detect the MR signal which is then digitized and processed to form an image. Typically, three rooms are prepared in the hospital or research lab where MRI is being installed. A shielded room that contains a magnet to isolate the magnet and RF coils from any interference from the outside world.

A console room where the patient monitoring system is located along with a scanner console and an expert operates this console system to provide the doctors with required anatomical scans. A third room for electronics is located adjacent or behind the magnet room where cabinets of gradient amplifiers, RF amplifiers, chiller system for cryostat, gradient cooling system, and body cooling system are placed. Let's dive into details of each of the subsystem in the following paragraphs.

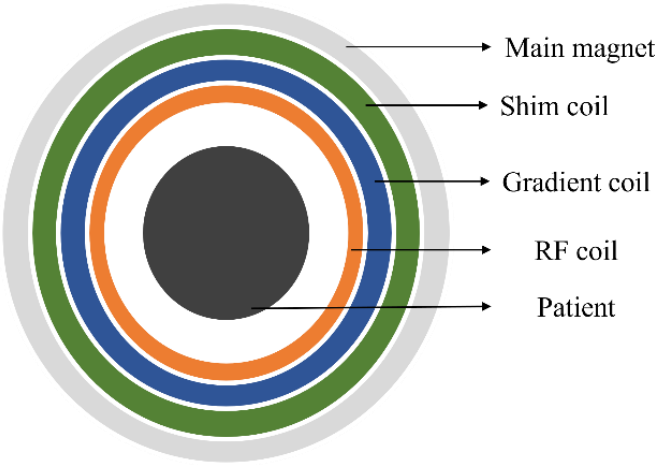

a)

b)

Figure 2-3. a) Cross section diagram of the different hardware parts of an MRI scanner and b) front view of the MRI scanner with cover removed

The main magnet is responsible for generating a strong and static magnetic field B_0 measured in Tesla for example, 1.5T, 3T, 7T, and so on. Various types of magnets are used across the world to generate this B_0, but superconducting magnets are the most popular ones. Superconducting materials are used to create a winding on a former and cooled to 4K (very close to absolute zero) such that the electrical resistance of the material drops to zero [49]. A combination of liquid helium and liquid nitrogen are used to cool the material and maintain the superconducting state. Once the magnet is ramped and the field strength is achieved shimming is done with the help of passive and/or active shimming coils. Shimming adjusts the magnetic field for small deviations and ensures uniformity [50]. Higher field strengths of the static magnetic field lead to better SNR, improved image quality, and increased spatial resolution. But higher field strength magnets come with their own challenges such as susceptibility to wave phenomena and increased RF power deposition [51].

Inside the main magnet is a set of three coils oriented in x, y, and z directions called gradients or gradient coils which help in spatial encoding of the MR signal [52]. These three gradients are orthogonal to each other and are called

1. Slice select gradient
2. Phase encode gradient
3. Frequency encode gradient

The X gradient is responsible for encoding the information from right to left. The Y gradient encodes the information from anterior to posterior direction and the Z gradient encodes information from superior to inferior direction. Gradients generate very weak time varying magnetic fields in the order mT/m with specific strengths and orientations that allows for precise localization of MR signal. This process of spatial encoding helps identify the exact location of the MR signal by identifying the slice and then the x-y pixel location on that slice. The linearly varying gradients in three directions ensure that no point in space (inside the imaging volume) has the same frequency as shown below

Equation 14

$$f_{Larmor} = \frac{\gamma}{2\pi}(B_0 + G_x\, x)$$

G_x is the linearly varying gradient in x direction.

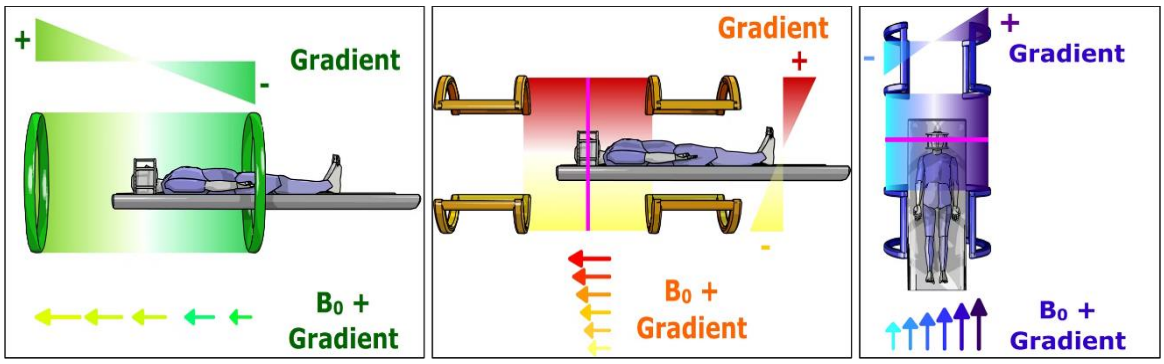

a)

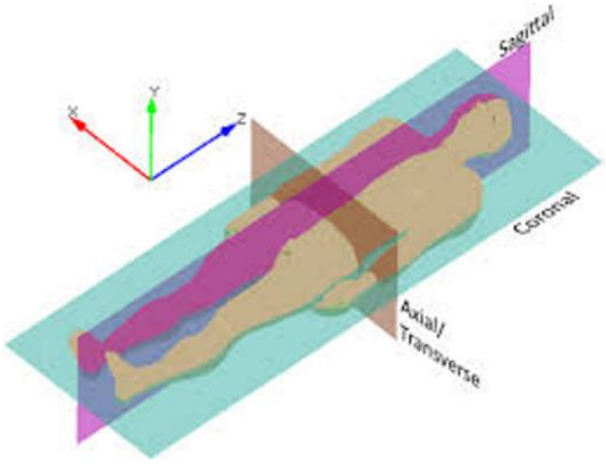

b)

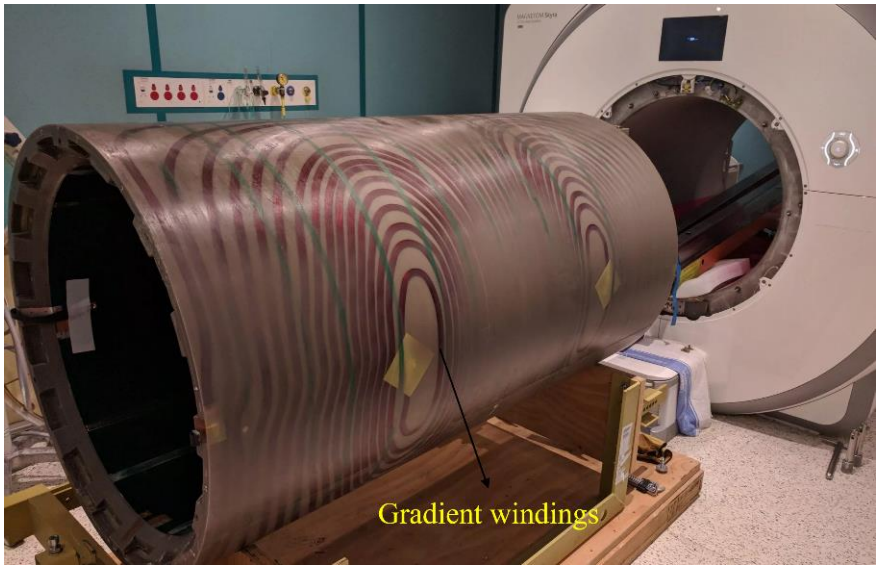

c)

Figure 2-4. a) Pictorial representation of the slice select, freq encode, and phase encode gradient (left to right) [53] b) axial, coronal, and sagittal imaging planes [54], and c) Picture of a gradient coil from Direct Med Parts& Services [55]

When multiple lines of data are connected from a sample in this manner, the resulting 2D data space is called the k-space. This k-space when subjected to inverse Fourier transform gives way to 2D MR images of the body part under imaging. Each of

the x, y, and z gradients are driven by individual power amplifiers. The gradient amplifiers create waveforms in trapezoidal ramp up segments where the timing and amplitude of the gradients are accurately controlled to create spatial encoding. A specific set of RF pulses when applied together with a specific set of gradient pulses (all three gradients) creates a unique imaging protocol called a pulse sequence. This pulse sequence with uniquely defined parameters is designed and applied to the anatomy for specific imaging purposes such as contrast, tissue characterization, and resolution [56].

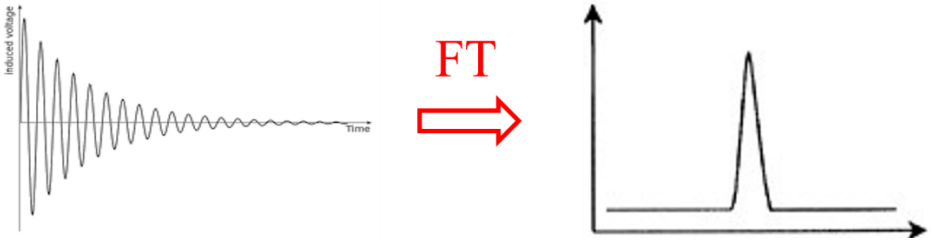

a)

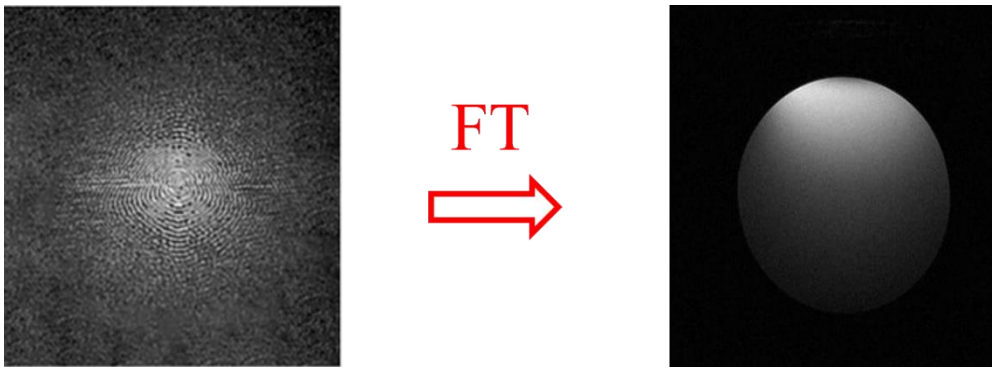

b)

Figure 2-5. a) Diagram showing the process of converting the FID to a frequency spectrum and b) Picture showing the process of constructing an image from k-space

The RF subsystem uses these specially designed pulse sequences that are an interplay of RF pulses and gradient pulses to gather MR data and convert it into images.

MRI uses a similar transmit chain and receive chain in terms of RF electronics to that of wireless communication as shown in Fig 2-6. An RF transmitter generates a signal which is then pulse modulated by the MR console according to imaging criteria. The console defines the duty cycle, timing, amplitude, frequency, and shape of the RF pulse. This is followed by an RF Power Amplifier (RFPA) which amplifies the small RF pulse from mW range to kW range based on the application and RF coil in use. Clinical imaging has strict RF power deposition restrictions based on the body part being imaged. Extremities (legs, wrist, knee etc.) use up to 4kW, head imaging can range from 6-8kW, and whole-body RF coils use a maximum of 30-35kW for whole body imaging. MRI RFPAs are most commonly class AB type multi-stage designs as a fine balance between linearity and efficiency is required. These amplifiers are also supported with power monitoring feedback-based output impedance matching systems to carefully control the amount of RF power deposited into a human body. The amount power deposited, and specific-absorption-rate (SAR) are monitored to keep protect the patient from tissue heating [57-59]. The amplified RF pulse is sent to a transmit RF coil which excites the protons in the region-of-interest (ROI) during the transmit phase.

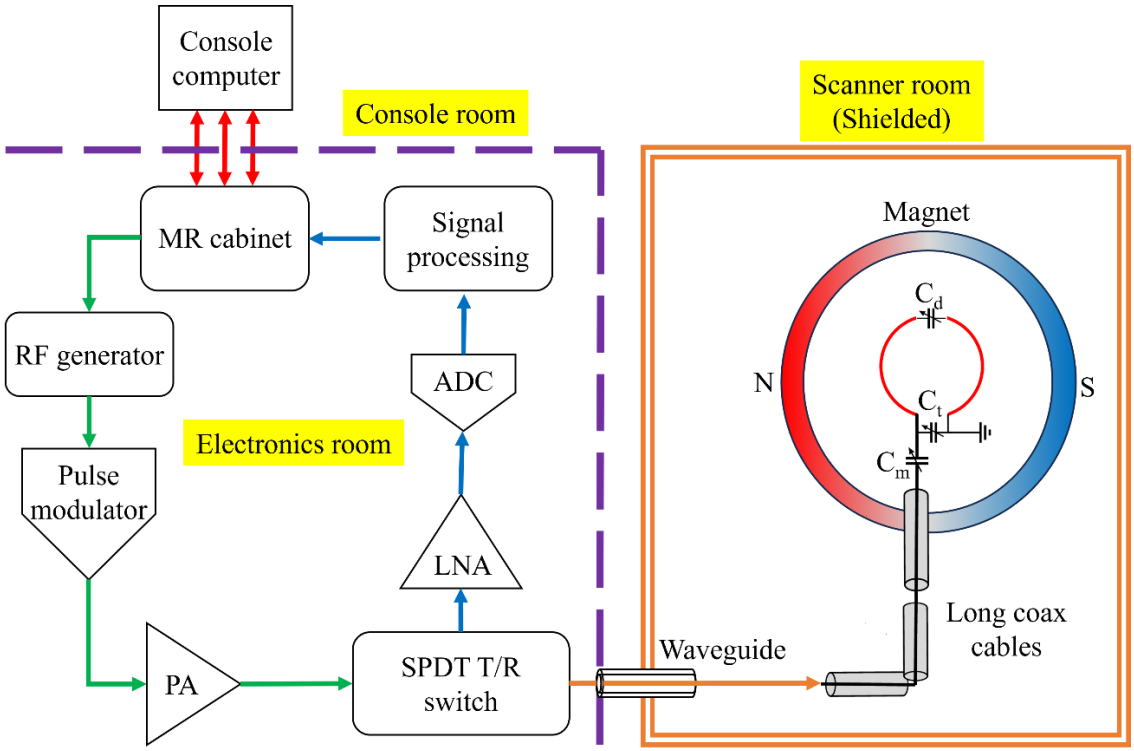

Figure 2-6. Block diagram depicting the MRI with transmit chain and receive chain components necessary to form an image along with floor plan

Once the transmit pulse is stopped, a receive coil detects the MR signal from the ROI. Usually, some type of RF switch is used in this situation if the same coil is being used for reception as well [60-63]. This signal is the uW range which is then amplified using a low noise amplifier (LNA) or a preamplifier. LNAs are now being integrated into the receive coil electronics which improves the SNR and assists in decoupling the coil elements in an array [64, 65]. In recent studies, analog-to-digital converters (ADC) are also integrated on to the coil to maximize the SNR and avoid signal loss and crosstalk when long cables are used to carry the amplified MR signal to receiver in the cabinet room. Also, the availability of advanced ADCs has allowed to perform direction conversion of the MR signal thus bypassing the mixer in the receiver [66, 68]. The

flexible and elastic coils introduced in the last couple of years present a sub-optimal impedance to the LNA as the loading effect changes due to the changing shape of the coil. This creates a loss of signal that cannot be recovered by the LNA. This thesis attempts to provide a solution to this issue by integrating an automatic impedance matching system with the RF coil to compensate for the constantly varying coil impedance.

2.3 Radio Frequency coils

RF coils in MRI play a crucial role in transmitting the RF pulses and detecting the MR signal that will eventually be converted to a detailed image of the specific part of the body. When the RF coil is placed close to the body part being imaged, it creates a secondary local transverse magnetic field (B_1 perpendicular to B_0), it couples and excites the nucleus in that region [65]. After the excitation pulse is removed, the particles release some energy to get back to the stable state. This released energy is the resulting MR signal which is detected by the same RF coil or a different coil. Resulting MR signal is a weak signal by nature, so RF coils are designed in various shapes and sizes to cater for different anatomical applications while considering maximum signal detection and patient safety in mind. RF coils can be broadly classified as Volume coils and Surface coils with different configurations, including arrays in case of surface coils.

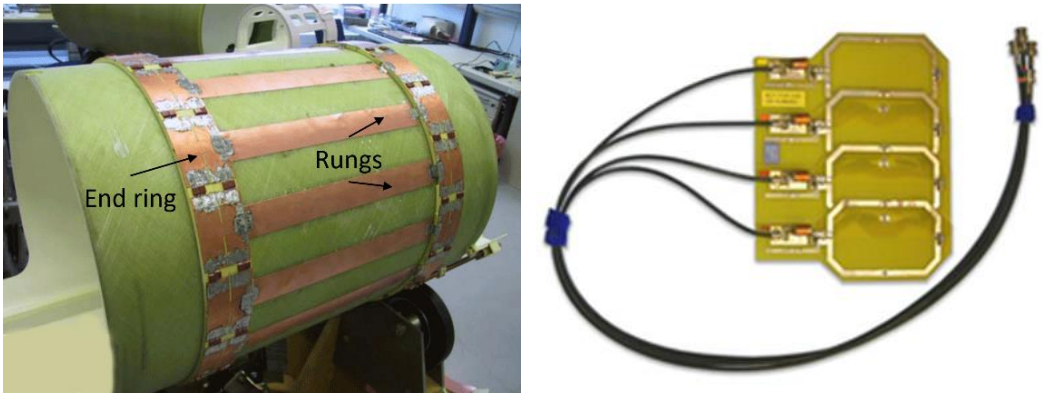

a) b)

Figure 2-7. a) Whole body volume birdcage coil design in high pass configuration b) Phased array coil using 4 loop elements using overlap decoupling technique [68]

A very popular volume coil design is called a “birdcage” coil designed and developed initially by Hayes et al. in 1985 [69]. Birdcage resonator or popularly known as birdcage, is a cylindrical wire mesh design with two major components. Two rings located at the ends of the coil called end-rings relate to multiple “legs” or “rungs”. Capacitors are placed at different locations across the birdcage to create resonant modes leading to three major arrangements 1) Low pass birdcage, 2) High pass birdcage, and 3) Bandpass birdcage. Capacitor placement is key in generating a uniform current which in turn creates homogenous magnetic field. Symmetrically placing capacitors at different locations helps with tuning the frequency of the coil and create uniform currents in the rungs while avoiding formation of standing waves. In low-pass configuration, the capacitors are placed on the end-rings. In high-pass configuration, the capacitors are placed on the rungs/legs of the birdcage. And finally, in band-pass configuration the capacitors are placed on both rungs and end-rings of the birdcage. Sinusoidal current

distribution in the rungs creates different resonant modes in the birdcage coils and many mathematical calculators are developed to help with the design process [70].

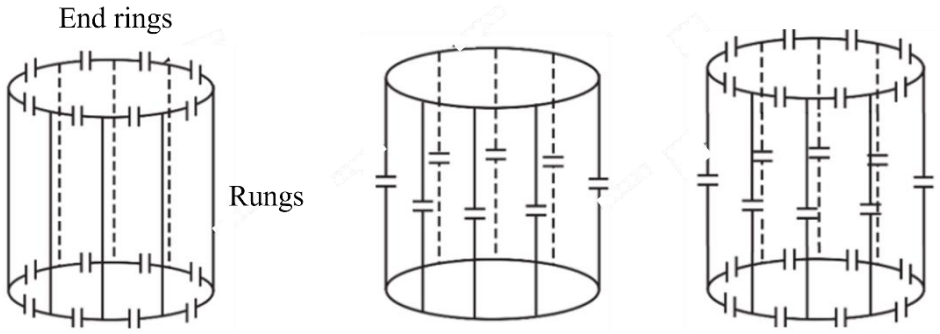

Figure 2-8. Birdcage coil circuit diagram for a) high-pass b) low-pass and c) bandpass configuration [69].

Volume coils are usually used to create a uniform magnetic field around the area to be imaged. They have lesser B_1 field strength and sensitivity compared to surface coil counterparts but can create a very uniform transverse magnetic field. These coils are usually used as transmit coils or transmit-receive coils. Volume coils are also used in quadrature phase scenario more often than linear phase to create a circularly polarization of the magnetic field [71]. Circular polarization techniques help improve the homogeneity of the magnetic field produced by volume coil. Particularly while imaging non-uniform shapes like abdomen, circular polarization helps reduce shadowing artifact and signal dropouts [72, 73]. Circular polarization creates RF signals that are less prone to interaction thus reducing standing waves compared to linear polarization. In the receive mode, it also helps in improving the SNR by a factor of $\sqrt{2}$ thus improving the contrast across large non-uniform anatomies like abdomen and extremities. Volume coils

cane be typically broken down into two types 1) Body volume coil in 1.5T and 3T scanners that are built inside the magnet typically covering the area of torso and head and 2) local volume coils at UHF strengths used for specific applications like head imaging, extremities (knee, wrist, elbow) imaging. UHF scanners do not have body volume coils in used because the wavelength of the RF signal at 7T and above becomes comparable to the size of the anatomy being imaged, called the wave phenomena, making it extremely difficult to acquire high quality images with body coils due to field inhomogeneities [74, 75]. Therefore, local volume coils are used in transmit mode with surface arrays placed closely to improve the SNR. In present day MRI, advanced techniques like parallel imaging along with multichannel array receive coils are combined with birdcage volume coils to improve SNR and reduce acquisition time [76].

Surface coils, as the name suggests, are placed very close to the anatomical surface to acquire maximum signal during reception [77, 78]. These coils are usually designed to image superficial structures in detail as they lack penetration depth into the tissue [78]. Surface coils, also called loop coils, have a very simple structure using a conductor with an impedance matching network to achieve resonance at Larmor frequency. Although lacking in uniformity or penetration depth surface coils provide high sensitivity and SNR thus providing images with finer detail compared to volume coils [79]. Based on the depth of imaging inside the tissue, the size of the coil is fixed which sets the inductance of the loop according to the equation below.

Equation

$$L = R\mu\left[ln\left(\frac{8R}{a}\right) - 2\right]$$

Where R is the radius of the loop, a is the diameter of the conductor and μ is the permeability of the conductor.

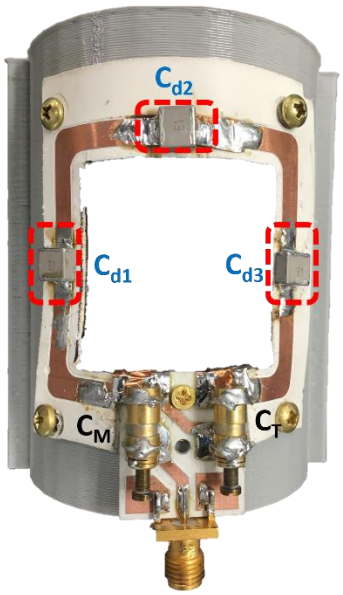

Figure 2-9. Picture of surface coil with 3 distributive capacitors and L-matching network at input milled on printed circuit board

Only 50-75% of the coil diameter is the penetration depth achieved during imaging [80]. Due to their high sensitivity these coils are frequently used as receive coils or transmit-receive coils in MRI. According to Faraday's law, changes in the magnetic flux after RF excitation leads to a very small MR signal, which induces a current in the surface coil placed closely on the patient body. The high sensitivity helps in detecting the microvolts MR signal when using a surface coil [81]. They provide high spatial localization due to smaller size, so they are repeatedly used as an array in receive mode to acquire high quality images. Surface coils are linearly polarized or circularly polarized based on the application but circularly polarized coils with quadrature detection provide a

factor of $\sqrt{2}$ improvement in SNR as the receive component of the MR signal is both directions.

2.4 Coil Impedance and Q factor

Impedance is the measure of opposition an electrical circuit presents to the flow of RF current. It is a complex quantity usually represented by Z and measured in Ohms (Ω). To maximize the energy transfer between the RF source and the load, a special circuit is designed between source and load. This process is called impedance matching. It is crucial to perform impedance matching in MRI to ensure that signal reflections are reduced to a minimum, RF power is transmitted and received in an efficient manner and avoid power loss and signal distortion [65].

Since the loop coil is most inductance with intrinsic amount resistance, the input impedance presented by the loop alone can be marked on the top left corner of the Smith chart. This means that an L-matching topology consisting of two capacitors can be used to tune and match coil to the Larmor frequency [83]. A series capacitor is used to control the frequency tuning of the loop and a shunt capacitor is used to achieve the impedance matching between loop and the receive chain. Widely used in the MRI community, L-matching network with 2 capacitors, the shunt capacitor is used to counter the reactance of the loop and place the impedance point on the unity circle of the smith chart. The series capacitor is used to move the impedance point to the center of the smith chart facilitating a matching condition. No capacitor solely controls tuning or matching as the above-mentioned scenario is describing a dominant behavior. Series capacitor slightly does affect tuning and shunt capacitor impacts the matching in an actual bench test. The

input impedance of the loop coil looking into the L-matching network is given by the equation below.

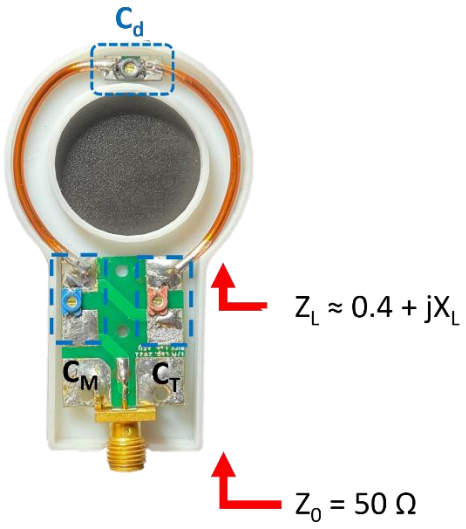

Figure 2-10. Picture of a copper wire surface coil with L-matching network with variable capacitors showing the input impedance at different reference planes

Equation

$$Z_{coil} = \frac{R}{(1-\omega^2 LC)^2 + (\omega RC)^2} + j\frac{\omega L\left[1 - \frac{R^2 C}{L} - \omega^2 LC\right]}{(1-\omega^2 LC)^2 + (\omega RC)^2}$$

As the can be drawn out as an RLC circuit, the following equations can be used to find the theoretical values of the series matching and shunt tuning capacitors used throughout this thesis [65].

Equation

$$\omega = \frac{1}{\sqrt{LC}}$$

Equation

$$\frac{1}{C_m \omega} = Z_0 \sqrt{\frac{r}{Z_0 - r}}$$

Equation

$$\frac{1}{C_t \omega} = L\omega - \sqrt{r(Z_0 - r)}$$

Although we can obtain the values of C_t and C_m through equations mentioned above, usually an iterative process is necessary to reach the required tuning and matching for the coil as (R_{coil}) the coil resistance depends on factors such as positioning, size, and conductivity of the sample under imaging.

Once the coil is tuned and matched to the best possible performance, the very first parameter validating the coil performance is Quality factor or Q-factor (Q). Q factor characterizes the accuracy of the resonance achieved with the coil. It is defined as the ratio of energy stored to energy lost (dissipated) at the frequency of interest [65]. In the case of MRI, the energy stored is the energy of the magnetic field. As the resistance is guided mostly by the coil geometry and material, the energy dissipated is usually resistive loss and specifically for MRI, dielectric loss due to near-field coupling with human body. During bench test with a VNA, the Q is measured as the ratio of center frequency to 3dB bandwidth. 3dB point signifies half power loss therefore a lower Q signifies wider 3dB bandwidth which in turn decreases sensitivity of the coil.

Equation

$$Q = \frac{\omega_0}{\Delta\omega_{3dB}}$$

Q defines the intrinsic peak performance level or efficiency of the designed coil which allows us to predict the maximum possible image SNR achievable (theoretical) by that coil. In an unloaded coil scenario, meaning when the human body is not coupling with the coil, Q can be written as

Equation

$$Q_{unloaded} = \frac{\omega_0 L}{R_{coil}}$$

When the coil is loaded the losses of the sample effect the Q of the coil, also called the loading effect, which is discussed further in the thesis.

Equation

$$Q_{loaded} = \frac{\omega_0 L}{R_{coil} + R_{sample}}$$

The ratio of Q_{loaded} to $Q_{Unloaded}$ is called the Q_{ratio} and is crucial in determining the coil performance.

Equation

$$Q_{ratio} = \frac{R_{coil}}{R_{coil} + R_{sample}}$$

A rule of thumb is to design RF coils with a Q_{ratio} less than 0.2, which means the coil is at peak possible performance when considering radiation loss, resistive loss, and lumped element loss used to build the coil. At this level, the hardware improvements needed to improve coil performance are not necessarily worthy (cryo-cooled receive coils) as the benefit to SNR is marginal. The regime is called the sample noise dominant regime. This is where the loading effect drastically changes the Q of the coil thus notifying the

sensitivity level of the coil. In this regime the sample couples with the coil and absorbs the RF energy induced by it.

SNR is by far the most important parameter in validating any image acquired in MR. Image contrast, spatial resolution, and temporal resolution are all defined by SNR. In simple terms, SNR is the ratio of MR signal detected to the randomly induced noise in the MR environment [84]. The thirst for higher SNR, in the MR community, is something that cannot be quenched. Based on Qratio of the coil, an estimation of the coil efficiency or SNR can be calculated based on equation [78]

Equation

$$SNR = SNR_0 \sqrt{1 - \frac{Q_{loaded}}{Q_{unloaded}}}$$

Where SNR_0 is the maximum available SNR

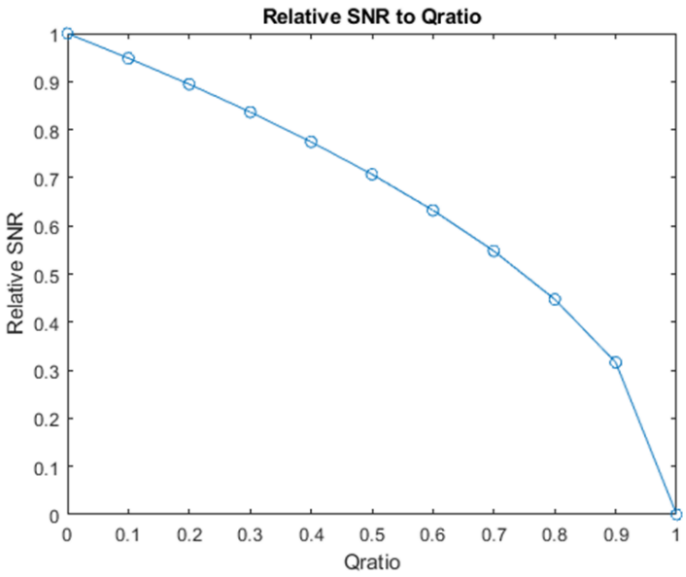

Figure 2-11. Plot of estimated SNR vs Qratio as described by the above equation

In real scenarios, the coil loss can be further examined as radiation loss (R_r) and resistive or Ohmic loss (R_Ω). Therefore, an estimated SNR can be calculated by

Equation

$$SNR \propto \frac{1}{\sqrt{R_r + R_\Omega + R_{sample}}}$$

2.5 Coil decoupling

Decoupling is the process of reducing the interaction between two coils resonating at the same frequency when they are placed close to each other. When multiple RF coils are placed together for an experiment in an array configuration there is electromagnetic interaction between the coils. This interaction impacts the individual coil performance in different thus rendering the array performance subpar. This interaction is called mutual coupling and can lead to crosstalk and reduced sensitivity in certain regions which make that region signal less [65]. Many decoupling techniques have been developed so far by the MR community to maximize array performance [85]. These techniques can be broadly classified as active decoupling and passive decoupling. Active decoupling is incorporated into the coil design with the help of PIN diodes [86]. Based on the bias condition of the diode the coil is either tuned to resonant frequency or detuned at resonance frequency. This method is mostly used to protect receive coils and receive chain components (LNA) from high power RF signal during the transmit phase. Passive decoupling includes overlapping adjacent coils to reduce mutual inductance, adding L/C network between coil elements to reduce the mutual coupling effect etc. [87]. Recent

studies have shown the feasibility of metamaterial structures to improve decoupling between coil elements [88. 89].

For example, in a two-coil system when the coils are individually tuned to resonance frequency of 300MHz and then brought together, the interaction increases with decrease in distance. At the point of maximum interaction, the two coils split their resonant peaks from the center frequency to slightly adjacent frequencies called peak splitting. This creates an “M” shape response in return loss plot of each coil. If they are continued to bring closer at certain point the two coils will go back to initial resonance condition with “zero” interaction between them. The peak splitting disappears, and this point is called the critical overlap distance. At this point the mutual inductance between the coils is perfectly canceled out thus removing any interaction between the coils. But this geometric overlapping gets more and more complex as the number of coil elements increases and arrive at a plateau where another decoupling technique must mix with overlap method to further improve decoupling. Decoupling plays a crucial role in improving B_1 sensitivity leading to better SNR and image quality. It reduces artifacts in the image like shadowing in regions between the coils.

CHAPTER 3

STANDALONE WIRELESS IMPEDANCE MATCHING SYSTEM

3.1 Recent studies – RF impedance matching in MRI

Different samples in a coil change the impedance conditions and this loading effect can be measured by the amount of power reflected to the source. The reflected power measurement is used by a microcontroller to compensate for the impedance change of a coil. Automatic or adaptive impedance matching has been extensively explored in the wireless communication domain for mobile phones [90-94], RFID [95, 96], and in wireless power harvesting [97, 98]. Due to the use of lower frequencies in MRI, most of the hardware is not as compact as in the aforementioned technologies. All components of the MRI system must be non-magnetic; this factor restricts the use of ferrite isolators for measuring the reflected power. Therefore, automatic impedance matching systems in MRI are both expensive and bulky compared to their 5G or RFID counterparts.

Previous investigations in the field of MRI have shown promising development towards an automatic tuning and matching system for RF coils. The necessity for automatic tuning and matching was identified in MRI's infancy [99, 100]. Varactors were used to change the capacitance value to compensate for impedance mismatch [101, 102]. Both magnitude and phase measurement compensation were also introduced in the past by using a 'zero-crossing' technique to find the optimal impedance matching state [103]. A PIN diode-based tuning and matching system was developed for an 8 channel transceive TEM coil using field-programmable-gate-arrays (FPGA) [104]. By simply

retuning the coil, it was observed to restore a majority of the SNR. Frequency detection technique was used in stretchable liquid metal coils to compensate for frequency shift during stretching [105]. Recently, a low-cost automatic system with an Arduino and a phase-locked-loop (PLL) was developed to tune and match an RF coil over a large range of field strengths from 1-23T [106]. Nonetheless, the idea of reading reflected power from the load to tune and match has remained the same for most parts [107-110]. A preliminary study of this work using Arduino Nano and Xbee wireless communication has been reported [111]. An unaddressed issue with existing systems is the lack of real-time monitoring and control by the user. Current systems require synchronization with the MRI console using hardware connection and are designed for specific coils rather than general-purpose system. Also, the systems do not include any type of detuning feature for an RF receive coil. Detuning circuits are essential for a receive coil and most coils are designed with PIN diode or MOSFET detuning circuits. Such coil designs can potentially generate interference causing B_1 field non-uniformity and the required bias for the active devices causes additional noise [112, 113]. To mitigate these concerns, a novel software detuning technique was introduced. With these factors in mind, we have delved further into improving the hardware and software components of existing automatic impedance matching systems for MRI.

3.2 Loading effect

The loading effect is also known as near field /coupling of human body to the transverse magnetic field generated by the RF coils. The loading effect can impact the transmit and receive capabilities of the MRI system and can affect the image quality and

patient safety. When the patient body interacts with the B_1 field generated by the coil, different materials of the human body present different dielectric constants and conductivities. This results in non-uniform field distribution of the transverse magnetic field. Due to the inhomogeneous field, different locations across the ROI can have varying flip angle thus affecting the image contrast. During the receive mode of the MRI, the loading effect can alter the impedance of the coil which changes the resonant frequency and thus impacts the amount of signal detected by the coil. This shows up as varying signal intensity across the image and loss in SNR of the image acquired. Patient safety (SAR) is also influenced by loading effect as it can lead to excessive deposition of RF power in some cases thus causing RF burns in tissue. Understanding the loading effect is crucial in maximizing the benefits of UHF MRI scanners while ensuring patient safety during scans.

The loading effect depends on the size of the patient, anatomy under scan (tissue properties), medical implants etc. Technicians and radiologists consider these factors before initializing the scan parameters. Pre-scan compensation steps include careful patient positioning and use of dielectric pads to create an impedance buffer between coil and the anatomy. A wide range of RF coil designs and shimming techniques are also developed to maintain the field homogeneity. A common technique involves designing coils with lower Q to reduce the impact of loading on the resonance frequency. But the wider bandwidth of the coil's frequency response reduces sensitivity of the coil and in turn the intrinsic SNR of the coil. Apart from the obvious impact on the image quality, the resonance shift causes an increase in the reflected power of the coil. This in extreme

cases can lead to damage of transmit chain components. For example, in a human head scan using ~8kW of RF power, a 10% shift in the resonance frequency equals to -10dB of return loss of the coil. This means ~800W will be reflected to the transmit chain which dissipates as heat. Such large quantities of power cannot be ignored as they lead to lifecycle depletion of the electronics and patient safety issues in extreme cases.

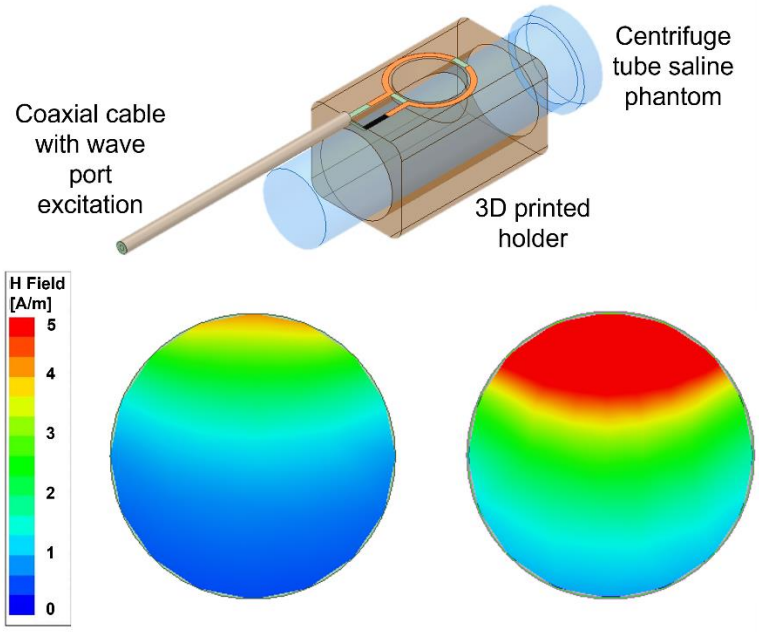

a)

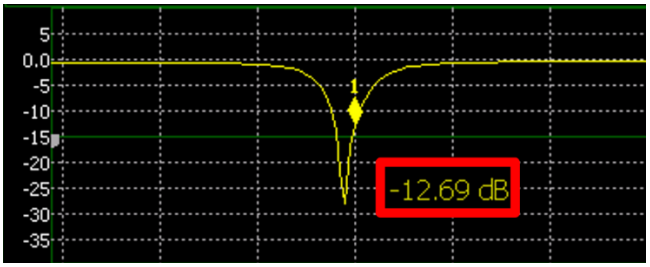

b)

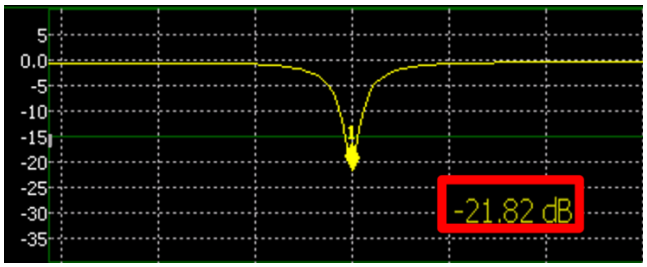

c)

Figure 3-1. a) HFSS simulation of a surface coil with a saline phantom showing the impact of loading on the B_1 field penetration inside the sample b) return loss plot of the surface coil when loaded with saline phantom and c) Return loss plot of the surface coil without saline sample

Low field strengths have lesser impact on the coil resonance compared to UHF scanners. A high Q high sensitivity RF coil is desirable at UHF due to the impact on image quality from wave phenomena. But the loading effect forces the coils to perform at suboptimal levels thus not maximizing the full potential of UHF scanners. Another method adopted by the industry is to estimate the shift in frequency caused by a large set of volunteer studies and design the coil to compensate for the average effect. This pre-calibration technique is a tried and tested method for rigid RF coils but the dynamic of RF coil design has begun to shift.

Recent studies have moved from rigid RF coils to elastic and flexible RF coils that can conform to the shape of the body [ref]. But they present an even bigger challenge as they constantly change the shape, size, and distance between coil and sample by stretching and bending. Now the change in resonance frequency is the result of loading effect and flexible RF coil changing its shape. This makes it extremely difficult to

estimate the amount of shift in frequency beforehand. Advanced RF electronics are continuously being developed to address the impedance mismatch caused by the loading effect and minimize the impact on image quality and patient care [parallel imaging, array coils ref]. As an effort to provide a possible solution to the above-mentioned problem, we propose a fully standalone and automatic wireless impedance matching system that is modular in its design and can be adapted to any UHF MRI at minimum expense.

3.3 Proposed SWIM system

SWIM has a built-in RF continuous wave (CW) signal generation for self-calibration, which makes it completely standalone. SWIM uses the magnitude of reflected power from the coil as feedback to compensate for the impedance mismatch. We also developed a pseudo-manual control of the tuning and matching network to adjust the impedance, irrespective of the automatic feature. Apart from automatic impedance matching function, this pseudo-manual control allows the user to fine-tune the impedance condition after the automatic function. The complete system is wireless and controlled by an in-house developed Android mobile application via Bluetooth. This section discusses in detail the design of RF coil and phantom used in this project, each individual module of the SWIM system, and the android-based application developed to control the SWIM system. The SWIM system consists of one RF input, one RF output, and a DC power supply port. The RF coil is connected to the output of the SWIM system, the RF input is connected to the MRI console, and a 9 V is supplied at the DC port. The android application is loaded on a smartphone/tablet and connected to the wireless controller of the SWIM system via Bluetooth.

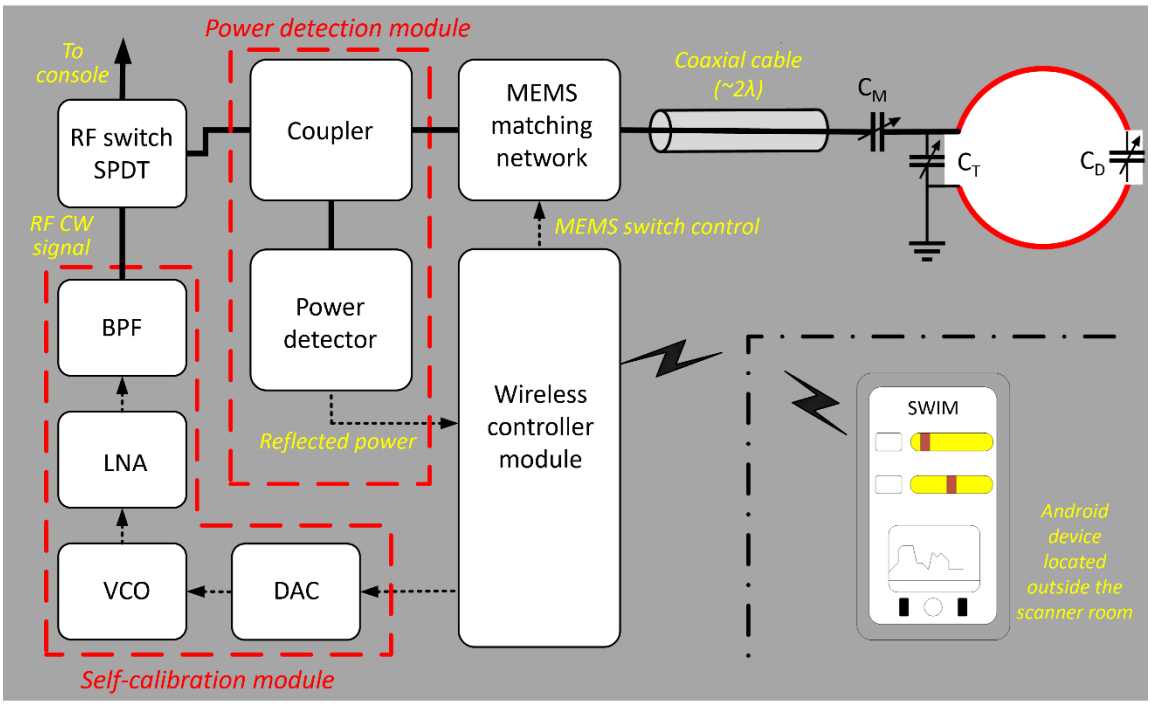

Figure 3-2. Block diagram representing the proposed automatic impedance compensation system with individual modules [113]

3.3.1 Power management

DC power supply to the SWIM system is an integral part of a system level design. Having a separate PCB for DC supply improves isolation between RF and power stages, reduces noise coupling between DC and RF grounds, and reduced ground loops provide overall enhancement of signal integrity for the system. SWIM system is a combination of RF, analog, digital (TTL/LVTTL), and power signals and it is extremely important to design and develop the system in a manner that helps with debugging yet makes it compact. In high-power RF systems, separate power supply PCB helps with thermal management as well. Therefore, we have developed power supply PCB which is connected to either an external DC supply source or a combination of DC supply and

Non-magnetic battery as shown in Fig 3-3. A 9V supply is connected to the low power section of the PCB which is used to supply all the components of the SWIM system. The high-power section is supplied with +/- 25V and 150mA to drive the PIN diodes used all over the SWIM system.

General purpose low-dropout (LDO) regulators ADP7105 are CMOS based adjustable linear voltage regulators which can provide outputs in the range of 3.3V to 20V, with a maximum current of 500mA. Ultralow-noise RF linear regulator ADM7150, is another CMOS based adjustable linear voltage regulator that can output 4.5V to 16V, with a maximum current of 800mA. The outputs of all the LDOs are adjustable using resistive divider circuits that are user adjustable. These LDOs are also equipped with TTL based enable option so that any number of regulators can be turned on/off using the microcontroller. This feature allows to further reduce low frequency (hum) DC noise during imaging mode.

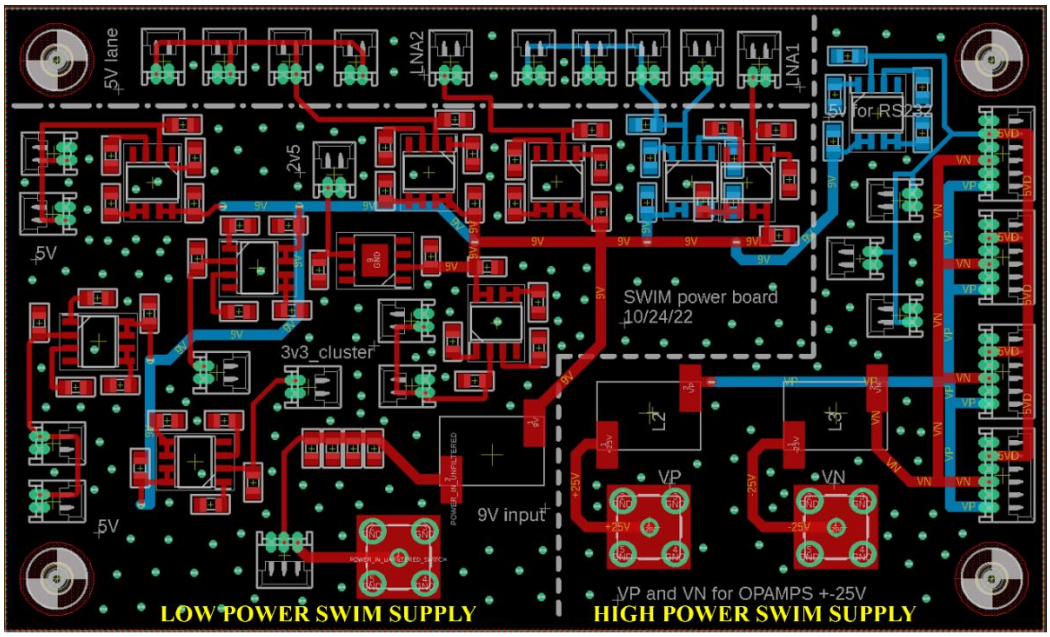

Figure 3-3 Eagle layout of the power supply board for SWIM with low-power and high-power inputs

3.3.2 Standalone Module

The standalone module is designed to provide the SWIM system with its own RF signal generation capability in a single or multi-channel scenario. A Voltage Controlled Oscillator is used to generate RF continuous wave (CW) signal and then passed through a low noise amplifier. This signal is then sent down through a Chebyshev band-pass filter to remove any harmonics and get it ready to use for calibration. This module consists of a VCO (CVC055CW-250-450, Crystek Crystal Corp., USA) which can generate a CW RF signal in the range of − 3dBm to +3dBm, with a typical output of 0dBm. VCOs offer a wide range of tunability in terms of frequency along with smooth control over the tuning range. Due to the modular nature of the proposed SWIM system the ability to tune between field strength allows this system to be standalone. Although used for CW signal generation in this case, VCOs allow for rapid frequency modulation making the SWIM system suitable for an open-source platform where the user can modify and improve individual modules for specific applications. VCOs also have lower phase noise thus sending out a signal that has better signal quality and spectral purity. These VCOs designed specifically for MRI applications are low cost making it easy for replicating the SWIM system.

The VCO used in this project requires a 5V DC supply with 12mA current for optimal operation making it a very low power consumption device. It has a tuning range of 0.3V to 4.7V across the frequency thus making it a perfect device to be controlled

using two individual digital-to-analog converters (DAC) (MCP4725, Microchip Technology, USA). These are 12-bit DACs that allow precise control over the tuning frequency as shown below. The VCO has a sensitivity of 50MHz per 1V tuning. 61kHz per bit can be achieved with this setup giving a very fine-tuning control over the standalone module frequency, as shown below.

Equation

$$\frac{5V}{2^{12}} = V_{step} = 1.22mV$$

$$f_{step} = Tuning\ sensitivity\ X\ V_{step}\ (kHz)$$

$$f_{step} = \ 50\ X\ 1.22 = 61\ kHz$$

Using a DAC to power up the VCO allows the user to completely switch off the signal which can interfere with MR signal during the imaging process and cause RF leaking artifacts. The microcontroller used inter-integrated circuit (I^2C) serial protocol to interact with the DACs, which set up the supply and tuning voltages for the VCO.

The RF signal is then followed by an E-pHEMT (Depletion mode High-Electron-Mobility-Transistor) low noise amplifier (SAV-331+, Minicircuits, USA) to amplify the signal by 22.3 dB. This model combines high gain with extremely low noise figure, resulting in lower overall system noise. The unit comes housed in a tiny 4-lead SOT-343 package. This model requires external biasing and matching which is designed using Keysight ADS (ADS). A non-linear model library of the transistor was obtained from Modelithics and installed in ADS as shown in fig 3-4 a). Bias point is VDS=4V; IDS=60mA is chosen in the class-A operation range of the I-V curve. Of the many techniques available to stabilize an amplifier, we are using RC-feedback design to stabilize

single stage LNA in this thesis. Feedback circuits are the best way to reduce instability issues and increase bandwidth at the same time, a common practice in MMIC design. For board level design this technique may reduce the gain in a single stage design, but this is a trade-off that is worth making. The stability of the preamp is measured using the μ-μ' technique. After a couple of iterations between different bias points to achieve a balance between power consumption and gain of the preamp, impedance matching was performed using Gain circles (Gacirc) and Noise circles (Nscirc) as shown in fig 3-4 b) and c). Finally, fig 3-4 d) display the achieved gain of 22dB, noise figure of 0.56dB with P1dB of 19dB. The impedance points selected for input and output matching are shown in Fig 3-4 e).

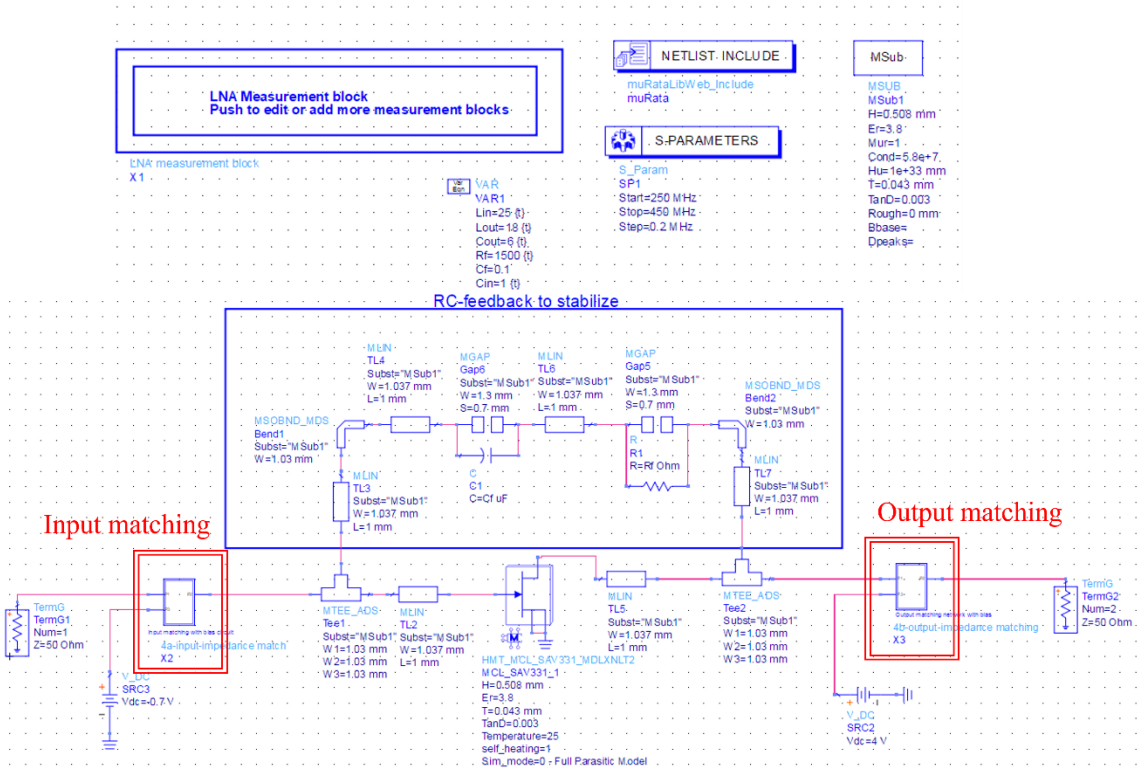

a)

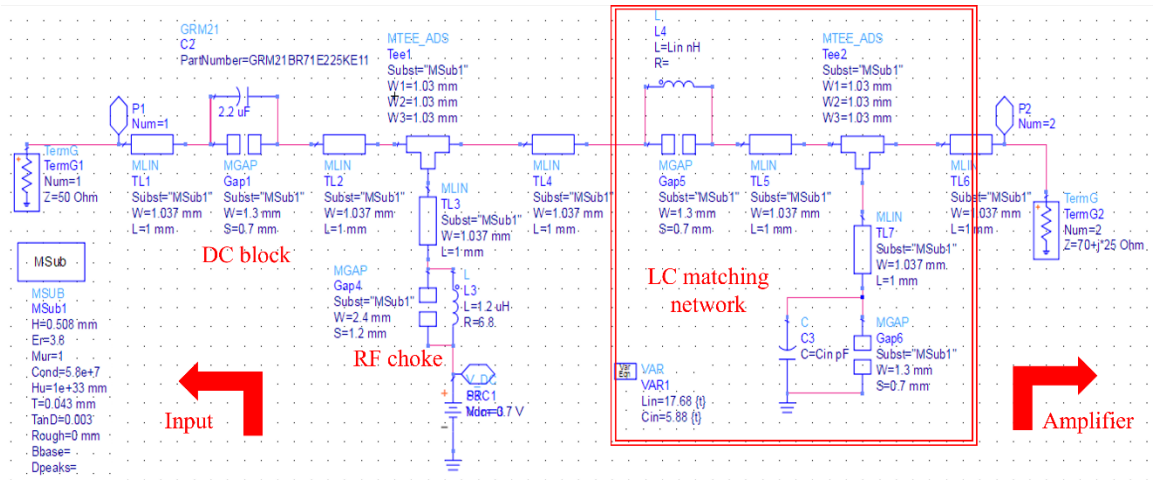
GRM21
C2
PartNumber=GRM21BR71E225KE11
2.2 uF
MTEE_ADS
Tee1
Subst="MSub1"
W1=1.03 mm
W2=1.03 mm
W3=1.03 mm
L
L4
L=Lin nH
R=
MTEE_ADS
Tee2
Subst="MSub1"
W1=1.03 mm
W2=1.03 mm
W3=1.03 mm
P1
Num=1
P2
Num=2
TermG
TermG1
Num=1
Z=50 Ohm
MLIN
TL1
Subst="MSub1"
W=1.037 mm
L=1 mm
MGAP
Gap1
Subst="MSub1"
W=1.3 mm
S=0.7 mm
MLIN
TL2
Subst="MSub1"
W=1.037 mm
L=1 mm
MLIN
TL3
Subst="MSub1"
W=1.037 mm
L=1 mm
MLIN
TL4
Subst="MSub1"
W=1.037 mm
L=1 mm
MGAP
Gap5
Subst="MSub1"
W=1.3 mm
S=0.7 mm
MLIN
TL5
Subst="MSub1"
W=1.037 mm
L=1 mm
MLIN
TL7
Subst="MSub1"
W=1.037 mm
L=1 mm
MLIN
TL6
Subst="MSub1"
W=1.037 mm
L=1 mm
TermG
TermG2
Num=2
Z=70+j*25 Ohm
MSub
MSUB
MSub1
H=0.508 mm
Er=3.8
Mur=1
Cond=5.8e+7
Hu=1e+33 mm
T=0.043 mm
TanD=0.003
Rough=0 mm
Bbase=
Dpeaks=
DC block
MGAP
Gap4
Subst="MSub1"
W=2.4 mm
S=1.2 mm
L
L3
L=1.2 uH
R=6.8
RF choke
LC matching
network
VAR
VAR1
Lin=17.68 {t}
Cin=5.88 {t}
C
C3
C=Cin pF
MGAP
Gap6
Subst="MSub1"
W=1.3 mm
S=0.7 mm
Input
Amplifier

b)

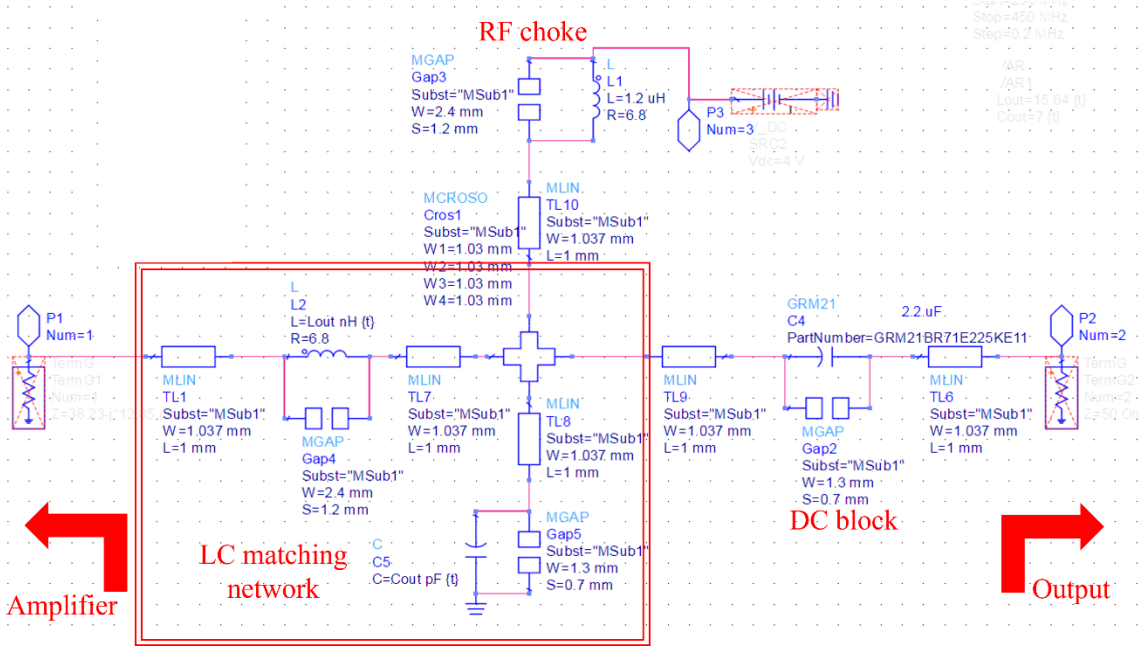
RF choke
MGAP
Gap3
Subst="MSub1"
W=2.4 mm
S=1.2 mm
L
L1
L=1.2 uH
R=6.8
P3
Num=3
MCROSO
Cros1
Subst="MSub1"
W1=1.03 mm
W2=1.03 mm
W3=1.03 mm
W4=1.03 mm
MLIN
TL10
Subst="MSub1"
W=1.037 mm
L=1 mm
P1
Num=1
L
L2
L=Lout nH {t}
R=6.8
MLIN
TL1
Subst="MSub1"
W=1.037 mm
L=1 mm
MLIN
TL7
Subst="MSub1"
W=1.037 mm
L=1 mm
MLIN
TL8
Subst="MSub1"
W=1.037 mm
L=1 mm
MLIN
TL9
Subst="MSub1"
W=1.037 mm
L=1 mm
GRM21
C4
PartNumber=GRM21BR71E225KE11
2.2 uF
MLIN
TL6
Subst="MSub1"
W=1.037 mm
L=1 mm
P2
Num=2
MGAP
Gap4
Subst="MSub1"
W=2.4 mm
S=1.2 mm
MGAP
Gap2
Subst="MSub1"
W=1.3 mm
S=0.7 mm
DC block
LC matching
network
C
C5
C=Cout pF {t}
MGAP
Gap5
Subst="MSub1"
W=1.3 mm
S=0.7 mm
Amplifier
Output

c)

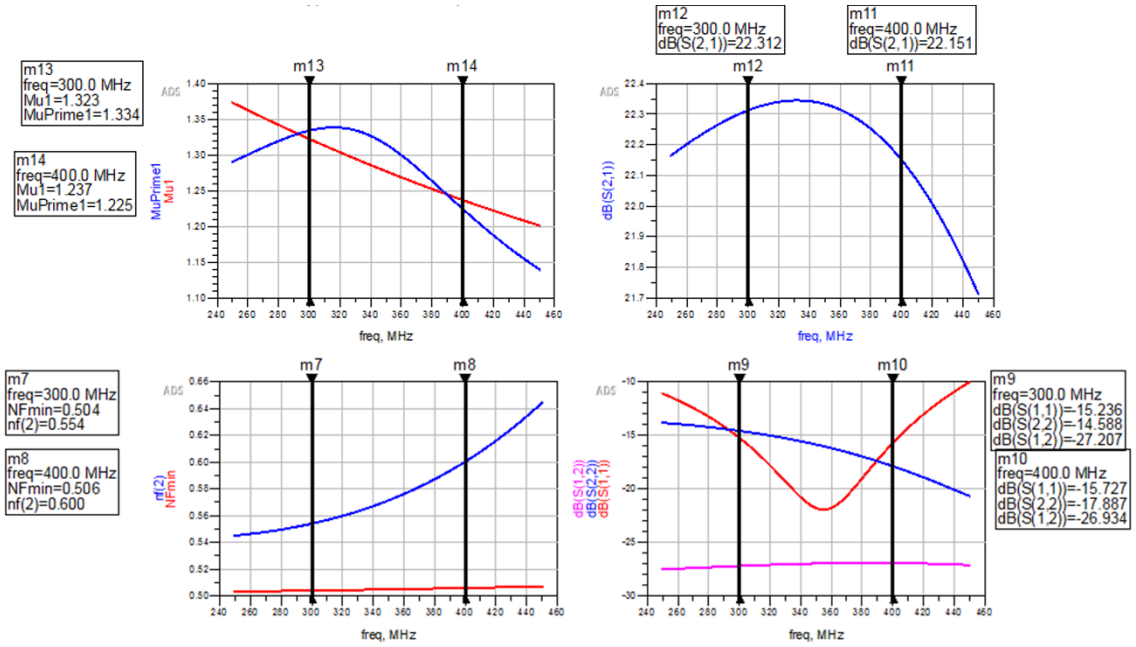

d)

NoiseMatch[m1_freq_index]	Zin1[m1_freq_index]	MaxGain1[m1_freq_index]	PwrGain1[m1_freq_index]
64.738 - j28.219	44.178 - j4.984	22.627	22.333

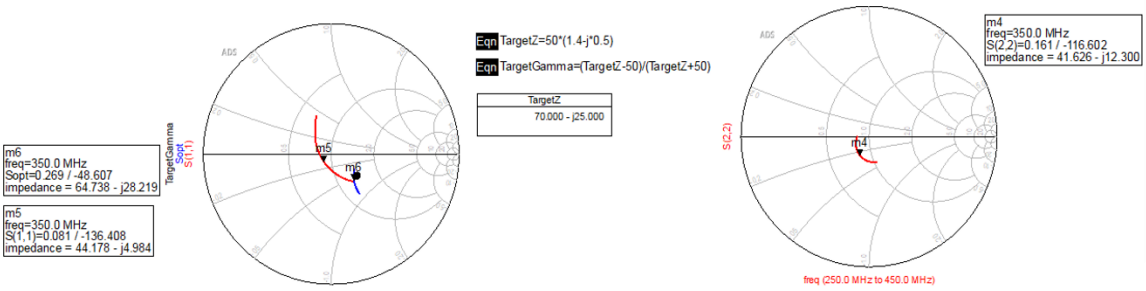

e)

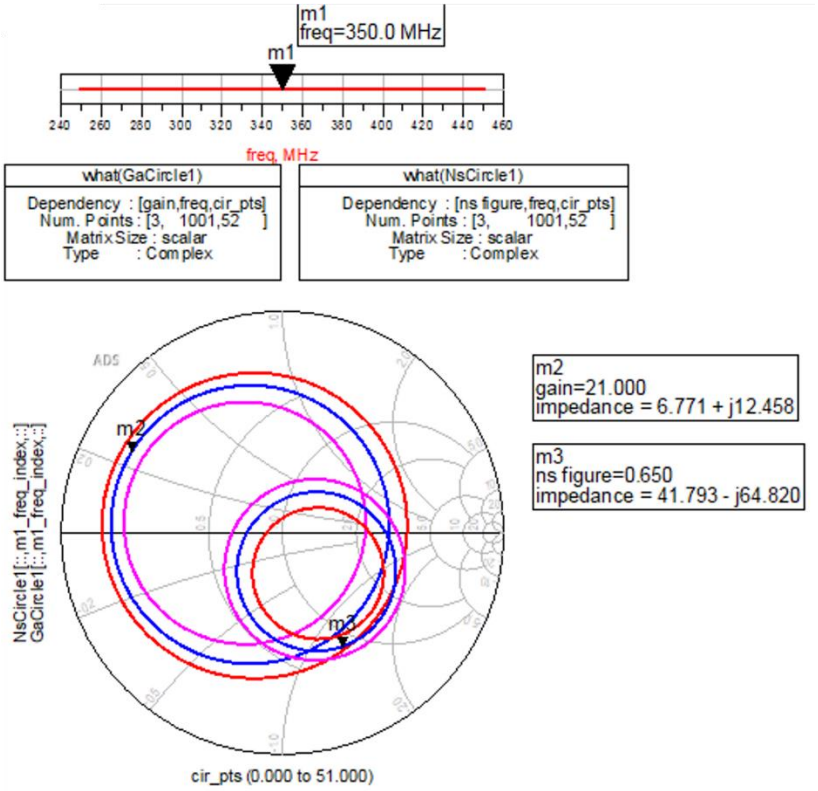

f)

Figure 3-4. LNA design in ADS b) input matching network c) output matching network and d) Results displaying gain, insertion loss, return loss for input and output, noise figure and stability of the LNA e) dataset and smith chart displaying the optimal impedance point for noise match at input f) Picture of noise circle and gain circles with "what" function displaying the achieved gain and noise figure after matching.

Complete designed parameters achieved for the preamp are mentioned in Table 3. A narrow band pass filter, designed in-house, was used as the next stage to filter out low frequency noise and higher harmonics from the VCO along with any mixer non-linear products from preamp. The lumped element filter was designed to have a 74 MHz bandwidth at center frequency of 300 MHz. A Chebyshev band-pass design with 3rd order

design is opted here because of the sharp roll off it provides after the stopband compared to other filters of same order. Finally, Chebyshev filters always require fewer components compared to other filters of same order leading to compact, cost-effective design with high selectivity. The schematic of the Chebyshev filter and its results are shown in fig 3-5 a) and b) respectively.

Table 3 Measured parameters of the designed preamp compared to a commercially available LNA

Target		**Traditional preamp**	**Achieved**
Freq	250-450MHz	1-1000MHz	250-450MHz
V_{dd}	<=5v	5V	4V
I_{ds}	<100mA	140mA	60mA
Gain	>20dB	22.5dB	22dB
NF	<1dB	1.1dB	0.56dB
S_{11}	<-15dB	-17dB	-11dB
S_{22}	<-15dB	-18dB	-12dB
Rev isolation	<-25dB	-26.1dB	-27dB
P1 dB	>16dB	24dB	19dB
IP3	>30 dBm	40dBm	32dBm
Power consp	<1W	3.3W	246mW

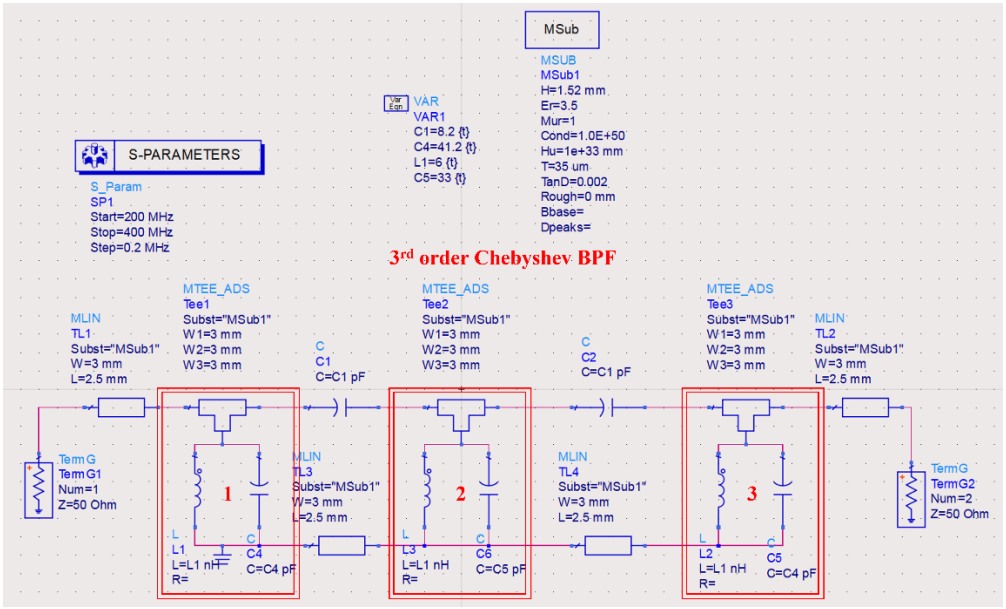

a)

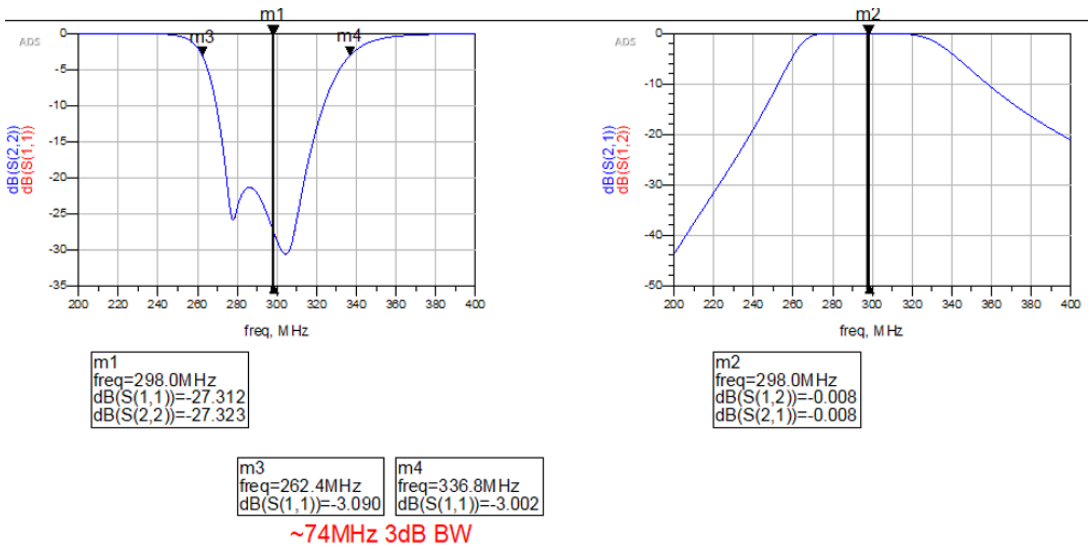

b)

Figure 3-5. a) Chebyshev Band-pass filter 3rd order design schematic in ADS and b) S-parameter results of the filter

The standalone module (PCB) layout design is shown in Fig 3-6 a) which shows that by swapping the VCO and filter, the complete board can be changed from 7T operation to 9.4T operation. These parts have the same footprint in layout with the same pin structure making it extremely modular and easy to replicate the design between different field strengths. The output of the standalone module is a sinusoidal CW RF signal measured at 19.47dBm or 5.95V Pk-Pk, as shown in Fig 3-6 b) and the adjacent channel power is measured at ~-61.7dBc making the calibration signal very linear and less prone to intermixing products as shown in Fig 3-6 c).

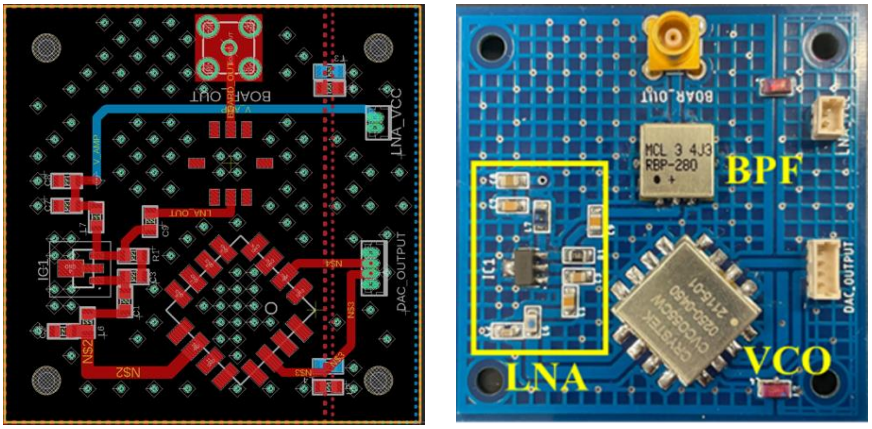

a)

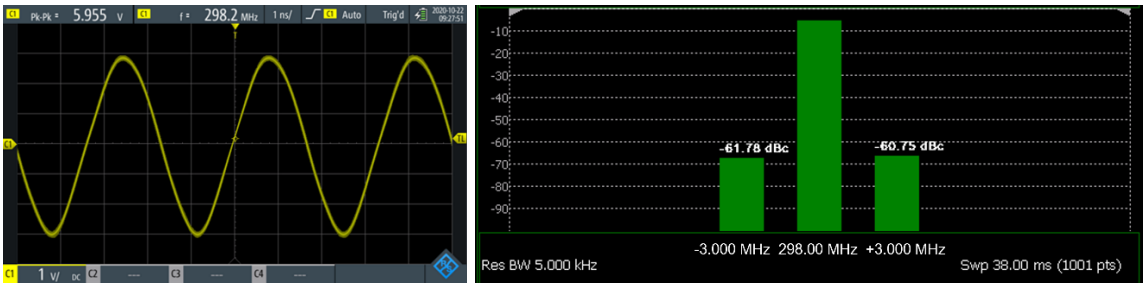

b) c)

Figure 3-6. a) PCB layout (left) and picture (right) of the standalone module that generates the RF CW signal required for calibration b) output of the CW signal as

measured in oscilloscope and c) adjacent channel power measurement of the output using power meter along with a VNA.

The filtered signal is then passed down to the RF single pole double throw switch. This switch toggles between the receive chain of the MRI for imaging and the impedance matching system for tuning and matching.

3.3.3 RF Switch Design

An RF switch between MR console, RF coil, and the SWIM system is the most crucial part of the design which makes the SWIM system standalone. Certain specific electrical characteristics are required for this switch to make the SWIM system efficient and cost effective. In switch terminology, a “pole” is the number of channels it can control at the same time and is represented by the number of channels that are named “common” or “COM”. Similarly, a “throw” is the number of connections or positions it switches to/between. Therefore, switch design in RF is usually named as number poles and number of throws for example, a switch with one COM port and two switching ports is called a Single-Pole-Double-Throw (SPDT). In this thesis the low-power SWIM system uses a CMOS based RF SPDT switch, and the high-power SWIM system uses a custom designed highly-isolation PIN diode based SPDT RF switch as described in the following sections.

An SPDT CMOS RF switch (HSW2-272VHDR+, Minicircuits, USA) was used to switch the receive coil between MRI console (connecting to the receive chain LNA) and self-calibration module. The “pole” or RF common (RFC) port is connected to a bidirectional coupler and the two “throw”, RF1 (port1) is connected to the MRI console

and RF2 (port2) is connected to the self-calibration module, as shown in Fig 3-7 a) and b). This switch offers high linearity with + 85 dBm 3rd order intercept point, low insertion loss, and internal CMOS driver, making it a perfect fit for low power impedance matching system. Insertion loss and isolation data of the switch were characterized at 300 MHz as 0.20 dB (RFC-RF1), 0.29 dB (RFC-RF2), and 41.56 dB (RFC-RF1/RFC-RF2) respectively, as shown in Fig 3-7 c) and d). After the SWIM function, the switch will toggle to a slightly lower insertion loss path and the input impedance presented to the console can be fine-tuned wirelessly via the mobile application if necessary.

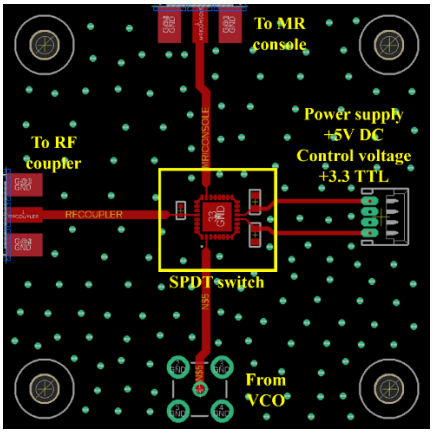

a)

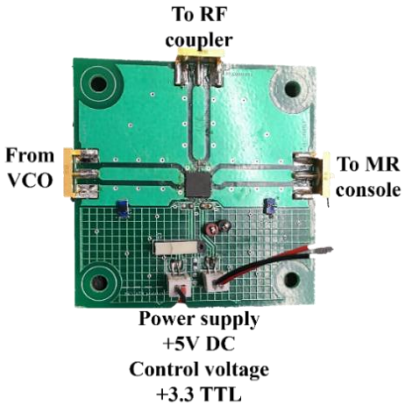

b)

c)

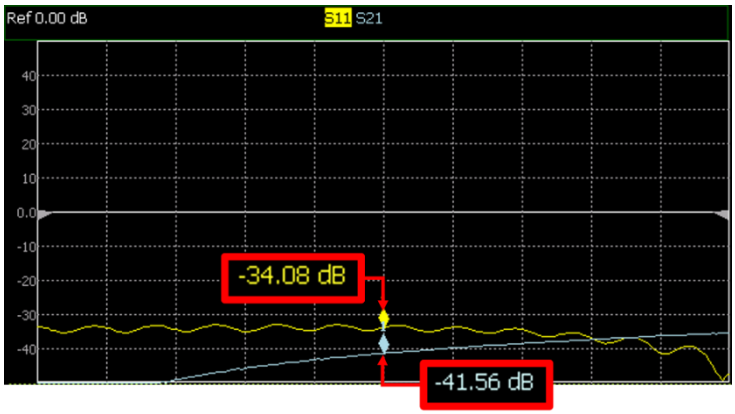

Channel isolation

d)

Figure 3-7. a) PCB layout of the low power SPDT RF switch b) Assembled SPDT RF switch with Molex control pins c) Measured insertion loss of the switch and d) Measured isolation of the switch at 298MHz

The high-power capable PIN diode switch is designed using four non-magnetic PIN diodes (MA4P7470F-1072T, MACOM). This RF SPDT switches between MR console and SWIM system thus making it a key piece of the puzzle. The diode configuration for SPDT is chosen in such manner to maximize the isolation between RF paths and maintain linearity in outputs. The configuration of the diodes is shown in Fig 3-8 a) and b) also indicating the bias points for the complete switch. This PIN diode arrangement also allows the use of only two bias voltages for 4 diodes thus reducing complexity, power consumption, and avoids a simultaneous high-impedance state for both RF paths.

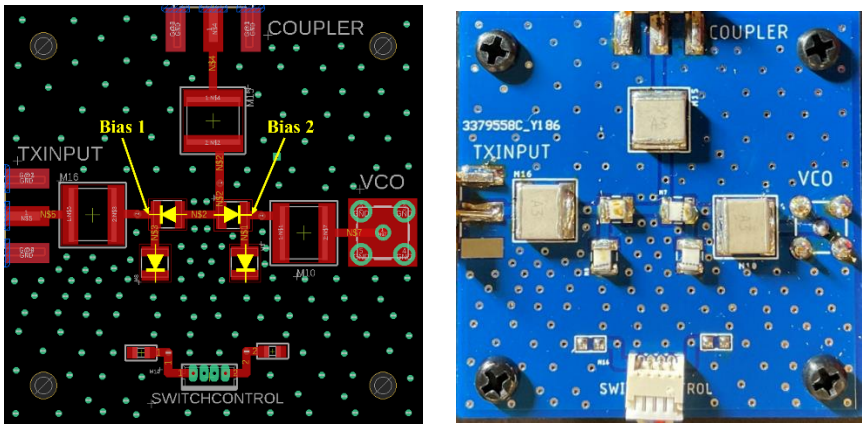

a) b)

Figure 3-8. a) layout of the PIN diode SPDT RF switch and b) assembled PCB with 4x MACOM PIN diodes

The bench test results of the high-power switch are detailed here as shown in Fig 3-9 detail the insertion loss of each RF path (RFC-RF1; RFC-RF2) when they are switched ON, isolation between each path when they are switched OFF, and finally the output signal from both paths to understand the magnitude and phase variations (for a same input signal). RFC to RF1 has an insertion loss of 0.118dB at the center frequency and an isolation of >40dB over a span of 40MHz from center frequency, as shown in Fig 3-9 a), b). Similarly, RFC to RF2 has an isolation of 0.225dB at center frequency and a channel isolation of >29dB over the span of 40MHz from center frequency, as shown in Fig 3-9 c), d).

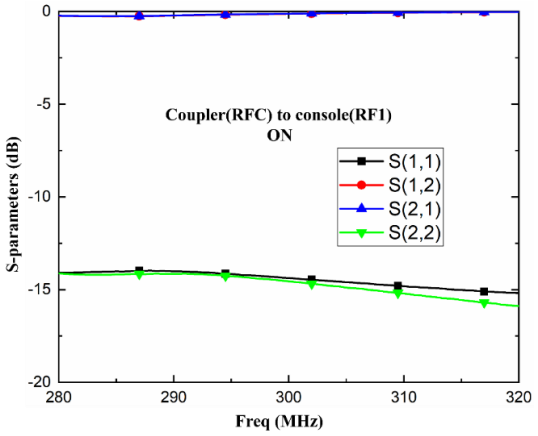
Coupler(RFC) to console(RF1)
ON
S(1,1)
S(1,2)
S(2,1)
S(2,2)
S-parameters (dB)
Freq (MHz)

a)

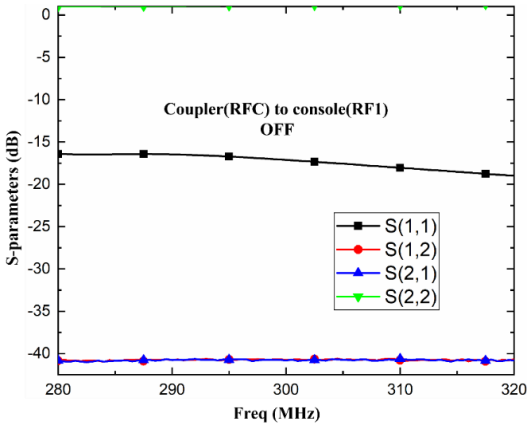
Coupler(RFC) to console(RF1)
OFF
S(1,1)
S(1,2)
S(2,1)
S(2,2)
S-parameters (dB)
Freq (MHz)

b)

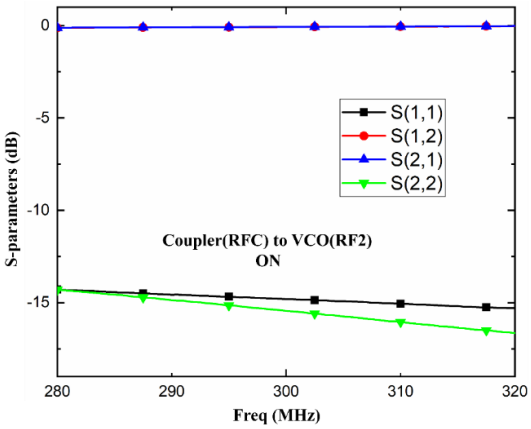
Coupler(RFC) to VCO(RF2)
ON
S(1,1)
S(1,2)
S(2,1)
S(2,2)
S-parameters (dB)
Freq (MHz)

c)

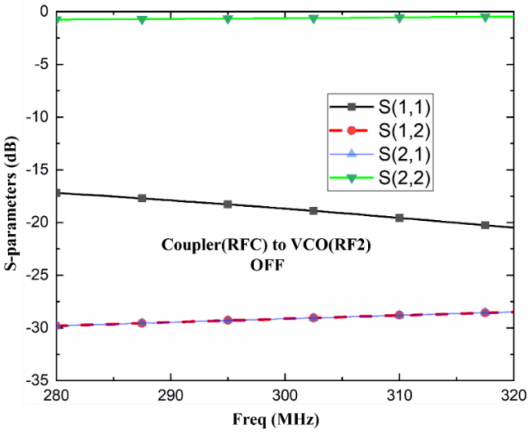
Coupler(RFC) to VCO(RF2)
OFF
S(1,1)
S(1,2)
S(2,1)
S(2,2)
S-parameters (dB)
Freq (MHz)

d)

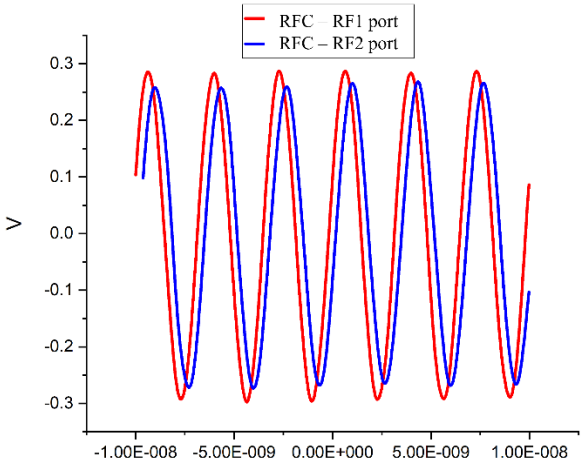
RFC – RF1 port
RFC – RF2 port
V

e)

Figure 3-9. S-parameter plot measured using VNA a) Insertion loss between RFC-RF1 (console) b) Isolation when turned off between RFC-RF1 c) Insertion loss between RFC-RF2 (VCO) d) Isolation when turned off between RFC-RF2 (VCO) and e) measured output from the both RF1 and RF2 with a sinusoid (300mV pk-pk) as input at RFC.

Sinusoid output from both ports of the low power RF switch is measured using an oscilloscope to understand the change in insertion loss between ports. Varying transmission coefficient between calibration port and imaging port may vary the impedance presented by the coil and invalidates the effort of the automatic impedance matching system. In Fig 3-9 e) the measured outputs from both ports (RFC-RF1) (RFC-RF2) are plotted with 300mV pk-pk sine signal as input to the RFC port. As seen, there is a very minute change between individual path insertion loss magnitude and phase. Therefore, a more lossy path is chosen for the calibration mode and lesser loss path will aid in maintaining the calibration impedance values. Also, RF1 has more isolation allowing user to use more Tx power that can protect the SWIM system. The RF switch connecting the Tx path has >40dB isolation and the LNA on the standalone board provide >25dB reverse isolation, thus provide >65dB of total signal isolation between Tx MRI pulse and low-power SWIM system components.

3.3.4 Power Measurement Module

To read and measure the reflected power magnitude and phase when there is an impedance mismatch in the RF coil, a device capable of taping RF power and required. Then another device capable of converting this high frequency signal to DC output is needed so that ADC conversions can be applied to that data and computations can be

performed by the microcontroller. Usually in the wireless communication industry, circulators are employed for this job. Circulators allow signal flow in one direction either clockwise or anti-clockwise depending on the design and use a ferrite core material to achieve this property along with its high isolation. In MRI, this is not possible as ferrous materials cannot be used inside the scanner room.

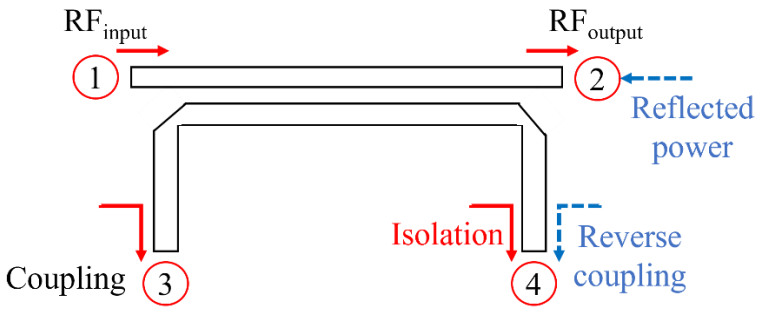

Figure 3-10. Block diagram of a bidirectional coupler with port functions

Therefore, a clever way of taping the reflected power is to use a bi-directional coupler between the transmit signal and RF coil. Couplers have very low insertion loss; they do not drastically affect the transmit signal. Couplers are 4-port devices with input port, output port, forward coupling port, and reverse coupling port. As the names suggest, the input port is where the signal is applied, and the output port is the exit for the signal. This path usually has the least insertion loss and can be adjusted in the design phase. There are two coupling ports, these are basically ports that tap the energy from the main path via the transmission line coupling process and make that sampled RF power available for user operations. The coupling factor is what decides the amount of power being tapped from the main line. Forward coupling port or coupled port is when a sample input signal entering is taped and presented here. A reverse coupling port or isolation port

is the Rport that has maximum isolation from the input port. But any signal entering the output port in the opposite direction (reflection) get coupled to the isolation port. As a reciprocal device the same coupling factor applies for both input coupling port and reverse coupling port [114].

Equations

$$Coupling\ factor\ (dB) = 10\ log\left(\frac{P_3}{P_1}\right)$$

$$Isolation\ (dB) = 10\ log\left(\frac{P_4}{P_1}\right)$$

$$Directivity\ (dB) = Isolation - Coupling\ factor$$

$$= 10\ log\left(\frac{P_4}{P_1}\right) - 10log\left(\frac{P_3}{P_1}\right)$$

$$Directivity\ (dB) =\ 10\ log\left(\frac{P_4}{P_3}\right)$$

Directivity is the difference between isolation of coupler and its coupling factor. A high directivity coupler, for a fixed coupling factor, has very high isolation. Hence, higher directivity is considered a virtue in coupler design as it reduces the ability for transmit signal to corrupt the very small (microvolts) reflected power signal. Especially in MRI applications, as the transmit power in the order of kilowatts, a higher directivity increases the sensitivity of the coupler to detect small changes in the impedance of the RF coil.

For low-power SWIM system a bi-directional coupler (ADCB-20-82+, Minicircuits, USA) is used to tap the reflected power. This device has a low measured insertion loss of 0.334 dB, 20 dB of coupling at both ports, and a directivity of 30 dB at

300 MHz. By terminating the forward coupling port with a 50 Ohm resistor, an accurate reflected power measurement can be conducted.

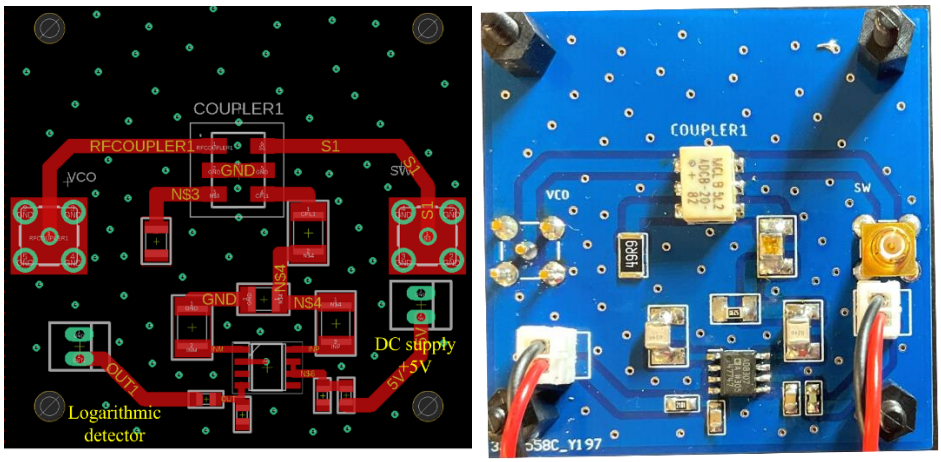

a) b)

Figure 3-11. a) Eagle payout of the power measurement module and b) assembled PCB with Bi-Di coupler and power detector

To accurately measure the reflected power using a bidirectional coupler, high directivity is required. Directivity is defined as the ability of the coupler to differentiate between forward and reverse signals. For a given coupling factor over a bandwidth lower directivity means lower isolation between input port and reverse coupling port. This leads to signal leakage from input port to the reverse coupling port which combines with the coupled reflected power signal. As the coupled reflected power is a very small signal, a high directivity is necessary to reduce the input leakage signal at the reverse coupling port. Microstrip lines suffer from poor directivity due to inhomogeneous dielectric material leading to different phase velocity of the odd and even mode. Various compensation techniques for microstrip coupled-line couplers were established to enhance the directivity [115-121]. Directivity and bandwidth are inversely proportional

to each other. In MRI this can be used to an advantage, due to the narrow band operation, to create even higher directivity. Feedback compensation is a simple yet effective way to improve directivity [122]. The proposed system utilizes a lumped element feedback compensation technique to increase the directivity, introduce tunability, and reduce the overall size of the coupled-line coupler, as shown in Fig 3-12. By connecting a trimmer capacitor (NMKM10HV, Voltronics, USA) between collinear ports, an isolation zero is generated due to the feedback. The reactance of the lumped element defines the frequency of isolation zero therefore, a trimmer capacitor allows the user to fine tune the directivity of the system. Closed-form equations were used to calculate the value of the feedback capacitor for 300 MHz and Keysight ADS was used to perform circuit level simulations. Carefully placing the shunt feedback capacitor between the two collinear ports will maintain the impedance of the coupled line, but slight variation in the coupling factor was observed during bench test. This can be compensated by adjusting the spacing between lines, if needed.

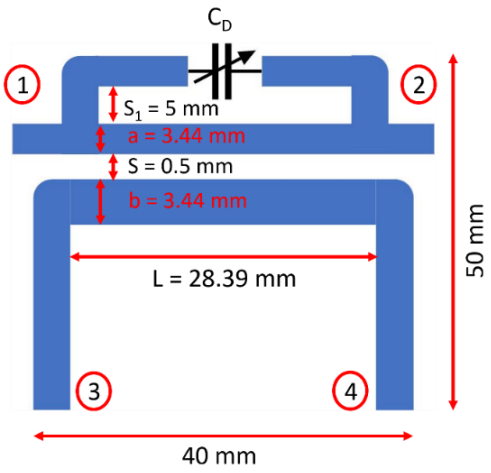

Figure 3-12. Proposed high directivity coupler with capacitive feedback.

Equation

$$\begin{bmatrix} Y_{11} & Y_{12} \\ Y_{21} & Y_{22} \end{bmatrix}_{odd} = \begin{bmatrix} \frac{cos\theta}{jZ_{0o}sin\theta_o} + j\omega C_d & \frac{-1}{jZ_{0o}sin\theta_o} - j\omega C_d \\ \frac{-1}{jZ_{0o}sin\theta_o} - j\omega C_d & \frac{cos\theta}{jZ_{0o}sin\theta_o} + j\omega C_d \end{bmatrix}$$

Equation

$$\begin{bmatrix} Y_{11} & Y_{12} \\ Y_{21} & Y_{22} \end{bmatrix}_{even} = \begin{bmatrix} \frac{cos\theta}{jZ_{0o}sin\theta_e} + j\omega C_d & \frac{-1}{jZ_{0o}sin\theta_e} - j\omega C_d \\ \frac{-1}{jZ_{0o}sin\theta_e} - j\omega C_d & \frac{cos\theta}{jZ_{0o}sin\theta_e} + j\omega C_d \end{bmatrix}$$

Y_{odd} and Y_{even} are converted to their corresponding S-matrices and the combined S matrix of the compensated coupler is given as follows.

Equation

$$S_{11} = \frac{1}{2}(S_{11}^e + S_{11}^o)$$

Equation

$$S_{12} = \frac{1}{2}(S_{12}^e + S_{12}^o)$$

Equation

$$S_{31} = \frac{1}{2}(S_{11}^e - S_{11}^o)$$

Equation

$$S_{41} = \frac{1}{2}(S_{21}^e - S_{21}^o)$$

As the idea of the lumped element feedback compensation is to create an isolation null, we can calculate the C_d value by satisfying $S_{41} = 0$. The connecting points of the feedback circuit to the original coupled line must be chosen carefully to maintain the characteristic impedance and keep the insertion loss to a minimum. Isolation zero refers to infinite directivity of the theoretical coupler, therefore the exact value of the capacitor obtained will result in slight variation of the coupling factor. This can be adjusted either by

correcting for the gap between the coupled lines or by tuning the variable capacitor as shown in Fig 3-12.

High directivity improves the ability to measure reflected power accurately without leakage from the transmit signal. Thus, improving the sensitivity of the system to slight impedance changes. A four-port VNA (Keysight 9370A, Keysight, USA) was used to gather the s-parameters of the coupler at 300 MHz with a 40 MHz bandwidth. The proposed high directivity coupler with directivity tuner is fabricated on a RO4003 substrate (ε = 3.55) and AD8307 magnitude detector is used to gather load impedance data as shown in Fig 3-13 a). In Fig 3-13 b), the measured insertion loss of the main line is measured 0.05 dB which is comparable to conventional coupler at 0.334 dB. A translucent rectangle marks the region of particular interest in MRI due to its narrow band operation. A maximum isolation of 90 dB was achieved at the center frequency with a minimum of 65 dB throughout the bandwidth as shown in Fig 3-13 c). The minimum measured directivity in this region is 35.4 dB with a maximum of 62.23 dB at the center frequency, as displayed in Fig 3-13 d). The measured coupling factor at the center frequency is 26.57 dB with a 0.8 dB coupling flatness. After validating individual modules, reflected power measurement data for various VSWR conditions was gathered using an oscilloscope to compare the results to a conventional coupler as displayed in Table 4. An RF coil tuned and matched to 50 Ω is connected to the port 2 of the coupler and port 1 is connected to the VNA. With the input power from the VNA known from the settings, reflected power is calculated based by intentionally changing the VSWR from 1.12 to 5. Once the target VSWR was achieved a high-power amplifier is connected to an

RF source to amplify the CW signal generated (19dBm) by 45dB and then reflected power is measured again.

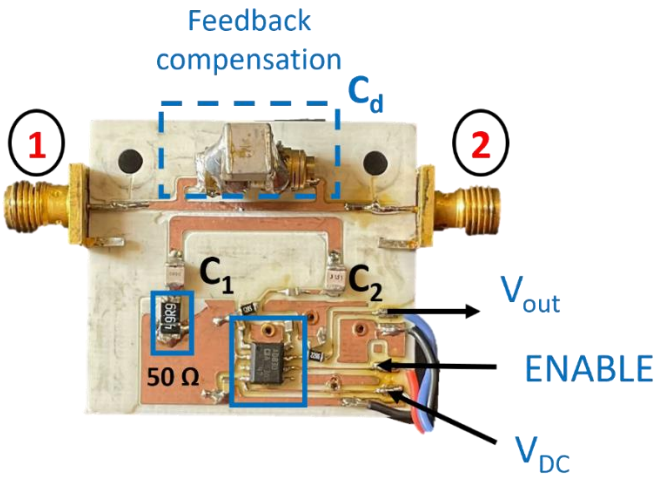

a)

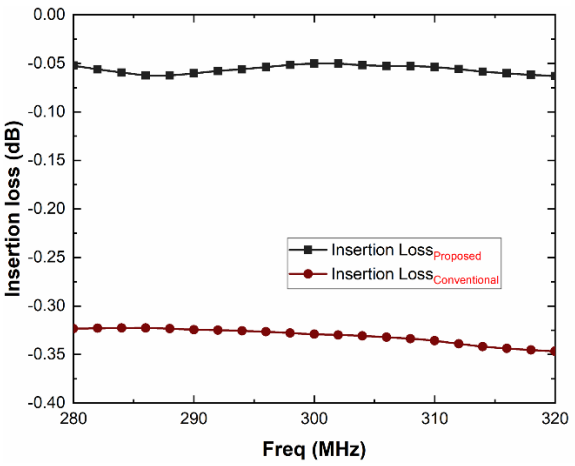

b)

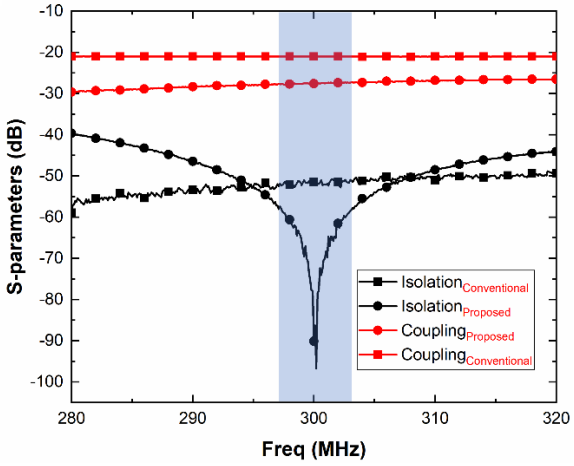

c)

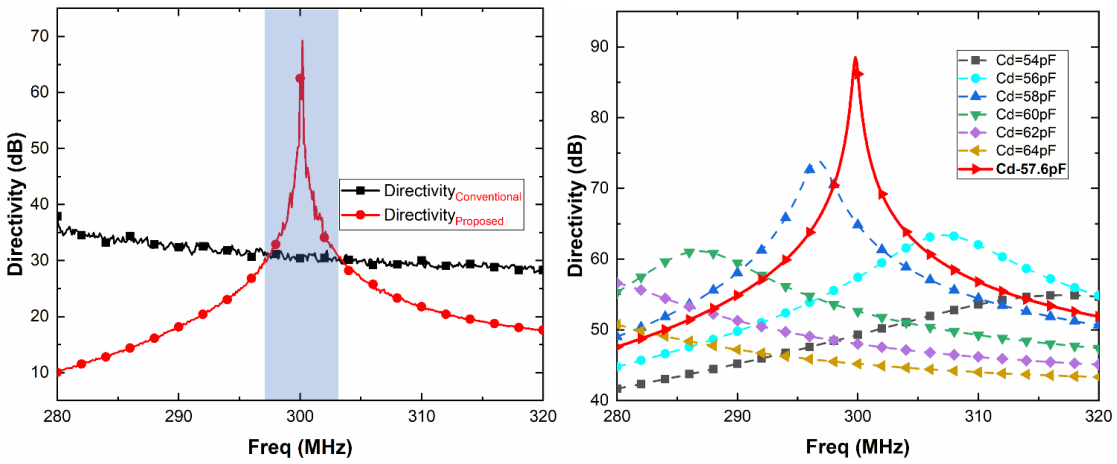

d) e)

Figure 3-13. a) Picture of the designed high directivity coupler b) measured insertion loss of the coupler c) Measured Isolation and coupling with the help of 4 port VNA d) Measured directivity of the proposed coupler compared to commercially available and e) Directivity plot varying the feedback capacitor value in ADS

AD8307 is a logarithmic amplifier capable of measuring RF power with a large dynamic range. Output ranges from 0.4V to 2.5V. Reflected power was measured using a logarithmic amplifier-based RF power detector (AD8307, Analog Devices, USA). The amplifier uses a progressive compression technique with 6 amplification stages. A narrow-band input matching at the frequency of interest also helps in better signal sensitivity along with a certain amount of frequency selectivity.

Table 4 Comparing error in coupled reflected power data of proposed coupler to a conventional coupler

	Directivity [dB]	Coupling factor [dB]	Error (%) for various VSWR		
			1:1.2	1:3	1:5
Conventional coupler	30	21	60.2	21	12.4
Proposed coupler	62	27	2.1	1.6	1.1

As the output of the coupler is unbalanced, using unequal capacitor values in the input matching network provides a balanced differential drive at both the input ports of AD8307. The OFFSET feature allowed us to change the intercept point and further extend the dynamic range of the power detector. The lower range is largely limited by the thermal noise floor. Taking these considerations into account, the external matching circuitry was designed to provide the necessary dynamic range of 90 dB at 300 MHz. The lumped element values C1—4 pF, C2—3.7 pF, and LM—120 nH were calculated using ADS simulation using the touchstone (.s2p) file of the device from the manufacturer. The power detector has a slope of 25 mV per dB. The analog output was fed to a 12-bit Analog-to-Digital (ADC) converter which was integrated in the microcontroller.

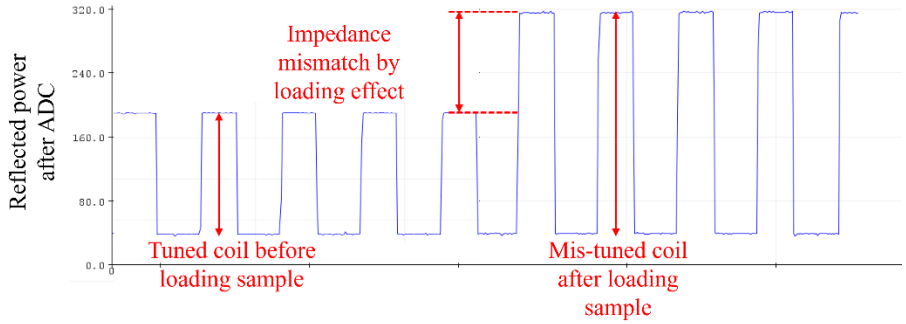

a)

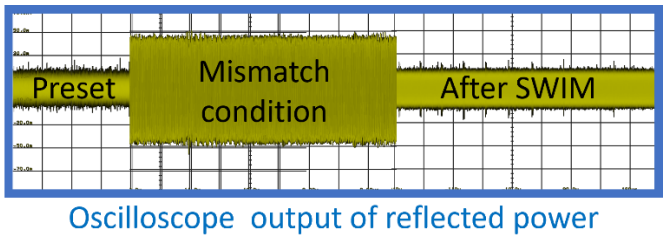

Oscilloscope output of reflected power

b)

Figure 3-14. a) change in reflected power reading (ADC value) observed in microcontroller due to loading effect. b) oscilloscope reading of the power detector before loading the coil, after loading with sample, and after the SWIM calibration is performed.

3.3.5 Impedance Matching Module

Let us revisit fundamentals of RF impedance matching with a brief introduction to S-parameters and Smith chart. Scattering parameters or s-parameters are a fundamental tool to analyze electrical performance of RF and microwave systems. These are a set of complex numbers that provide a relationship between incident and reflected waves at various ports of the system [Pozar]. Based on the voltage of input and output, they help determine the reflection loss, insertion loss, and impedance matching between two networks at a particular frequency of interest. Each of the s-parameters provides amplitude and phase relation between the input and the output signal. S_{ij} is defined as the ratio of voltage at the output of port *i* to the voltage at the input of port *j*. S-parameters of an N port device are written in N x N matrix form.

$$[V^-] = [S][V^+]$$

and

$$S_{ij} = \frac{V_i^-}{V_j^+}$$

From this Sii is the amount of input signal that gets reflected back to the same port, called the reflection coefficient (Γ) and S_{ij} is the portion of input signal that transmits to the output port, called the transmission coefficient. For example, S-matrix of a two-port device (LNA) are given as follows.

$$[S_{LNA}] = \begin{bmatrix} S_{11} & S_{12} \\ S_{21} & S_{22} \end{bmatrix}$$

Assuming port 1 as input and port 2 as output, S_{11} and S_{22} informs about the input and output impedance matching of the LNA. S_{12} gives the measure of gain of the preamplifier and S_{21} details the measure of reverse isolation that can achieved by the preamplifier. All RF/microwave circuits, both passive and active, are validated based on this S-parameter data to begin with. This helps in understanding the impedance matching, signal loss/gain, and optimize individual circuit in a system to get the signal performance necessary. Modern day vector network analyzers (VNA) measure and display the s-parameters in various formats. The most common way of measurement is logarithmic (dB) for magnitude plots and degrees for phase plots.

Equation Return Loss and Insertion loss

$$RL = -20log(|S_{ii}|)$$

$$IL = -20log(|S_{ij}|)$$

Understanding the working of transmission line theory is one of the most crucial parts of learning RF/microwave circuits. This gives the ability to design impedance-controlled lines at precise frequencies to manipulate signal along these lines in a desired manner. Transmission line theory provides us with the ability to model any length of trace as an RLC network. This theory helps in designing controlled impedance transformation lines/traces between two devices such that signal loss is minimized. As mentioned previously, when a voltage is applied at the input of a transmission line a portion of it reflects. This reflected wave interacts with the incident wave to form voltage standing wave pattern (VSWR).

Equation

$$VSWR = \frac{1 + |\Gamma|}{1 - |\Gamma|}$$

Where Γ is the reflection coefficient.

Smith chart another important tool developed in 1939 by P. Smith at the Bell Telephone Laboratories [ref]. This chart allows the users to plot complex impedance (normalized with system impedance) to understand the interaction between output of a device and input of a transmission line, for example. Impedance Smith chart as shown in Fig 3-x a) describes the basics needed to move forward with impedance matching of an RF coil. In Fig 3-x b) the dot marks an arbitrary load impedance, and the lines indicate the direction of movement of the impedance based on the configuration of the lumped element used in the matching network. In Fig 3-x c) the grey region highlights the area of the Smith chart that cannot be used when working with a 2 capacitor L-matching network.

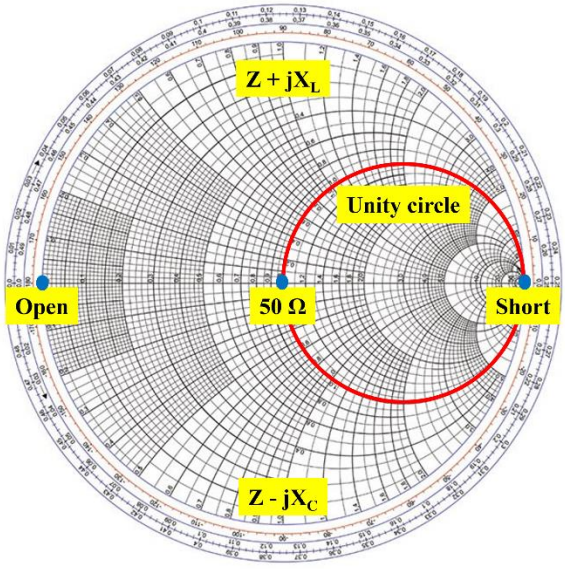

a)

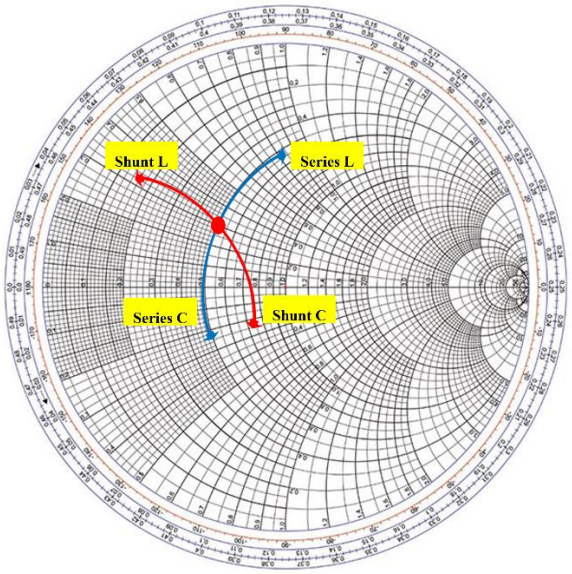

b)

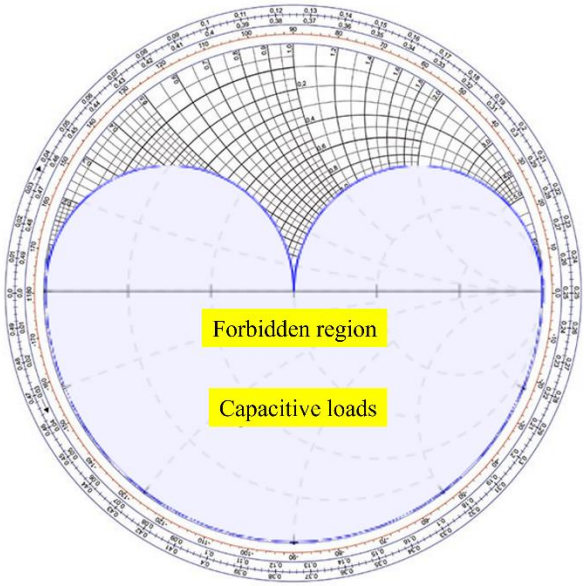

c)

Figure 3-15. Smith charts plot a) detailing the basics of Smith chart and how impedance is mapped on it, b) depicting the movement of impedance point based on the lumped

component and configuration in matching network and c) Picture of Smith chart showing the forbidden impedance region for the 2-capacitor L-matching network to work in MRI.

Based on the S-parameter theory and Smith chart impedance matching concepts we now dive deep into impedance matching an RF coil so that we can achieve maximum signal detection during the spin relaxation phase and acquire a detailed image. Space inside a preclinical scanner is extremely limited and it is difficult to place the SWIM system inside the bore close to the RF coil without using a long coaxial cable. Therefore, a surface coil

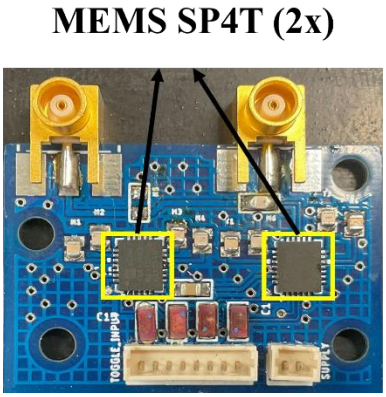

a)

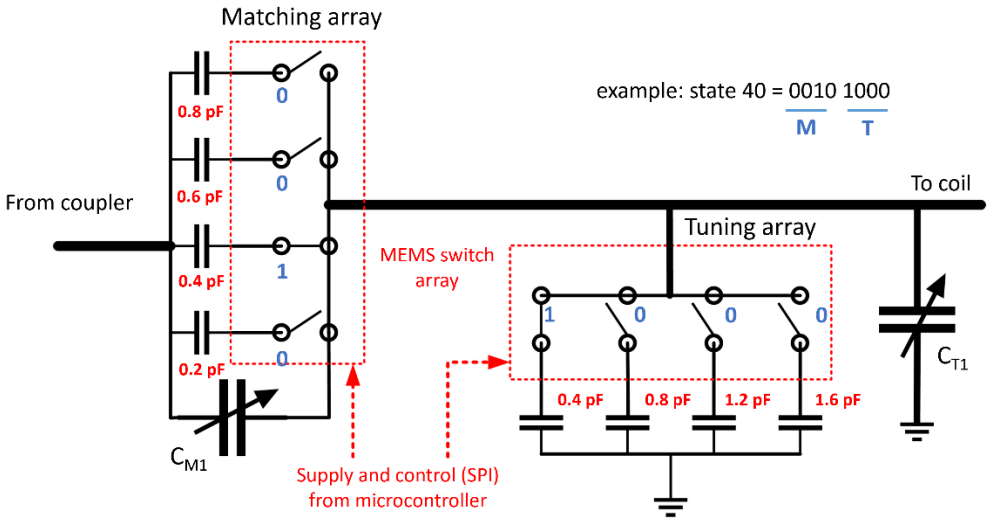

b)

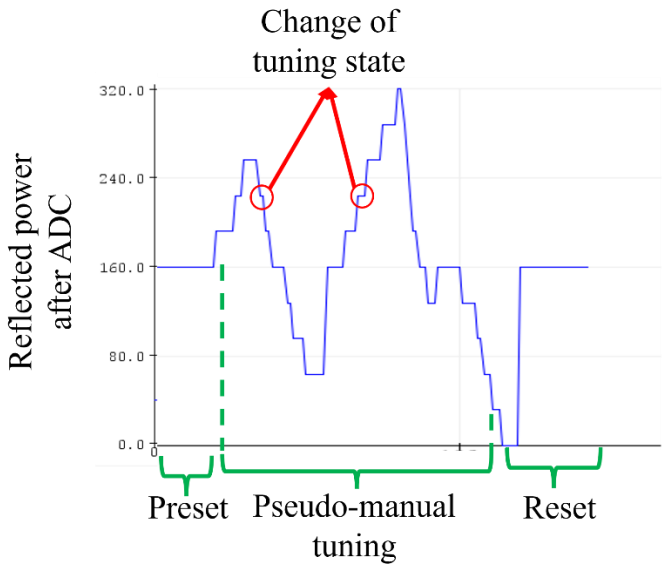

c)

Figure 3-16. a) Surface coil with MEMS capacitor array L-matching network that can be electronically tuned and matched, b) L-matching MEMS capacitor array schematic with 4 series capacitors and 4 shunt capacitors, and c) ADC reading of reflected power by the microcontroller as the tuning states are changed pseudo-manually.

We then connected the SWIM system outside the bore which includes the wireless control system (microcontroller) to electrically change the impedance of the coil by changing the state of the capacitors as shown in Fig 3-x b). This switch was chosen because of high linearity and low COFF and RON for each port. The insertion loss and isolation of any one of the 4 ports (RFx) to the common port (RFC) at 300 MHz were measured to be 0.16 dB and 47 dB respectively. The switch also measured a crosstalk isolation of 45 dB between two ports. In shunt configuration, RFC was connected to the trimmer capacitor and each of the 4 switches were connected with a fixed capacitor

(0505C Non-magnetic capacitors, Passive Plus Inc, USA) to ground. Similarly, in series arrangement, 4 fixed capacitors were connected to form a capacitor array. We also used a 10 MΩ resistor in shunt with each fixed capacitor to avoid floating capacitance during the off state of the switch. Each of the 4 throws can be individually controlled using Serial Peripheral Interface (SPI) in a multiplexer (MUX) style to create 256 combinations. The ON time of the MEMS switch was 75 μs, thus making the quickest time to cycle through all combinations without delays was approximately 20 ms. But a 5 ms delay between state transitions was introduced to account for RF settling time which makes a 3 s total run time for automatic tuning and matching sequence. The eight fixed capacitor values were picked by loading various sample sizes into the coil to understand the scope of impedance mismatch based on sample size. This method ensured that the SWIM system was not limited by capacitor values for a large variety of sample sizes.

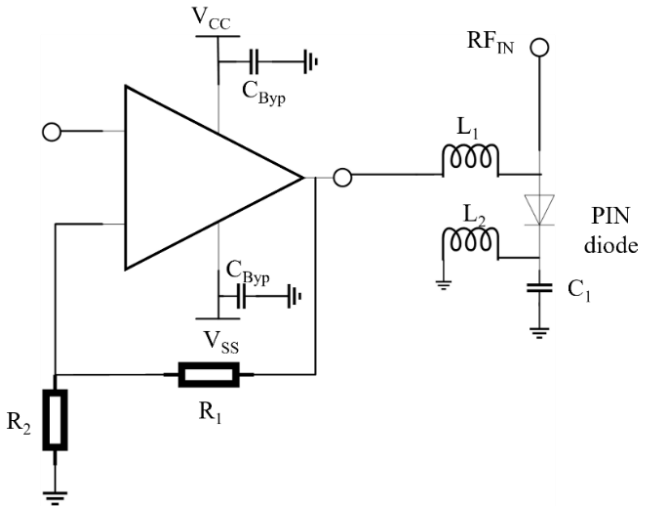

a)

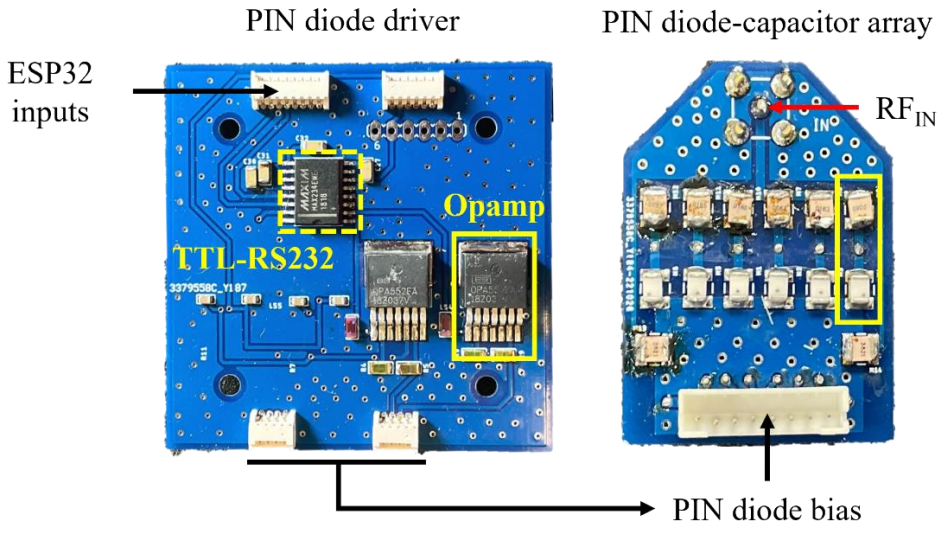

b)

Figure 3-17. a) schematic diagram showing the Opamp driver and one PIN diode and b) Picture of assembled PCB of Opamp driver and PIN diode array (shunt arrangement)

High power tuning array is designed like the MEMS capacitor array where each diode acts as an SPST switch turning on/off the capacitor associated with it. Each diode is biased with an opamp driver to provide sufficient forward current and reverse voltage to toggle the pin diode as a switch. Each GPIO pin from the microcontroller is connected to the opamp driver board where LVTTL signal converted to RS232 in the stage. This gives +/- 10V. But the RS232 converter has an inverted output, therefore a logic “0” becomes logic “1” and vice-versa. This converted signal is then given as input to OPA552 high voltage high current opamp module with +/- 25V Vcc and Vss. Each opamp can provide up to 200mA current but the supply is set to +/-25V and 100mA current for smooth operation of the PIN diode capacitor array.

3.3.6 Wireless Control Module

The wireless microcontroller (ESP32-WROOM-32D, Espressif Systems, China) used in the SWIM system is a powerful, cost-effective, and easy to use module with generic Wi-Fi, Bluetooth, and Bluetooth Low Energy (BLE) capabilities as shown in Fig 3-18. We used the built-in 12-bit ADC of the ESP32 to read the reflected power from the power detector and map it to each of the 256 states of the matching network array. SPI protocol is used to control the MEMS switch instead of digital pins as serial communication is robust and makes it easier to customize the system by adding more MEMS switches in the future. An array of digital pins is connected to power detector and power supply regulators to enable and disable these devices according to need. This reduces additional power supply noise and reduces power consumption of the SWIM system during imaging sequence as these devices are turned off.

Figure 3-18. PCB picture of the microcontroller board with ESP32 and DACs built in along with necessary power regulators

Nonetheless, during bench tests, both topologies showed adequate tuning and matching range to compensate for various phantoms representing small animals like mouse and rat for the chosen coil diameter. For coils with larger diameter, removing

matching capacitor CM at the coil end increased the frequency range of tuning. We concluded that the user could choose between the two options based on coil diameter and number of distributive capacitors. We used a brute force technique to find the minimum reflected power for a given sample. We integrated a bubble sort algorithm within the impedance state sweep to generate a time-efficient routine compared to a look-up-table method. ADC values were averaged to avoid erroneous power detector readings. Since the intention was to develop a general-purpose system meant to tune and match almost any small animal receive coil at 300 MHz, brute force routines work quickly if there are a small number of impedance states. Advanced optimization techniques like a gradient descent algorithm can be implemented to use the input “preset” state as a basis to find the lowest reflected power for a particular receive coil setup or an array of receive coils, by reducing time taken to match individual coils using the “preset” condition.

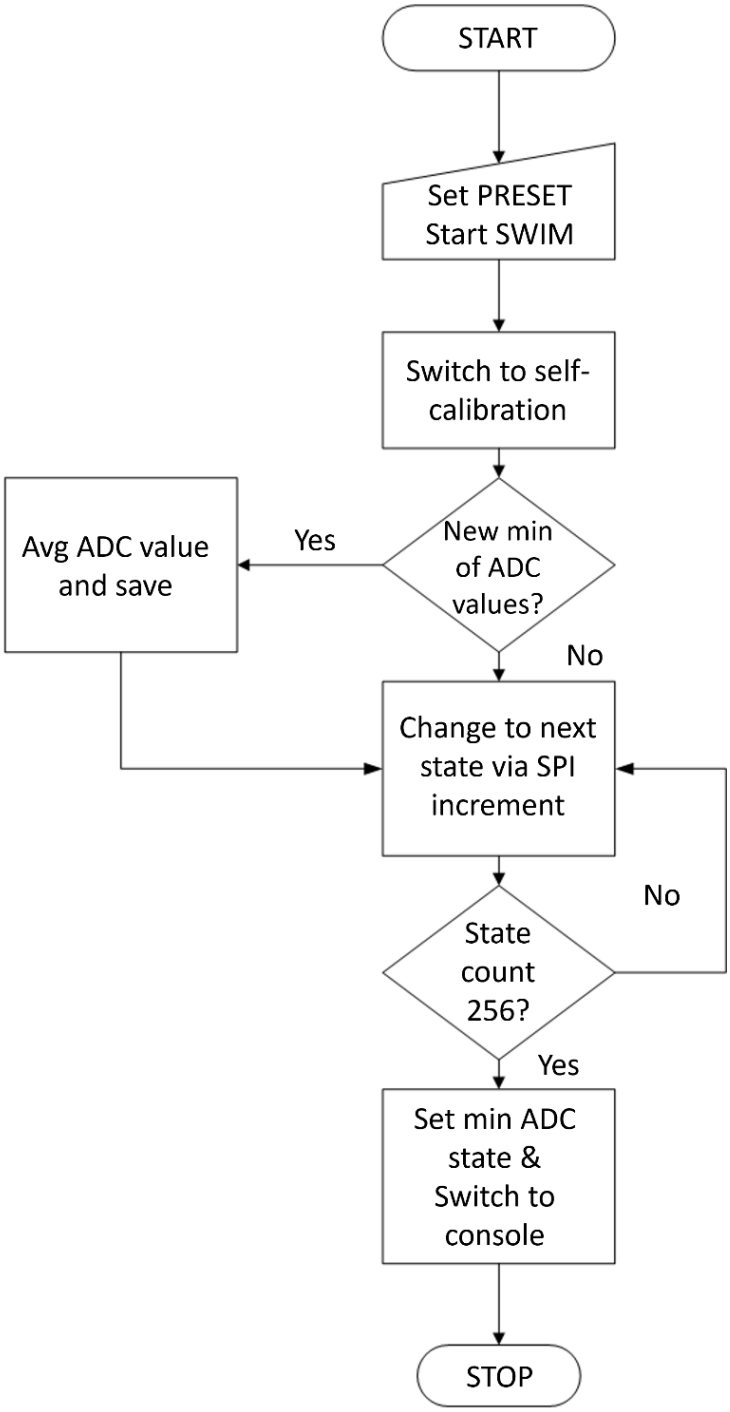
START
Set PRESET
Start SWIM
Switch to self-calibration
New min of ADC values?
Yes
Avg ADC value and save
No
Change to next state via SPI increment
State count 256?
No
Yes
Set min ADC state & Switch to console
STOP

a)

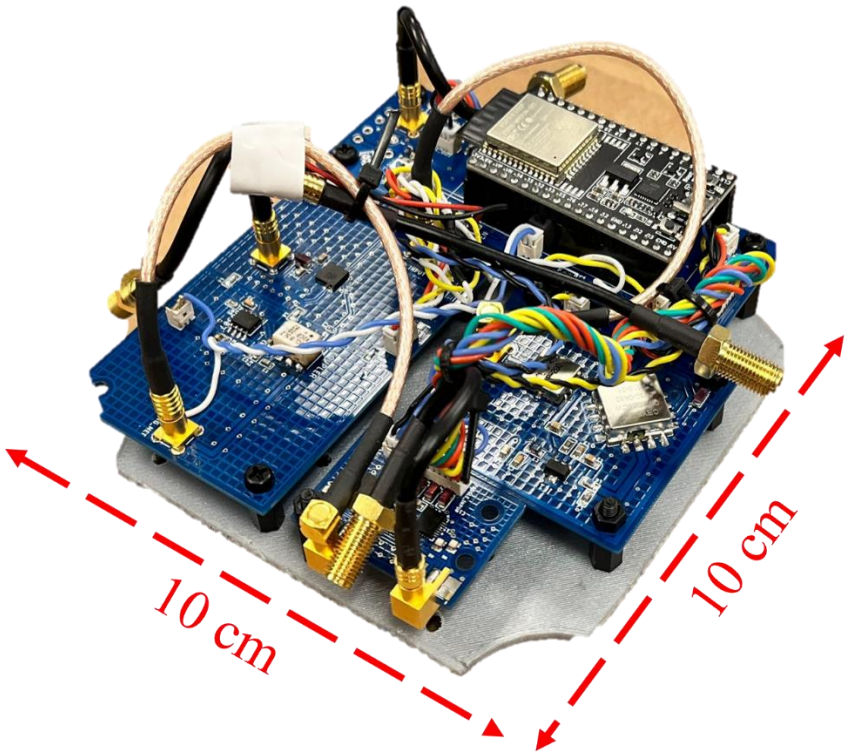

b)

Figure 3-19. a) Algorithm flow of the SWIM system b) Birdseye view of the low-power SWIM system

3.3.7 Android Application

Once the SWIM system is connected to the coil and placed inside the scanner room, the user control completely falls on an Android mobile application that was developed using Kodular, an app design platform. Kodular is a block-based coding platform to design and develop Android based applications for various purposes. This simple, cost-effective, and open-source platform is a beneficial tool to design mobile applications for the SWIM system. The block-based coding method for android applications makes it user friendly for all levels of engineers to change and update the

functionality of the SWIM app based on their particular needs. It avoids complex and mainstream coding platforms like Android studio (Kotlin/Java script) and offers cloud-based memory storage services to gather large amounts of tuning and matching data for various individuals to access for research purposes. Simple yet offer all major features like Bluetooth protocols, Serial communication protocols, ability to launch on Google Playstore etc. All of those features we utilize to some extent in controlling the SWIM system. An Android tablet was used to install the developed application and it is paired with the Bluetooth feature to create an interactive interface with the microcontroller.

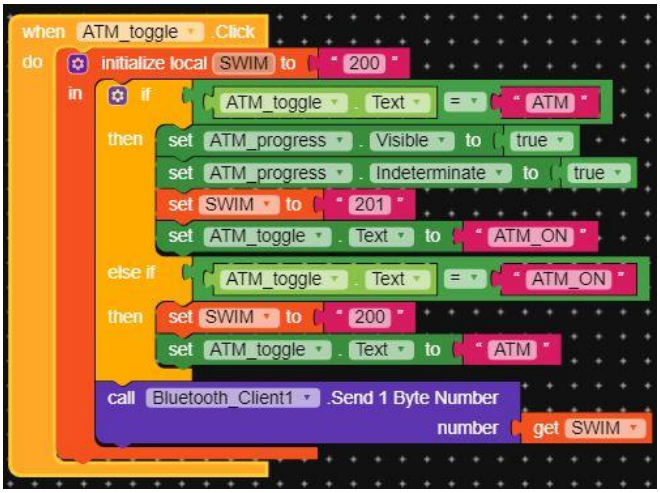

Figure 3-20. Example picture of block-based coding design to develop an Android mobile application using Kodular

We have developed an Android mobile application using Kodular as shown in Fig 3-20. Each ESP32 inside the SWIM system generates a unique MAC address along with a user defined name that can be selected using the Bluetooth connectivity panel. Up to eight individual SWIM systems can be connected to the Android application and controlled independently, thus allowing the user to scale this design to accommodate up

to eight channel RF coils. After pairing the SWIM system to the mobile device, the SWIM control panel activates, and the calibration panel is reset to “red” color indicating no tuning and matching performed as a status message.

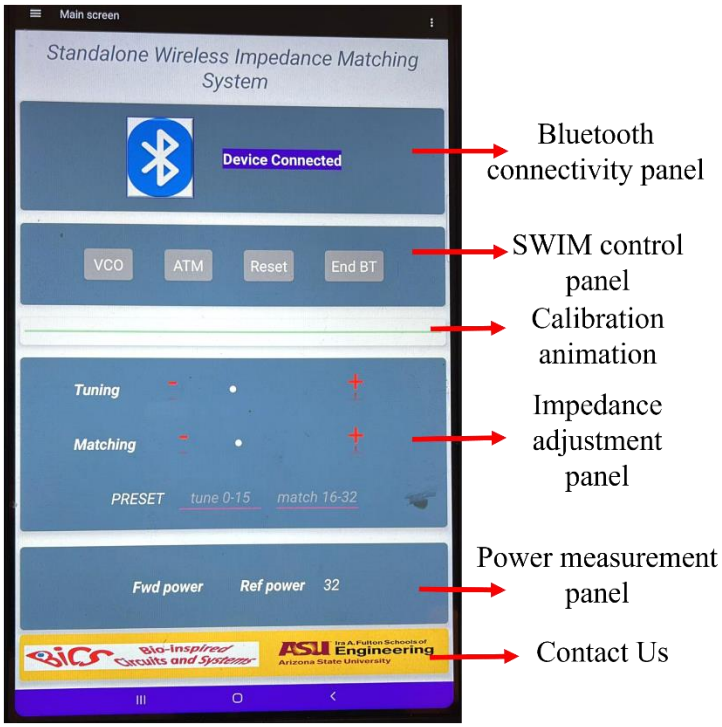

Figure 3-21. Main screen layout picture of the SWIM application

Four buttons were designed to independently control the self-calibration module and all its features. The “VCO” button toggles the standalone module between ON and OFF thus allowing the user to start the CW RF signal for tuning calibration. The “ATM” button allows the user to start the automatic impedance calibration function (after the VCO button is ON). During the tuning calibration process the SWIM system toggles various capacitor values called “states” and selects an optimal impedance condition based on sample and coil design. Once the automatic process is completed, the calibration animation panel turns “green” indicating the completion status message. This informs the

user to continue with the next steps. The “Reset” button can undo all the automatic and user induced changes to the SWIM system setting it back to the original condition for a fresh start if required. During this reset state the application asks the user for a “preset” state (if known to the user) so that the automatic impedance matching can begin at an ideal position based on the coil. This feature is useful for users who built their own coils and have an idea of the input impedance for their design.

Below this is the Impedance adjustment panel with two input dialog boxes are placed to set the remote tuning and matching separately based on the coil parameters, known as the “preset” condition. Sixteen states each for tuning and matching, respectively are assigned in this design. Since these can be switched independently of each other we achieve a combination of 256 states (256 capacitor combinations). Two slider bars were designed to provide wireless pseudo-manual control of tuning and matching capacitor array independently and irrespective of the auto-calibration function. After the automatic function, these slider bars can also be used to fine-tune the impedance condition. They also provide an easy wireless adjustment of impedance condition between scans to account for sample movement.

If the user inputs the amount of input power in dBm in the “power measurement panel” at the end of the autocalibration the reflected power is displayed in dBm based on the reflections observed by the power detector module. After being satisfied with the impedance of the coil, Bluetooth can be disconnected using the “End BT” button. During this phase the microcontroller will be placed in deep sleep to avoid inducing any external electronic noise to the image that comes from fast clock (on board oscillator). And

finally, the contact information of the lab and a communication form are available when clicked on the “ASU” logo thus allowing us to send error messages or difficulties in understanding the design/functions.

3.4 System level performance validation

A two-port VNA (FieldFox N9923A, Keysight Technologies, USA) was used to measure the S-parameters of the proposed SWIM system to validate the bench test performance with various loading conditions. Different sizes of cherry tomatoes were used to gather data on loading effect along with a saline sample prepared for 7T field strength. Bench test in a system level design is crucial as it integrates an independent tuning and matching system with a coil of specific input impedance. Studying the loading effect with various samples gives an understanding of the extent of mismatch condition on impedance and range of frequency tuning necessary to successfully perform the automatic tuning and matching for that specific coil.

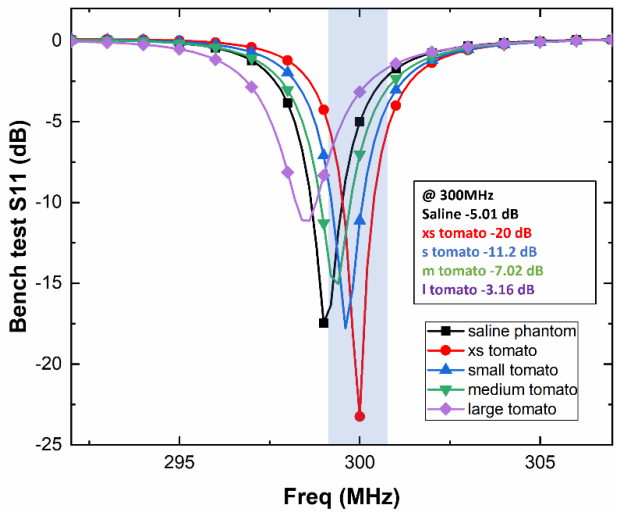

a)

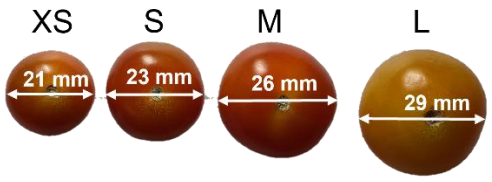

b)

Figure 3-22. a) return loss plot of the surface coil when loaded with various samples (no tuning is performed) and b) picture of different sizes of tomatoes used to understand the loading effect on surface coil

General-purpose systems have extremely high system level integration standards to meet user needs across the globe. Therefore, we incorporated two techniques i) an automatic impedance calibration step and ii) a pseudo-manual calibration step where the user can electrically cycle through all possible impedance conditions and pick one that is ideal for that coil. As shown in Fig 3-23 a), the experimental setup used to bench test the system with a surface coil and saline phantom of miniature human head. We introduced

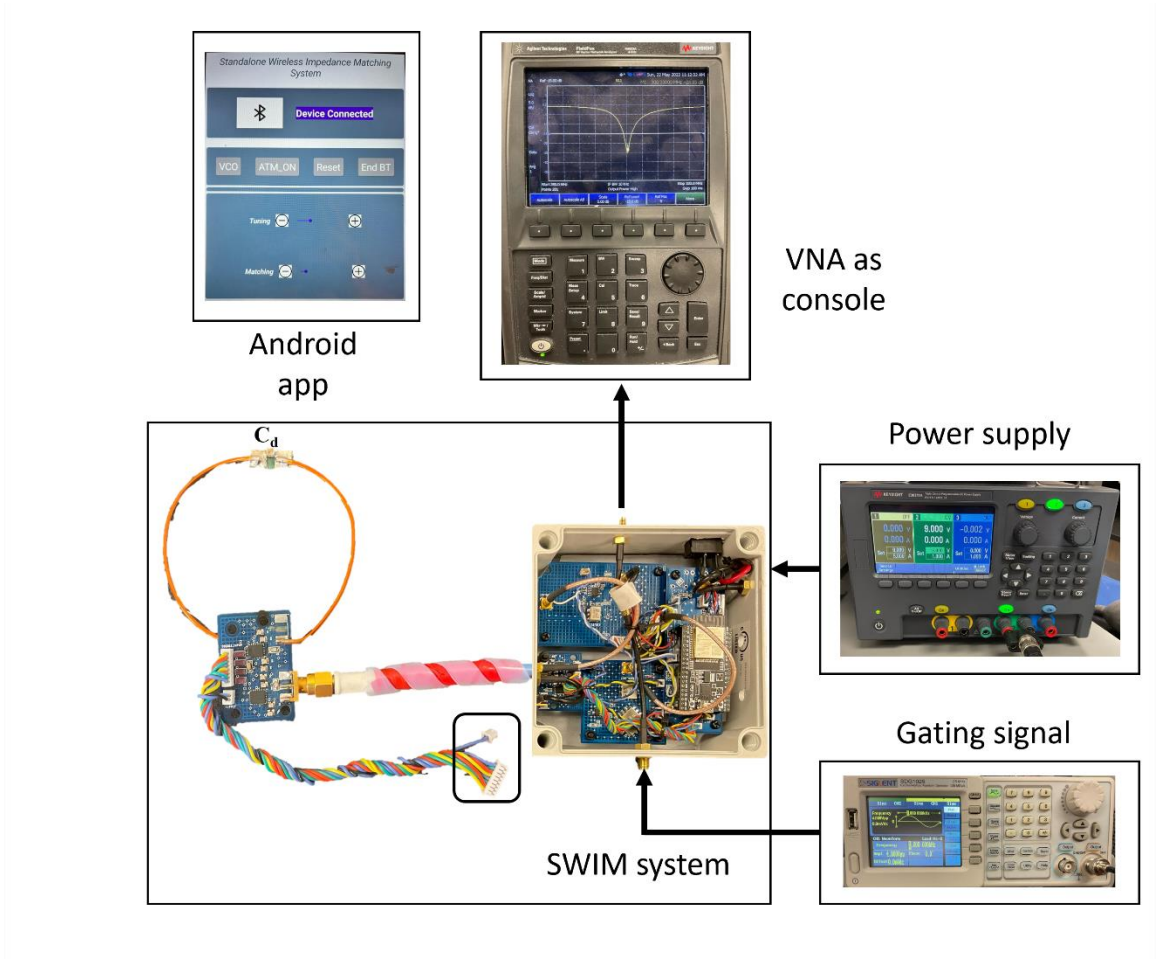
Standalone Wireless Impedance Matching System
Device Connected
VCO
ATM_ON
Reset
End BT
Tuning
Matching
Android app
VNA as console
C_d
Power supply
Gating signal
SWIM system

a)

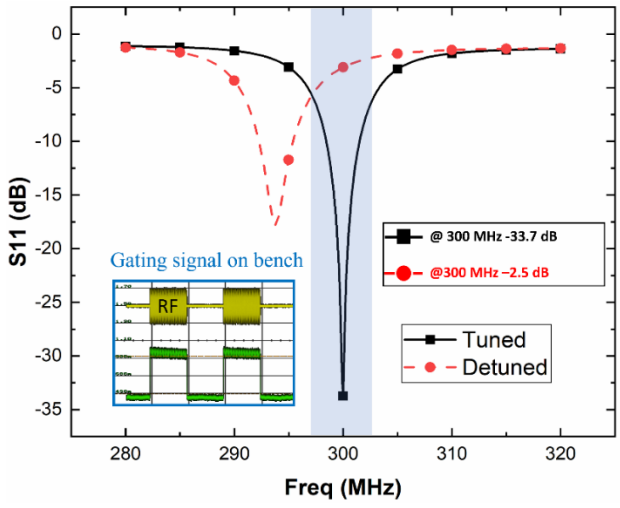
S11 (dB)
Freq (MHz)
0
-5
-10
-15
-20
-25
-30
-35
280
290
300
310
320
Gating signal on bench
RF
@ 300 MHz -33.7 dB
@300 MHz –2.5 dB
Tuned
Detuned

b)

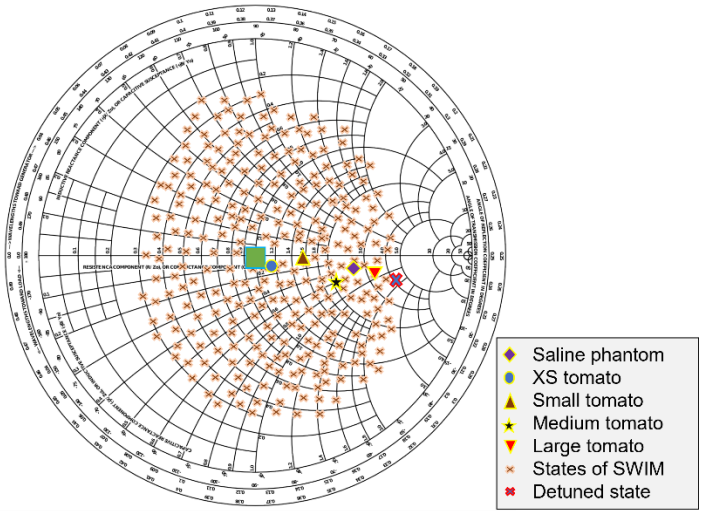

c)

Figure 3-23. a) Picture of the bench test experiment setup along with different equipment like DC supply, gating signal generator, VNA to display tuning condition, and Android application to control the system. b) Return loss plot of the coil with and without "detuning" condition along with a replica of MR gating signal (inset). c) Smith chart plot of impedance points for various loads along with coverage of the SWIM system for 256 impedance states

a new concept of actively detuning the RF coil during transmit pulse using the SWIM system instead of PIN diodes.

All the MR imaging studies were conducted at Barrow Neurological Institute - Arizona State University (BNI-ASU), Center for Preclinical Imaging, using a 7T small-animal, 30-cm horizontal-bore magnet and BioSpec Avance III spectrometer (Bruker, Billerica, MA) with a 116-mm high-power gradient set (600 mT/m). Fast-Low-Angle-Shot (FLASH) Sequence with a repetition time (TR) of 350 ms, echo time (TE) of 5.4 ms, and a flip angle (α) of 20 degrees was used for MR imaging experiments. A field of

view (FOV) of 40 x 40 mm and 256 x 256 matrix leading to an in-plane resolution of 156 x 156 μm, in addition 9 slices were acquired along the sample with a slice thickness of 1 mm. A Bruker Linear Birdcage coil was used as the transmit coil. The peak power used for the FLASH sequence was 700 W. A rat bed of 72 mm diameter was used to hold the receive coil housing. Sample was then placed inside the receive coil housing and fed into the scanner.

After loading the saline sample, retuning of the coil was not performed, and an image was acquired to show the effect of impedance mismatch. Two studies were performed to analyze the noise of the proposed system, with microcontroller in deep sleep mode and with microcontroller set to active mode. SNR of the ROI for the mismatched impedance condition was measured as 26.85 dB shown in Fig. 3-24 a). However, when the microcontroller was in active mode with continuous wireless communication, the noise levels were significantly higher causing a drop in SNR from 26.85 dB to 24.08 dB (10.8% decrease) even after automatic impedance matching as shown in Fig. 3-24 b). We then proceeded to place the controller in deep sleep mode where all the SWIM system processes are electrically switched off and the optimal impedance condition was set to the MEMS switches. This has shown substantial improvement in SNR from 26.85 dB to 34.15 dB as shown in Fig. 3-24 c). To fully characterize the effectiveness of the SWIM system we also performed manual tuning and matching using trimmer capacitors without SWIM system and computed the SNR to be 34.96 dB as shown in Fig.3-24 d). Four different cherry tomatoes were imaged to validate the general-purpose performance of the SWIM system. Before and after SWIM

calibration images of extra small tomato (d=21 mm), small tomato (d=23 mm), medium tomato (d=26 mm), and large tomato (d=29 mm) are shown in Fig. x respectively. As tomatoes contain many inhomogeneities such as air bubbles, water, and seeds, accurately calculating the SNR is a challenge. Therefore, we present the mean signal levels from the ROI for each tomato (before and after SWIM) to show the impact of the SWIM system. As a surface coil was used for imaging, an ROI was identified close to the coil as marked with dashed circle for all the above calculations. The mean signal intensity has improved by 23.04% for extra small tomato, 43.27% for small tomato, 45.26% for medium tomato, and 46.56% for large tomato respectively. The larger the mismatch caused by the sample, the larger is the improvement in mean signal intensity as it is retuned to center frequency after the SWIM calibration sequence.

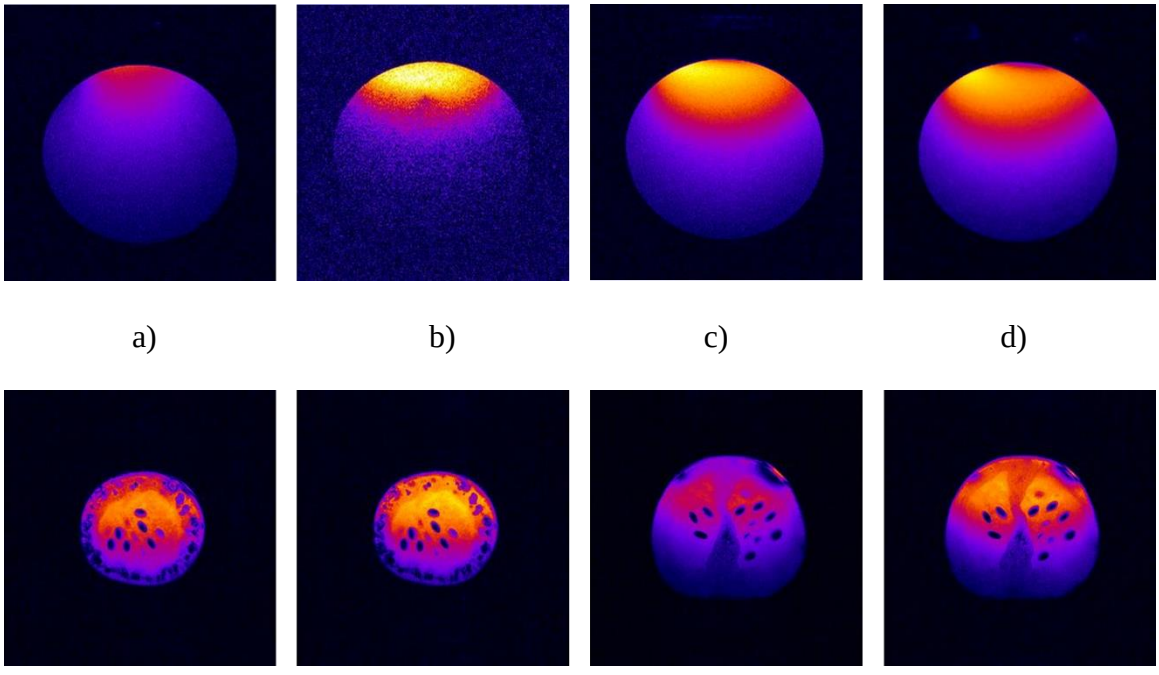

a) b) c) d)

e) f) g) h)

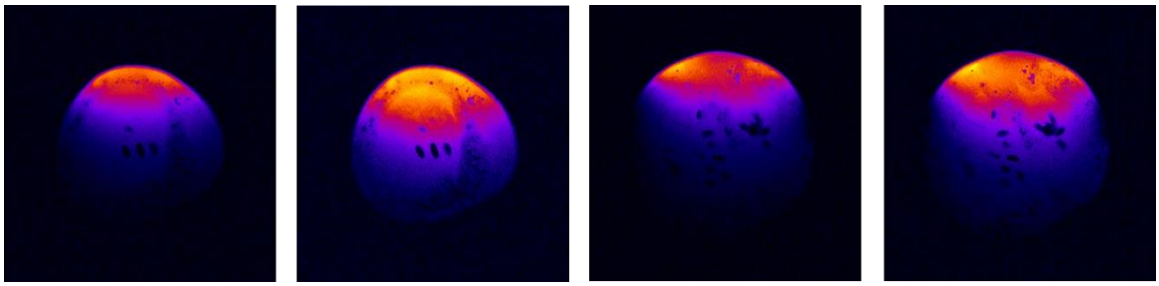

i) j) k) l)

Figure 3-24. MR images of different tomatoes before and after SWIM impedance calibration

The MR images show that retuning and matching the coil after loading the sample will considerably increase the SNR of the coil. We calculated peripheral and overall SNR of the saline sample images (as saline sample is homogeneous) to fully characterize the improvement caused by the SWIM system. The SNR of the full image area increases by 17.2% (22.6 dB to 26.85 dB) after retuning the coil with the SWIM system. We also observed an increase in SNR at the bottom of the sample (opposite side of the coil) by 19.35% from 14 dB to 17 dB after the automatic calibration. The top side has seen an increase of 24% (26.85 dB to 34.15 dB) as the coil is closely placed on the sample. We also computed the SNR from left and right side of the image which showed 14.2% (18.06 dB to 20.82 dB) improvement after using the SWIM system. An image of the same sample with similar conditions was acquired with manual impedance matching using trimmer capacitors, where the SNR was calculated to be 34.96 dB. This shows a 2.34% decrease in SNR when compared to the image acquired using the SWIM system. A 1.2 dB insertion loss from SWIM components was measured during the bench tests, which include RF SPDT switch, bidirectional coupler, and the matching network with MEMS

capacitor array. Along with the insertion loss of the system, microcontroller in active state induces noise further degrading the SNR even after an optimal impedance condition has been achieved by the SWIM system.

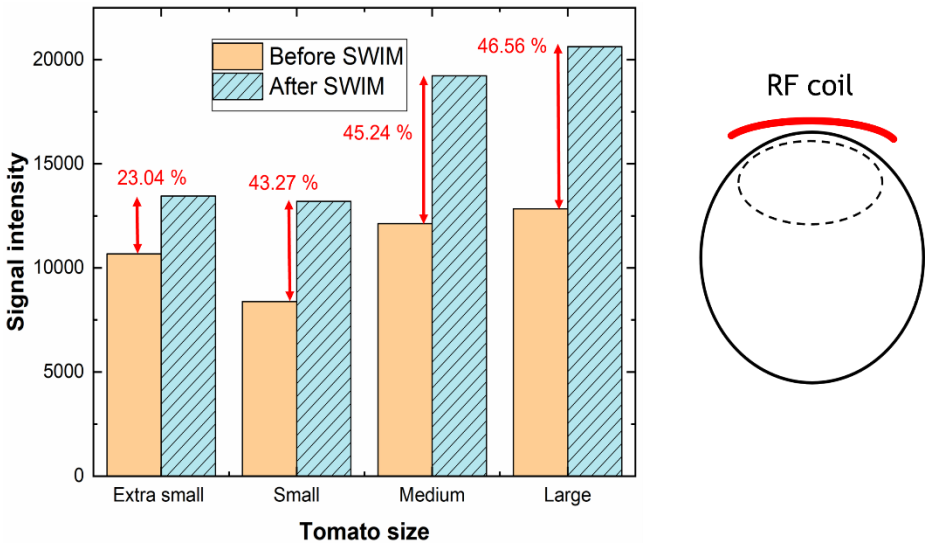

Figure 3-25. Mean signal intensity plot of various sizes of tomatoes before and after SWIM system calibration. (inset) ROI where the SNR is calculated with red line showing orientation of coil.

Therefore, we used the ESP32's deep sleep protocol after calibration to electrically power off the processing unit, RAM and all the digital peripherals except for RTC timer to wake the system for subsequent adjustments or power monitoring. RF MEMS switches retain the last received state via SPI and help maintain the optimal impedance condition during the deep sleep mode. Deep sleep acts as a power saving function as the controller consumes only 10 µA current in deep sleep compared to ~120 mA during the active state with continuous wireless communication. Various conditions were explored to offer a good starting position for the system but, we concluded that an option to decide the PRESET condition must be given to the user to customize the SWIM

system for their needs. The system takes around 3 seconds to complete the process of tuning and matching with a brute force algorithm. The SWIM system provides the user with a greater level of monitoring and control than existing systems. Preclinical systems present a challenge for manual tuning with long tuning sticks and narrow bore sizes. Wireless communication combined with speed and efficiency enables effortless operation of the complete standalone system to avoid long cables and tuning sticks in preclinical scanners.

CHAPTER 4

INFLATABLE RF COIL DESIGN FOR ENDORECTAL PROSTATE IMAGING

4.1 Current trends in stretchable and flexible RF coils in MRI

Surface RF coils are for local use and have low B_1 field penetration [122-125]. Surface coils have evolved from rigid to flexible and progressed towards stretchable coils. Liquid metal flexible coils for MRI were investigated as early as 1986 with Mercury conductive traces in silicon tubes [126]. A transceiver coil with shielded-coaxial-cables (SCC) that is flexible and can conform to the sample shape was introduced for human knee imaging at 7T [127]. A flexible coil using screen-printed silver ink on a 75 µm thick polyethylene terephthalate (PET) substrate was studied at 1.5T and 3T [128]. Receive only coils for 9.4T MRI applications were developed with silver conductors on flexible polyimide (Kapton). Traces were printed on both layers of Kapton to imitate lumped capacitors on the coil [129]. Liquid metals like Eutectic Gallium-Indium (eGaIn) are modern solutions to create stretchable and flexible devices, such as RF coils for MRI and general-purpose antennas [130-134]. Ink-jet printing was used to lay eGaIn over a neoprene substrate, creating a flexible and stretchable receive coil [130,131]. Screen printing or ink-jet printing are design-friendly techniques but may not be cost effective. Self-tuning elastic receive coil was developed using silicon polymer and liquid metal at 128 MHz for knee imaging [135]. Flexible and conformal RF coils present sub-optimal impedance matching condition at receiver due to change in loading conditions in MRI. A few automatic impedance matching systems were investigated to compensate the mismatch caused by loading effect in MRI [136-142]. Coil resistivity along with

dielectric and inductive losses in the sample and preamplifier losses are the three main reasons for noise in receivers [142-144]. Previous investigations have shown that intrinsic Signal-to-Noise ratio (SNR) of the copper antennas is superior to that of liquid metal antennas. eGaIn is 17-times more resistive than copper. Considering the skin effect at higher frequencies it can be observed that the effect of increased resistivity is only up to 4-times. Flexible and elastic designs to enhance patient comfort compensate for the low intrinsic SNR of liquid metal RF coils.

4.2 Novel elastic and stretchable RF coil

As recent studies in MRI community have headed towards improving and creating new ways to design and develop elastic RF coils, we propose a novel design of inflatable and stretchable RF coil that can be integrated with the SWIM system for endorectal prostate imaging. A wirelessly controlled pneumatic system is used to inflate and deflate the coil.

4.2.1 Elastic and flexible RF coils

Initially working towards the goal of conformal RF coils for MRI, we approached the problem by developing elastic and stretchable RF coil using silicone polymer to understand the combined impact of loading effect and changing size on coil impedance and tuning in preclinical scanners. Fig 4-1 a) clearly describes the process of fabricating layers for the elastic RF coil. Two parts of a silicon polymer A and B (Ecoflex, SmoothOn) are mixed in equal ratio (1:1) at room temperature in a small dish and mixed thoroughly to create a bond between the two materials.

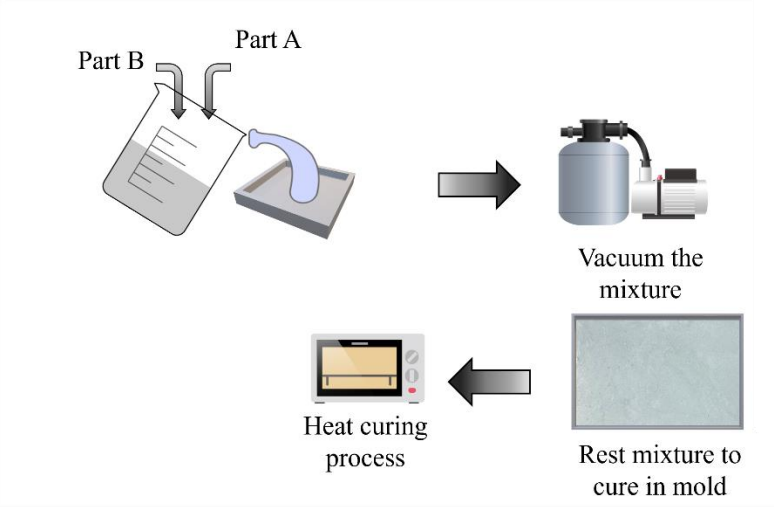

a)

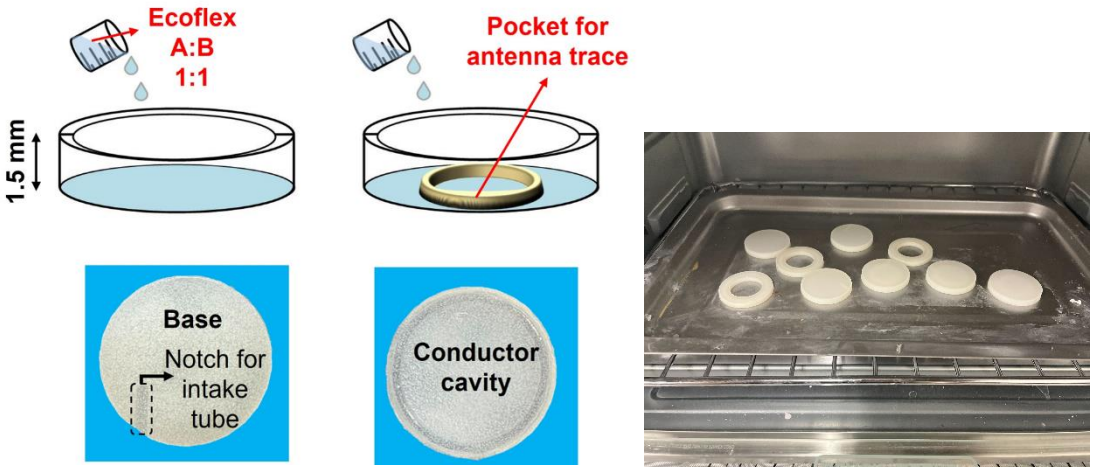

b) c)

Figure 4-1. a) General block diagram of the fabrication process of silicon polymer liquid metal RF coil, b) Two different layers created using above mentioned process to make flexible and stretchable RF coil and c) Using toaster oven to cure the silicon layers to remove impurities and improve curing time.

Once the materials are cured at room temperature for 40-45 minutes, it is placed in an oven (preheated to 280 F) for 3-4minutes. The LM coil was fabricated by injecting

eGaIn into a microfluidic channel of 1.5 mm diameter. The ends were sealed by 3D printed inserts and copper wires of 14 AWG. Then, two heat shrinks are placed on both ends to avoid any leaks. An L-matching network with trimmer capacitors compensates for the loading effect caused by different phantom sizes and stretching of the LM coil. It is designed to stretch about 40% of its original dimensions without causing any physical damage to the microfluidic channels. The material itself can stretch over 80% of its initial dimensions and retain its shape after excessive usage and stretching but the metal inserts and microfluidic channel can interact during stretching and cause small ruptures that can compromise the integrity of the coil. Therefore, we classified “medium stretch” as 20% of its original diameter and “heavy stretch” as 40% of its original diameter. The tomatoes were picked such that, the liquid metal coil when wrapped around has no stretch, medium stretch, and heavy stretch of its diameter. Bench test data from Fig 4-2 displays the change in resonance frequency as the coil is stretched over three different levels. The coil is perfectly tuned in resting condition or “no stretch” position and has a return loss of 30dB. In “medium stretch” condition the coil has a return loss of 10dB and in the “heavy stretch” condition is it less than 5dB. This shows the impact of stretching on tuning and matching of the RF coil.

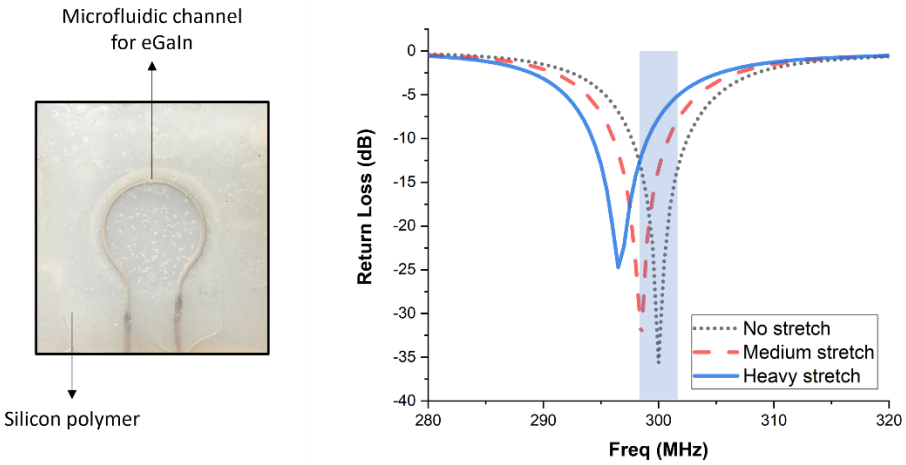

Figure 4-2. Picture of a liquid metal RF coil design at 7T using microfluidic channel in silicon polymer (left) and impact on coil resonance frequency as it subjected to stretching (right).

16 mm diameter coil fits without any stretch on the smallest tomato while increasing the diameter to 18.4 mm and 22.6 mm for medium and large sized tomatoes respectively when wrapped around for imaging. Image quality depends on the position of the coil as well as the tuning of the coil frequency. In Fig 4-3 we compare the effect of distance between coil and sample in case of rigid coil in (a) and impact of stretching the coil radius using a liquid metal coil in (b). A Fast-Low-Angle-Shot (FLASH) Sequence with a repetition time (TR) of 400 ms, echo time (TE) of 5.4 ms, and a flip angle (α) of 25° was used for both MR imaging experiments. A field-of-view (FOV) of 60 x 60 mm and 256 x 256 matrix leading to an in-plane resolution of 234 x 234 μm, in addition 10 slices were acquired along the sample with a slice thickness of 1 mm and a slice gap of 0.1 mm. The LM coil improved the signal intensity in the ROI when compared to the copper coil. The separation distance between the coil and the subject was observed to

have a greater impact on image quality than the radius of the coil. The average signal intensity of each sample was increased by 16% (small tomato), 24% (medium tomato), and 35% (large tomato). The SNR values for the rigid copper coil placed 5mm away from a small cherry tomato that was tuned is observed to be 21.2dB and when the distance was kept same but loading effect is changed by using a larger tomato, the SNR dropped to 17.84dB.

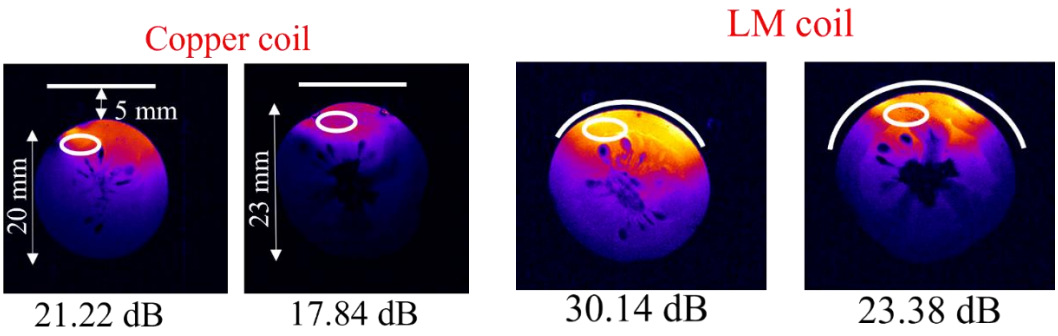

Figure 4-3. a) MR images using traditional copper coil with a gap between sample and coil and b) MR images of same cherry tomato using liquid metal RF coil of similar dimensions on an elastic silicone polymer substrate

Assuming a similar external noise environment, this means there is a two times loss in signal intensity from the same ROI. In the case of LM coil, by simply placing the coil conforming to the sample we can observe a drastic increase in the image quality and SNR (30.14dB) from the same ROI. Even by swapping the smaller tomato with larger one, the ability of the coil to wrap around has allowed to detect slightly more MR signal from the ROI (23.3dB) compared to a copper coil that was far away. Therefore, it is observed that LM coils offer the opportunity to use a single coil across different age

groups of rats and mice, which have varying head and body shapes, without compromising image quality.

4.2.2 Inflatable RF coil design

Prostate is a gland in the male reproductive system that produces fluid for the semen that transports sperm. It is a slightly conical shaped gland that is in front of the rectum and below the bladder. The prostate phantom is divided into 3 ROIs for SNR analysis of inflatable coil performance shown in Fig 4-4.

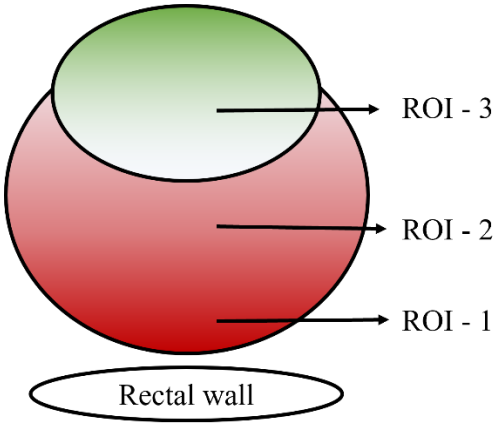

Figure 4-4. Simplified sketch of the prostate gland defining the 3 ROIs for this study

Prostate cancer is the second most common diagnosed cancer after skin cancer in the United States. One in every seven men over the age of 65 are diagnosed with this cancer. Some early state prostate cancers were identified in as young as 40-45 years men. Studies have shown that men who were diagnosed early had 87% more chances of living compared to late diagnosis. It is also a leading cause of cancer death in men over 85 years of age. The high mortality rate may also be a reason for late detection. The past six decades has seen a steady rise in the prostate cancer cases which could be stemming from environmental factors, increased fat percentage in diet, sex hormones, steroid hormones,

etc. As we observed the importance of coil positioning compared to dynamic coil shape and their distinct impact on impedance, image quality, and SNR. From Biot-Savart's Law

Equation

$$B_1(d) = \frac{\mu_0 I R^2}{2(R^2 + d^2)^{3/2}}$$

We identified an area for improvement in the endorectal prostate imaging field. Currently available traditional endorectal coils have two major issues that need to be addressed. First, the coil is a rigid PCB or copper wire design that does not move closer to the prostate rather depends on the balloon design surrounding for help to move closer to the ROI. This movement of coil closer to the sample almost negligible and most balloon designs in the current coil are meant to reduce the motion artifact cause by breathing.

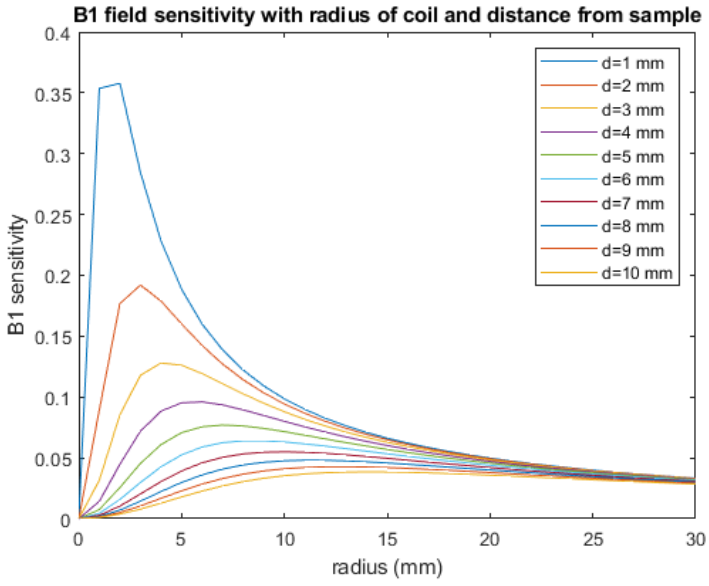

a)

b)

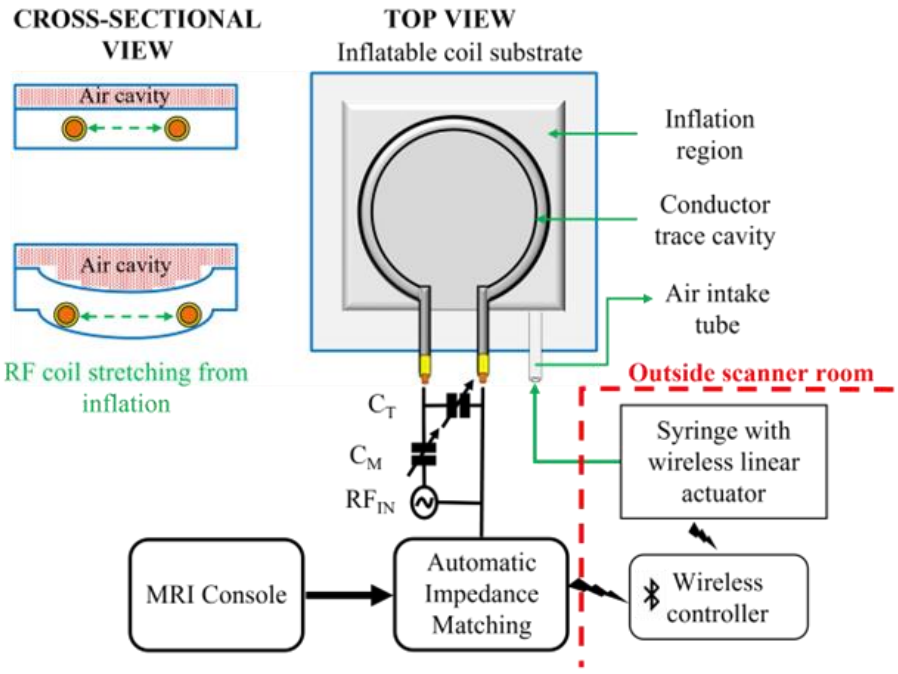

c)

Figure 4-5. a) Plot of the B_1 sensitivity with respect to coil radius and distance between coil and sample, b) Picture of current endorectal RF coils with external balloon for inflation, and c) Block diagram of the proposed inflatable RF coil with wireless impedance matching

Secondly, the impedance matching and tuning of the coil prior to inflation and after inflation cannot be adjusted. Current prostate coils rely on low Q designs that

sacrifice sensitivity and SNR to retain the frequency tuning post insertion into the rectal cavity.

In this section of the thesis, we attempt to resolve the above-mentioned issues and show feasibility for future designs that can lead to improved hardware in endorectal prostate imaging area. In this novel design, we propose to extend the stretchable LM coil from the previous section with inflatable air cavity to give it an ability to move up and down as shown in Fig 4-6 a). This translates to coil moving closer to the prostate once inserted into the rectal cavity.

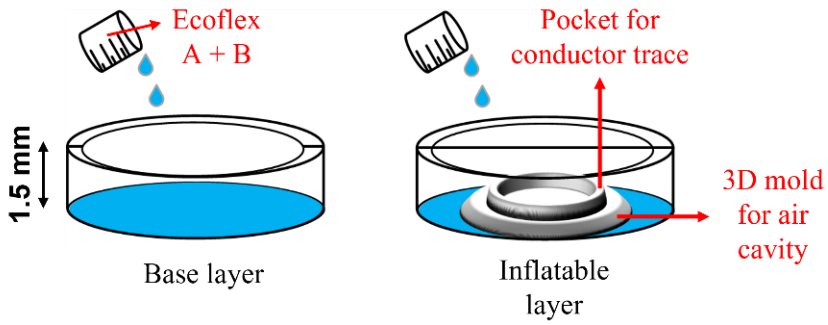

a)

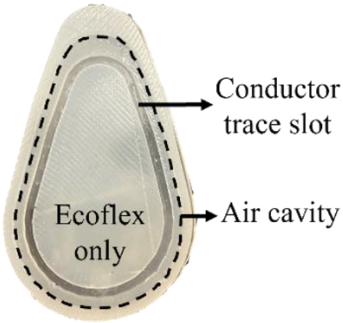

b)

Figure 4-6. a) Diagram explaining the process of fabricating the inflatable RF coil and (Bottom) conductor layer of the proposed inflatable RF coil for endorectal imaging and b) developed inflatable RF coil with Ecoflex showing inflation.

This cavity is sealed with another layer of Ecoflex substrate that has more stiffness compared to the first layer. Additionally, to maintain the inflation in one direction (towards the prostate) rather than inflation in all directions like current design we also embed a very thin plastic laminate sheet to the bottom layer. This stops the coil from overinflating on the side opposite to the prostate pushing the rectal wall away excessively thus resulting in patient discomfort and increased space between coil and prostate. Through this design we hypothesize that by moving the coil closer to the sample the overall SNR and image quality of the prostate region can be improved.

The reason for the oblong shape of the coil conductor which serves two purposes i) to create a mechanically strong entry point during insertion to the rectal cavity and retain the shape with minimum patient discomfort and ii) after maximum inflation the coil changes shape and size (expanding up to 25% of its diameter) thus creating a more circular design with increased average diameter. LM coil, when inflated stretches slightly at the diameter thus increasing the size of the coil and in turn slightly enhancing the penetration depth of the coil. We also hypothesize that by placing a flexible and elastic RF coil so closely to the prostate we can observe a similar SNR to the copper counterpart by using lesser RF transmit power thus making it more cost effective and reducing patient risk.

In section 4.3 we show various bench test results and MR images of a prostate phantom designed in lab to show feasibility of our design and validate our hypothesis.

4.2.3 Prostate Phantom design

To validate the inflatable coil performance using MR images, a prostate phantom was developed using ground meat and saline/gel sample. A 3D printed cylindrical tube of 32 mm radius was used at the outer shell of the prostate phantom with an ellipsoid shape representing the rectal cavity, as shown in Fig 4-7 a). The height of the phantom is 60 cm such that the inflatable coil can be fully housed inside the rectal cavity. The rectal cavity is designed to be open as shown in Fig 4-7 b) with a maximum inflatable space of 25 mm. This allows the coil to be inserted without resistance and reduces design complexity of making the cavity with a collapsible wall. In real world scenario, the rectal cavity is closed and the RF coil upon insertion creates a maximum opening of 22-27 mm as designed for this project. At 400 MHz prostate has respective electrical properties, conductivity of 1.03 S/m and permittivity of 63.4 F/m [148]. For the above mentioned electrical, 0.42g NaCl, 10.1g Sugar, 0.22g Agar are mixed with distilled water to create this saline gel of 25 ml representing the prostate.

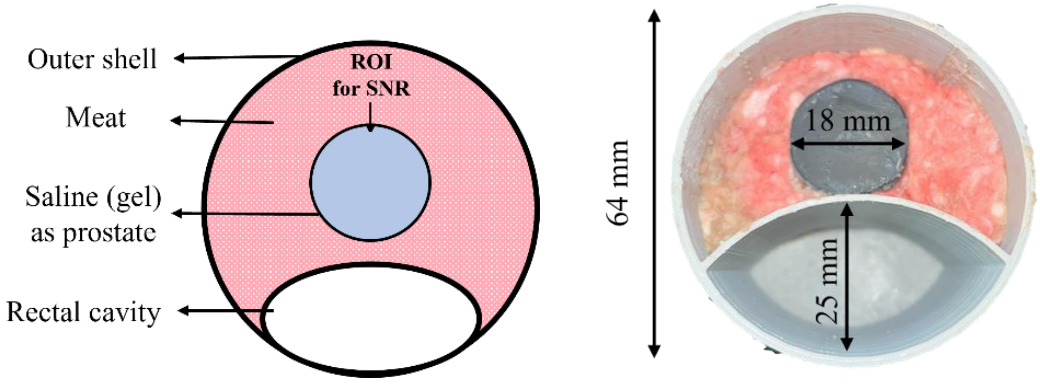

a) b)

Figure 4-7. a) diagram of the designed prostate phantom and b) picture of the prostate phantom with ground meat and agar gel

4.3 System level testing of inflatable RF coil along with SWIM

A two-port VNA (FieldFox N9923A, Keysight Technologies, USA) was used to measure the S-parameters of the proposed inflatable RF coil with a saline phantom for different inflation volumes. The impact of inflation on coil frequency response based on the volume of air inside the cavity is displayed in Fig.4-7 a). Higher resistivity (ρ = 2.9x10-7 Ω.m) of the liquid metal causes the antenna to have lower quality factor (Q-factor) and a wider bandwidth compared to copper RF coil.

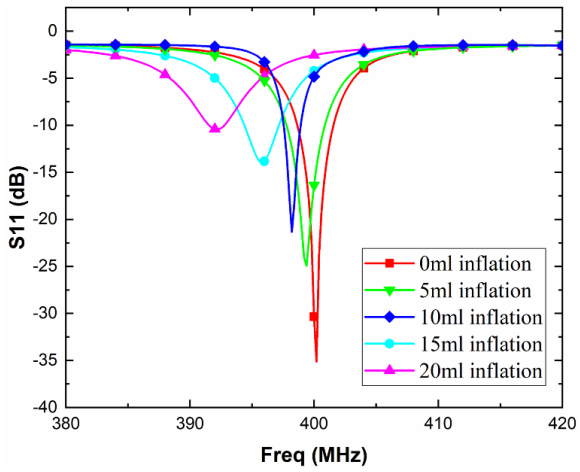

a)

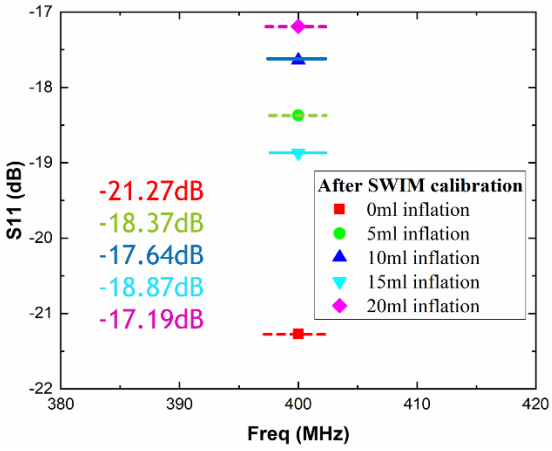

b)

Figure 4-8. a) Return loss plot of the loaded (placed inside prostate phantom) Ecoflex inflatable RF coil for different levels of inflation and b) Return loss plot of the loaded Ecoflex inflatable RF coil with SWIM calibration

A wireless pneumatic actuator is used to push air into the substrate via a syringe. This technique provides precise control over the volume of inflation and allows the user to quickly inflate and deflate the substrate. This also works alongside the manual impedance matching of the coil by placing the resonance in the approximate region of the central frequency based on inflation level. By inflating the coil and moving closer to the sample, zones SNR has been observed to increase. The proposed inflatable substrate can also create immobilization to reduce the motion artifact in images due to breathing. Endocavity antenna have been shown to improve the SNR in prostate imaging but are prone to compression artifact of the gland itself and lower posterior SNR of the prostate gland [146].

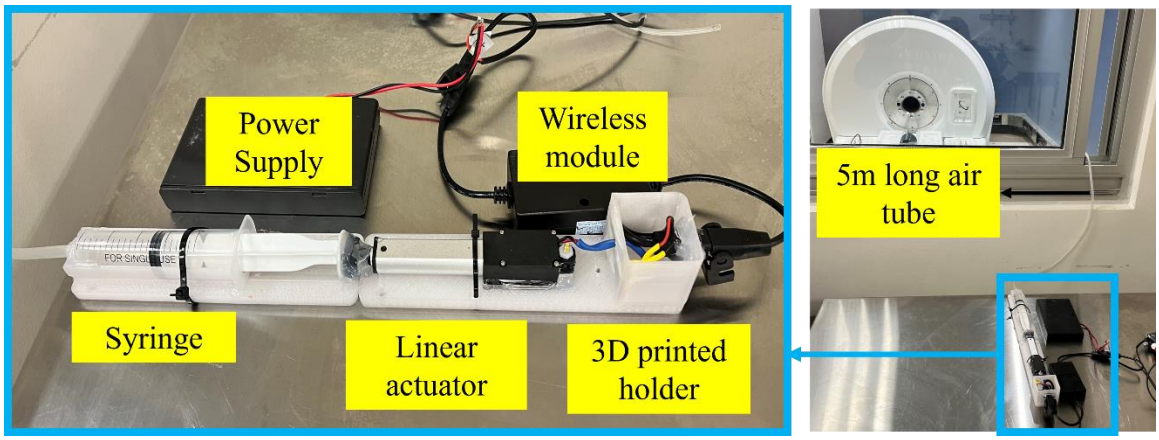

Figure 4-9. Wireless linear actuator with syringe to push and pull air from inflatable coil. (Inset) Detailed image of the linear actuator set up with syringe and air tube.

4.3.1 MR images

The 9.4T MR imaging study was conducted in a cryogen-free, 17 cm horizontal-bore dry magnet MRI scanner that allows small animal imaging at multiple field strengths (3T, 7T, or 9.4T) with gradient strengths of up to 2000 mT/m. The scanner console has a built-in hybrid coupler with two outputs 90° apart in phase. The coil is connected to one output and the other is terminated in 50 Ω with a high-power attenuator. This allows the proposed design to work as a transmit-receive RF coil. A Fast-Low-Angle-Shot (FLASH) Sequence with a repetition time (TR) of 400 ms, echo time (TE) of 5.4 ms, and a flip angle (α) of 25° was used for both MR imaging experiments. A field-of-view (FOV) of 60 x 60 mm and 256 x 256 matrix leading to an in-plane resolution of 234 x 234 μm, in addition 10 slices were acquired along the sample with a slice thickness of 1 mm and a slice gap of 0.1 mm. All the parameters for the imaging sequences were kept same, pre and post inflation, including the receiver gain to accurately validate the performance of the inflatable RF coil. ROIs are defined as shown in Fig.4-4. SNR of the ROI is calculated as the ratio of mean signal of ROI to the standard deviation of noise. The raw values of SNR are converted to dB scale and displayed in individual MR images. Fig.4-9, the MR images acquired before (left) and after (right) inflation at 400 MHz with LM coil are displayed. The change in frequency response after inflating the RF coil is compensated for by the SWIM system by adjusting the capacitor values in the PIN diode array before the imaging sequence to get maximum SNR.

Preliminary MR imaging was conducted using a cherry tomato to show feasibility and confirm the claim that inflation of liquid metal RF coil improves the SNR and image

quality, as shown in Fig 4-9 a). The mean signal intensity of the tomato has improved after inflation in the top-bottom direction as shown in Fig 4-9 b).

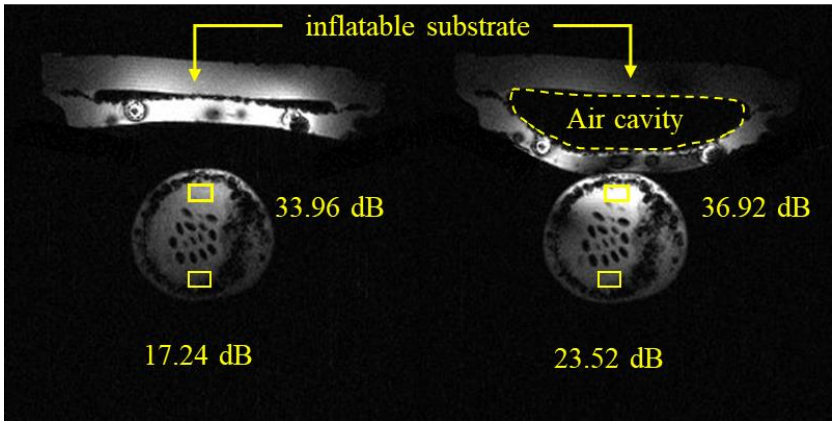

a)

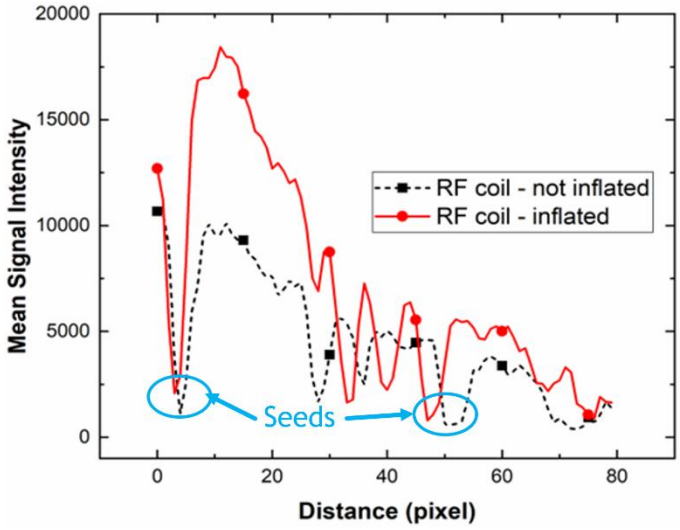

b)

Figure 4-10. MR image showing feasibility of the inflation in RF coil along with SNR values (dB) of the anterior and posterior regions of cherry tomato

Now we used the prostate phantom with saline solution along with manual tuning and matching to get MR images at different inflations levels as shown in Fig4-10 a) with 100W RF input power. Every time the coil is inflated the impedance matching is

performed manually by changing the variable capacitors on the L-matching network board. The SNR from the saline phantom (ROI is full saline phantom) is mentioned in individual images. We can see an increase in SNR from 24.24dB without any inflation of RF coil to 33.98dB with 20ml (maximum) inflation. This increase in SNR corresponds directly to the increase in the B_1 penetration depth of the coil calculated from these images at no inflation and maximum inflation.

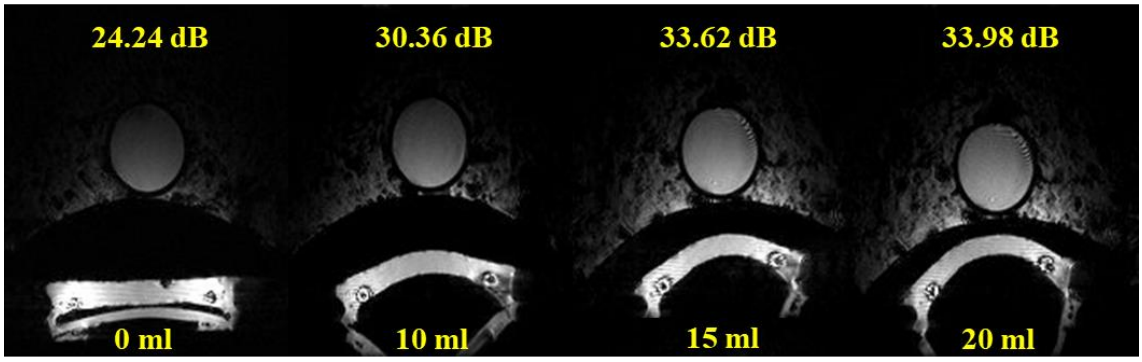

a)

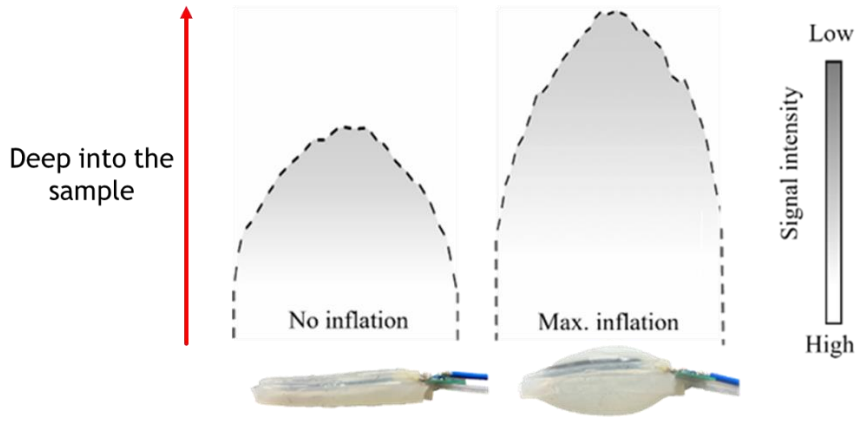

b)

Figure 4-11. a) 1ch inflatable RF coil images with prostate phantom used as transmit-receive coil and b) Inflatable coil B1 penetration profile before and after inflation

Acquiring a before and after SWIM calibration image in the case of an inflatable RF coil is not possible as the resonance is shifted quite drastically based on loading and inflation as seen earlier in bench test data. Therefore, we integrated the SWIM system with the inflatable coil and gathered MR images. Firstly, we reduced the input power from 100W to 31.6W (5 dBm reduction) to see the impact of inflatable design in low power scenarios as prostate imaging with high input power may cause patient safety concerns. FLASH sequence with same parameters was set up to acquire MR images shown in Fig 4-11 a) except for reduced RF input power.

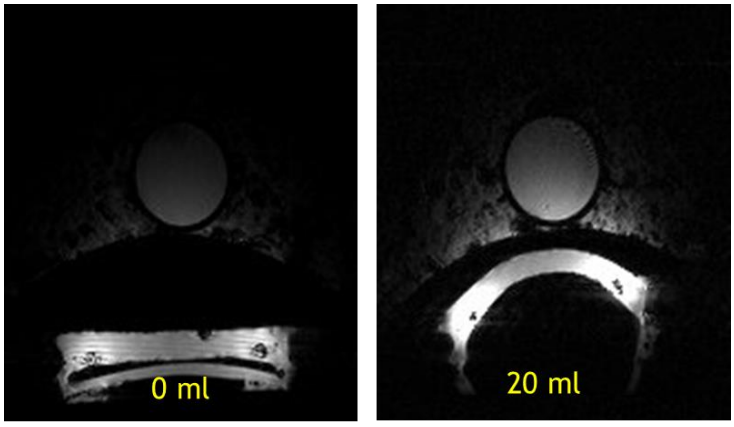

a)

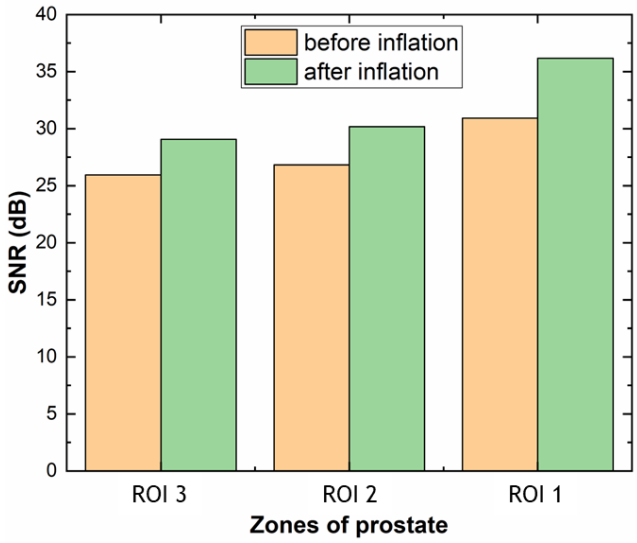

b)

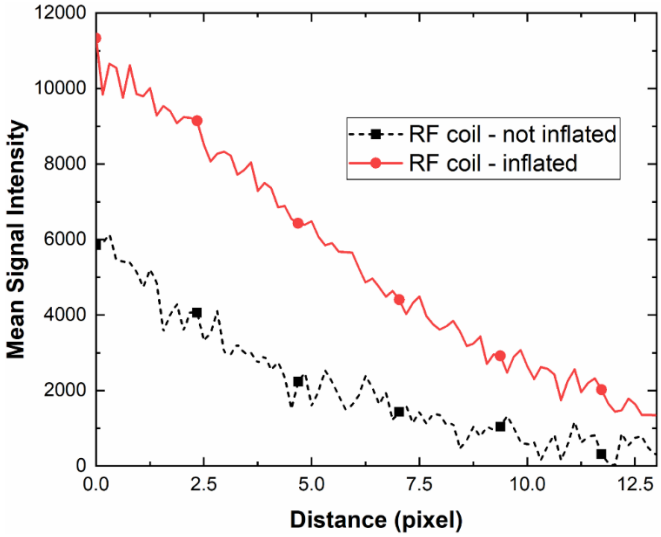

c)

Figure 4-12. a) MR images acquired of saline sample using inflatable RF coil integrated with SWIM system, b) SNR plot of the 3 different ROIs before and after inflation and c) Mean signal intensity of the MR images (vertically from top to bottom of phantom) before and after inflation and SWIM calibration

An increase in SNR in all three regions can be observed as shown in Fig 4-11 b) after inflation and automatic calibration by the SIWM system. In ROI 1, SNR increase from 33.98 dB to 39.63 dB was observed as this is the closest to the coil. In ROI 2 and ROI 3, we observed a change in SNR from 30.36 dB to 34 dB and 29.34 dB to 32.33 dB respectively.

Secondly, saline-gel sample was created by adding 0.22g of Agar to the saline solution and increased the diameter of the prostate to better represent the prostate phantom. The overall volume of the prostate was kept at 25ml with 18mm diameter and 25mm height of cylindrical phantom. MR images were acquired after integrating the SWIM system with inflatable RF coil using same sequence parameters as mentioned above at 31.6W.

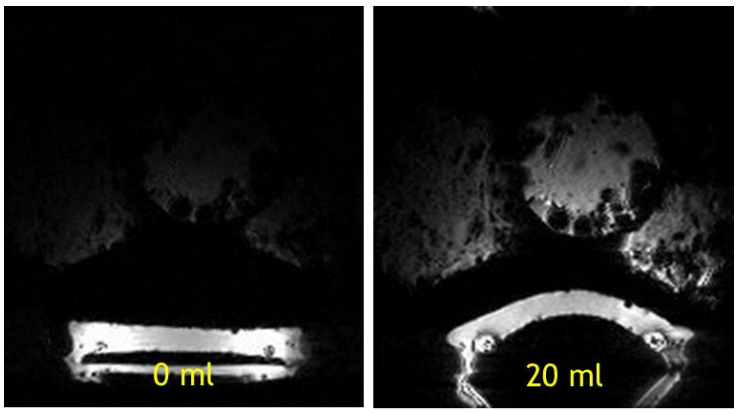

a)

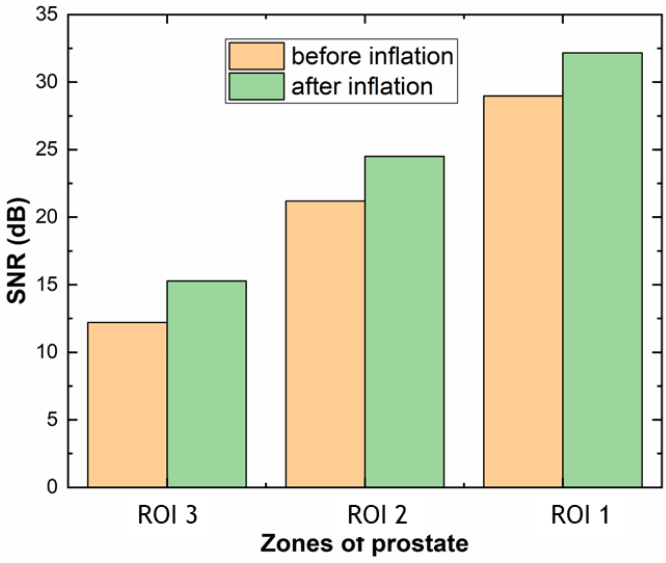

b)

Figure 4-13. a) MR images of saline gel phantom using inflatable RF coil integrated with SWIM system and b) SNR plot of 3 different ROIs before and after inflation

For the same input power and pulse sequence parameters, a bigger phantom creates a bigger loading effect thus impacting the impedance of the coil much more. This test was performed to validate the performance of the integrated system that can tune and match different sizes of samples while improving the SNR after inflation. In ROI 1, SNR increase from 28.97 dB to 34.16 dB was observed as this is the closest to the coil. In ROI 2 and ROI 3, we observed a change in SNR from 21.2 dB to 25.01 dB and 12.2 dB to 15.28 dB respectively.

Lastly, we used the same sample and RF coil integrated with SWIM system to acquire MR images using a Fast Spin Echo (FSE) sequence to validate the performance of the proposed system. With a TR of 4000ms and TE of 100ms, a field-of-view (FOV) of 50 x 50 mm and 256 x 256 matrix leading to an in-plane resolution of 234 x 234 μm,

in addition 10 slices were acquired along the sample with a slice thickness of 1 mm and a slice gap of 0.1 mm were set as imaging parameters for this scan.

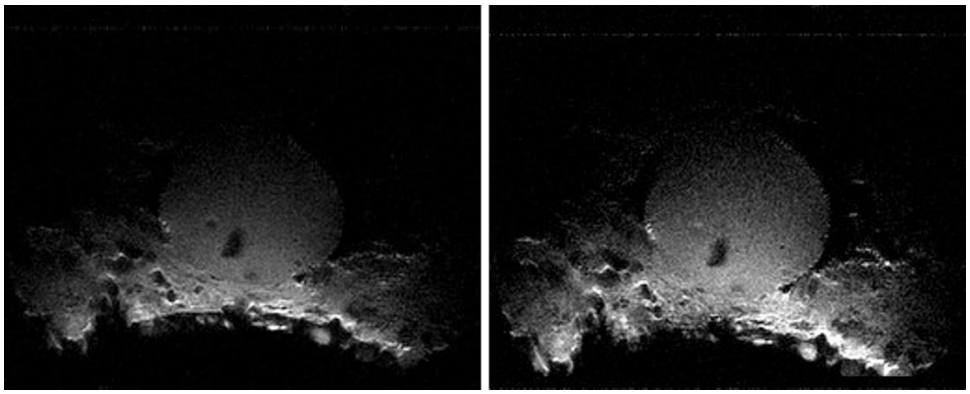

a)

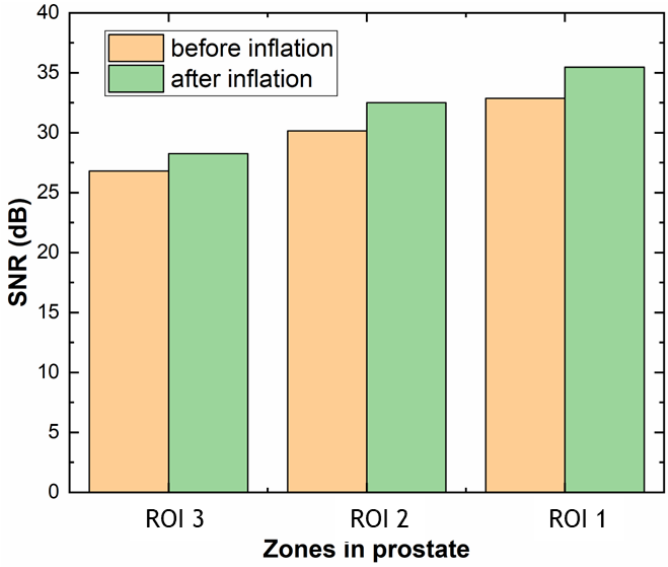

b)

Figure 4-14. Fast Spin Echo sequence MR images of Agar gel-based prostate phantom using Ecoflex inflatable coil before inflation (left) after inflation (right) and b) SNR plot of 3 different ROIs before and after inflation

In this experiment the saline-gel phantom was redeveloped to reduce air-bubbles during manufacturing as shown in Fig 4-13 a) as compared to previous experiment Fig 4-12 a).

In ROI 1, SNR increase from 30.86 dB to 35.47 dB was observed as this is the closest to the coil. In ROI 2 and ROI 3, we observed a change in SNR from 30.15 dB to 32.50 dB and 26.79 dB to 28.25 dB respectively. We have successfully demonstrated the proposed inflatable RF coil and integrated it with the SWIM system for automatic impedance matching after inflation. In three different experiments we have seen the inflating and impedance matching the RF coil has improved the SNR in all three ROIs of the prostate phantom as claimed in hypothesis. In all three experiments, an average increase in SNR of 10% in ROI 1, 19% in ROI 2 and 25% in ROI 3 was observed.

CHAPTER 5

CONCLUSION

5.1 Summary

In this dissertation two projects were addressed with the focus on automating the impedance matching of RF coils in MRI. We designed a novel elastic and inflatable RF coil towards endorectal prostate imaging using liquid metal (eGaIn) and silicon polymer substrate. We developed a wireless automatic impedance matching system to compensate for loading effect and change in coil dimension due to stretching and enlargement using capacitor arrays. A low-power system with MEMS switch capacitor array was designed as a general-purpose impedance matching module for receive coils. A high-power system built with PIN diodes was developed to compensate for the loading effect and stretching of RF coils used as transceive coils. Android-powered smart systems are a valuable next step for MRI research. We demonstrated that through a smart RF coil tuning and matching system. Integrating crucial RF systems and making them open source greatly accelerates research in the MRI community, as it allows performance evaluation of non-commercial (developed in lab) RF coils irrespective of scanner limitations. WE have shown a 10%, 19%, and 25% increase in SNR of three different ROIs in the prostate phantom imaging by combining SWIM system with inflatable RF coil. Bringing together the inflatable RF coil and the SWIM system as proposed will be a leading step towards the next generation of MRI RF coil systems and a driving force for the community to look at patient comfort without sacrificing the quality of diagnosis.

5.2 Future work

The design philosophy behind this general-purpose system is to create an open-source available automatic impedance matching system that can be scaled between field strengths and modified according to user specific needs. This automatic impedance matching system is modular in nature and can be expanded to a multichannel scenario to be used with a phased array receive coil. With multi-channel scaling the software upgrade such as changing the brute force algorithm of SWIM system to mathematical based minima finding algorithms such as Hill-climb technique. A large sample of loading conditions would provide training data for above mentioned techniques along with providing a preset state for the SWIM system to reduce the time it takes to tune and match each channel. Although built as a general-purpose system, the current version is restricted to pre-scan calibration and calibration between scan sequences. This leaves us with uncertain impedance matching condition during the scan that is caused due to patient movement. This method can be explored by looking deeply at the RF pulse time (duty cycle), transient time after switching capacitor state, and signal acquisition time for various pulse sequences.

The idea of inflatable RF coil can be used for other imaging such as pediatric imaging, head imaging, and extremities like knee, wrist, and ankle imaging. Inflatable designs can also conform to irregular anatomy like ankle, shoulder, wrist etc. More importantly inflatable substrate with elastic RF antennas can be a gateway for next generation endocavity RF antennas. Inflatable RF coil can also be used as motion restricted coil design in infant MRI scans. Prostate RF coil with liquid metal can be

further studied to improve mechanical design to further evaluate for patient safety concerns. Thermal analysis of the liquid metal coil for various pulse sequences is another step in the direction of liquid metal transmit-receive RF coils in MRI.

REFERENCES

[1] Bloch, F. (1946). Nuclear induction. Physical Review, 70(7–8), 460–474. https://doi.org/10.1103/physrev.70.460

[2] Purcell, E. M., Torrey, H. C., & Pound, R. V. (1946). Resonance absorption by nuclear magnetic moments in a solid. Physical Review, 69(1–2), 37–38. https://doi.org/10.1103/physrev.69.37

[3] Hahn, E. L. (1950). Spin echoes. Physical Review, 80(4), 580–594. https://doi.org/10.1103/physrev.80.580

[4] Damadian, R. (1971). Tumor detection by nuclear magnetic resonance. Science, 171(3976), 1151–1153. https://doi.org/10.1126/science.171.3976.1151

[5] Southwest Diagnostic Imaging Center (2020, November 20). Things You Should Know Before an MRI Scan. Diagnostic Imaging, MRI. https://swdic.com/posts/things-you-should-know-before-an-mri-scan/

[6] Bryant, T. (2023, March 27). Bath Community Hospital Acquires a new state-of-the-art X-Ray Machine - Bath Community Hospital. Bath Community Hospital. https://bathhospital.org/bath-community-hospital-acquires-new-state-of-the-art-x-ray-machine/

[7] GE Optima CT660 CT Scanner - Avante Health Solutions. (n.d.). https://avantehs.com/p/ge-optima-ct660-ct-scanner/13800

[8] Lauterbur, P. C. (1973). Image formation by induced local interactions: Examples employing nuclear magnetic resonance. Nature, 242(5394), 190–191. https://doi.org/10.1038/242190a0

[9] Nishimura, D. G. (2010). Principles of magnetic resonance imaging. In Stanford University eBooks. http://ci.nii.ac.jp/ncid/BB12402079

[10] Vaughan, J. T., & Griffiths, J. R. (2012). RF coils for MRI. John Wiley & Sons.

[11] Jin, J. (2018). Electromagnetic analysis and design in magnetic resonance imaging. In Routledge eBooks. https://doi.org/10.1201/9780203758731

[12] Marzola, P., Osculati, F., & Sbarbati, A. (2003). High field MRI in preclinical research. European Journal of Radiology, 48(2), 165–170. https://doi.org/10.1016/j.ejrad.2003.08.007

[13] Robitaille, P., & Berliner, L. (2007). Ultra-high field magnetic resonance Imaging. Springer Science & Business Media.

[14] Duyn, J. H. (2012). "The future of ultra-high field MRI and fMRI for study of the human brain." Neuroimage 62(2): 1241-1248.

[15] Schick, F. (2005). "Whole-body MRI at high field: technical limits and clinical potential." European radiology 15(5): 946-959.

[16] Blamire, A. M. (2008). "The technology of MRI: the next 10 years?" Br J Radiol 81(968): 601-617.

[17] Dai, J. (2006). Opportunities and Challenges of MRI in the Developing World ISMRM: 2.

[18] Wada, H., M. Sekino, et al. (2010). "Prospect of High-Field MRI." Applied Superconductivity, IEEE Transactions on 20(3): 115-122.

[19] Preclinical MRI 7.0T, cryogen-free superconducting dry magnet. (2022, October 14). MR Solutions. https://www.mrsolutions.com/mr-imaging/mr-imaging/mr-dry-magnet-cryogen-free/mr-7t/

[20] Newsroom | GE Healthcare. (n.d.). https://www.gehealthcare.com/about/newsroom/press-releases/setting-helium-free-revolutionary-mri-tech-ge-healthcare

[21] K. P. Pruessmann, M. Weiger, M. B. Scheidegger, and P. Boesiger, "SENSE: sensitivity encoding for fast MRI," Magn Reson Med, vol. 42, pp. 952-62, 1999

[22] M. A. Griswold, P. M. Jakob, R. M. Heidemann, M. Nittka, V. Jellus, J. Wang, et al., "Generalized autocalibrating partially parallel acquisitions (GRAPPA)," Magn Reson Med, vol. 47, pp. 1202-10, 2002.

[23] M. Lustig, D. L. Donoho, J. M. Santos, and J. M. Pauly, "Compressed sensing MRI," Ieee Signal Processing Magazine, vol. 25, pp. 72-82, 2008.

[24] P. Caravan, J. J. Ellison, T. J. McMurry, and R. B. Lauffer, "Gadolinium(III) chelates as MRI contrast agents: Structure, dynamics, and applications," Chemical Reviews, vol. 99, pp. 2293-2352, Sep 1999.

[25] H. B. Na, I. C. Song, and T. Hyeon, "Inorganic Nanoparticles for MRI Contrast Agents," Advanced Materials, vol. 21, pp. 2133-2148, Jun 5, 2009.

[26] O. Ocali and E. Atalar, "Ultimate intrinsic signal-to-noise ratio in MRI," Magn

Reson Med, vol. 39, pp. 462-73, Mar 1998.

[27] P. B. Roemer, W. A. Edelstein, C. E. Hayes, S. P. Souza, and O. M. Mueller, "The NMR phased array," Magn Reson Med, vol. 16, pp. 192-225, 1990.

[28] F. Wiesinger, P. Boesiger, and K. P. Pruessmann, "Electrodynamics and ultimate SNR in parallel MR imaging," Magn Reson Med, vol. 52, pp. 376-90, Aug 2004.

[29] AIRTM. (n.d.). GE HealthCare (United States). https://www.gehealthcare.com/products/magnetic-resonance-imaging/air-technology

[30] Vincent, J. M., & Rispoli, J. V. (2019). Stitching Stretchable Radiofrequency Coils for MRI: A Conductive Thread and Athletic Fabric Approach. Annual International Conference of the IEEE Engineering in Medicine and Biology Society. IEEE Engineering in Medicine and Biology Society. Annual International Conference, 2019, 6798–6801. https://doi.org/10.1109/EMBC.2019.8857051

[31] Wang, B., Siddiq, S. S., Walczyk, J., Bruno, M., Khodarahmi, I., Brinkmann, I. M., Rehner, R., Lakshmanan, K., Fritz, J., & Brown, R. (2022). A flexible MRI coil based on a cable conductor and applied to knee imaging. Scientific reports, 12(1), 15010. https://doi.org/10.1038/s41598-022-19282-6

[32] Dale, B. M., Brown, M. A., & Semelka, R. C. (2015). MRI: Basic Principles and Applications. John Wiley & Sons.

[33] Bushong, S. C., & Clarke, G. D. (2015). Magnetic resonance imaging: Physical and Biological Principles. Mosby.

[34] De Graaf, R. A. (2019). In vivo NMR spectroscopy: Principles and Techniques. John Wiley & Sons.

[35] Schultz, W. (2022, January 4). But what is quantum spin? - Wilhelm Schultz - Medium. Medium. https://medium.com/@pelicanlabs/but-what-is-quantum-spin-de66e030e17e

[36] Gyromagnetic ratio (γ). (n.d.). Questions and Answers in MRI. https://mriquestions.com/gyromagnetic-ratio-gamma.html

[37] Wikipedia contributors. (2023b). Zeeman effect. Wikipedia. https://en.wikipedia.org/wiki/Zeeman_effect

[38] Jones, J. (2009). Larmor frequency. Radiopaedia.org. https://doi.org/10.53347/rid-5855

[39] Hoult, D. I., & Lauterbur, P. C. (1979). The sensitivity of the zeugmatographic experiment involving human samples. Journal of Magnetic Resonance, 34(2), 425–433. https://doi.org/10.1016/0022-2364(79)90019-2

[40] J. Kurhanewicz, D. B. Vigneron, K. Brindle, E. Y. Chekmenev, A. Comment, C. H. Cunningham, et al., "Analysis of cancer metabolism by imaging hyperpolarized nuclei: prospects for translation to clinical research," Neoplasia, vol. 13, pp. 81-97, Feb 2011.

[41] J. Ruiz-Cabello, B. P. Barnett, P. A. Bottomley, and J. W. Bulte, "Fluorine (19F) MRS and MRI in biomedicine," NMR Biomed, vol. 24, pp. 114-29, Feb 2011.

[42] J. B. Ra, S. K. Hilal, and C. H. Oh, "An algorithm for MR imaging of the short T2 fraction of sodium using the FID signal," J Comput Assist Tomogr, vol. 13, pp. 302-9, Mar-Apr 1989.

[43] D. I. Hoult, S. J. Busby, D. G. Gadian, G. K. Radda, R. E. Richards, and P. J. Seeley, "Observation of tissue metabolites using 31P nuclear magnetic resonance," Nature, vol. 252, pp. 285-7, Nov 22 1974.

[44] B. M. Goodson, "Nuclear magnetic resonance of laser-polarized noble gases in molecules, materials, and organisms," J Magn Reson, vol. 155, pp. 157-216, Apr 2002.

[45] MRI Basics. (n.d.). https://case.edu/med/neurology/NR/MRI%20Basics.htm

[46] T2* vs T2 relaxation time. (n.d.). Questions and Answers in MRI. https://mriquestions.com/t2-vs-t2.html

[47] Maxwell's Equations. (n.d.). http://hyperphysics.phy-astr.gsu.edu/hbase/electric/maxeq.html

[48] MR magnet types. (n.d.). Questions and Answers in MRI. https://mriquestions.com/types-of-magnets.html

[49] Koh, D., Lee, J. M., Bittencourt, L. K., Blackledge, M., & Collins, D. J. (2016). Body diffusion-weighted MR imaging in oncology. Magnetic Resonance Imaging Clinics of North America, 24(1), 31–44. https://doi.org/10.1016/j.mric.2015.08.007

[50] Vachha, B., & Huang, S. Y. (2021). MRI with ultrahigh field strength and high-performance gradients: challenges and opportunities for clinical neuroimaging at

7 T and beyond. European radiology experimental, 5(1), 35. https://doi.org/10.1186/s41747-021-00216-2

[51] Mripetctsource. (2023b). MRI gradient coil. MRIPETCTSOURCE. https://www.mripetctsource.com/mri-gradient-coil#:~:text=The%20gradient%20coil%20creates%20a,3D%20image%20of%20the%20body.

[52] Spatial encoding in MRI: magnetic field gradients | e-MRI. (n.d.). IMAIOS. https://www.imaios.com/en/e-mri/spatial-encoding-in-mri/magnetic-field-gradients

[53] DirectMed Parts & Service. (n.d.). All about gradient coils in magnetic resonance Imaging (MRI) - DirectMed Parts & Service. https://directmedparts.com/all-about-gradient-coils-in-magnetic-resonance-imaging-mri

[54] Collins, C. M. (2016). Fundamentals of MRI fields and basic pulse sequences. In Morgan & Claypool Publishers eBooks (pp. 1–24). https://doi.org/10.1088/978-1-6817-4083-6ch1

[55] MRI image formation: K-space exploration | e-MRI. (n.d.). IMAIOS. https://www.imaios.com/en/e-mri/mri-image-formation/k-space-exploration#:~:text=The%20k%2Dspace%20location%20(kx,the%20center%20of%20k%2Dspace.

[56] Murbach, M., Neufeld, E., Kainz, W., Pruessmann, K. P., & Kuster, N. (2013). Whole-body and local RF absorption in human models as a function of anatomy and position within 1.5T MR body coil. Magnetic Resonance in Medicine, 71(2), 839–845. https://doi.org/10.1002/mrm.24690

[57] Adair, E. R., & Black, D. R. (2003). Thermoregulatory responses to RF energy absorption. Bioelectromagnetics, 24(S6), S17–S38. https://doi.org/10.1002/bem.10133

[58] National Electrical Manufacturers Association. NEMA Standards Publication MS 8-2016. Characterization of the Specific Absorption Rate (SAR) for Magnetic Resonance Imaging Systems. https://www.nema.org/standards/Index/6f116c99-5c09-4ac1-b06f-13af4d8d0898/

[59] Nacher, P., Kumaragamage, S., Tastevin, G., & Bidinosti, C. P. (2020). A fast MOSFET rf switch for low-field NMR and MRI. Journal of Magnetic Resonance, 310, 106638. https://doi.org/10.1016/j.jmr.2019.106638

[60] Brunner, D. O., Furrer, L., Weiger, M., Baumberger, W., Schmid, T., Reber, J., Dietrich, B. E., Wilm, B. J., Froidevaux, R., & Pruessmann, K. P. (2016). Symmetrically biased T/R switches for NMR and MRI with microsecond dead time. Journal of magnetic resonance (San Diego, Calif. : 1997), 263, 147–155. https://doi.org/10.1016/j.jmr.2015.12.016

[61] Yazdanbakhsh, P., & Solbach, K. (2011). Microstrip Butler matrix design and realization for 7 T MRI. Magnetic resonance in medicine, 66(1), 270–280. https://doi.org/10.1002/mrm.22777

[62] Microwaves101 | Butler Matrix. (n.d.). https://www.microwaves101.com/encyclopedias/butler-matrix

[63] Cao, X., Fischer, E., Hennig, J., & Zaitsev, M. (2018). Direct matching methods for coils and preamplifiers in MRI. Journal of Magnetic Resonance, 290, 85–91. https://doi.org/10.1016/j.jmr.2018.03.009

[64] Gruber, B., Froeling, M., Leiner, T., & Klomp, D. W. J. (2018). RF coils: A practical guide for nonphysicists. Journal of magnetic resonance imaging : JMRI, 48(3), 590–604. Advance online publication. https://doi.org/10.1002/jmri.26187

[65] Zwart, N. R. (n.d.). (ISMRM 2015) Onboard RF combination for receiver channel reduction. https://archive.ismrm.org/2015/3139.html

[66] Darnell, D., Truong, T., & Song, A. W. (2021). Recent advances in Radio-Frequency Coil technologies: flexible, wireless, and integrated coil arrays. Journal of Magnetic Resonance Imaging, 55(4), 1026–1042. https://doi.org/10.1002/jmri.27865

[67] Birdcage RF coil. (n.d.). Questions and Answers in MRI. https://mriquestions.com/birdcage-coil.html

[68] Hayes CE, Edelstein WA, Schenck JF, Mueller OM, Eash M. An efficient, highly homogeneous radiofrequency coil for whole-body NMR imaging at 1.5 T. J Mag Reson 1985; 63: 622–628.

[69] Giovannetti, G., Landini, L., Santarelli, M.F. et al. A fast and accurate simulator for the design of birdcage coils in MRI. MAGMA 15, 36–44 (2002). https://doi.org/10.1007/BF02693842

[70] Ahmad, S. F., Kim, Y. C., Choi, I. C., & Kim, H. D. (2020). Recent Progress in Birdcage RF Coil Technology for MRI System. Diagnostics (Basel, Switzerland), 10(12), 1017. https://doi.org/10.3390/diagnostics10121017

[71] Santini, T., Zhao, Y., Wood, S., Krishnamurthy, N., Kim, J., Farhat, N., Alkhateeb, S., Martins, T., Koo, M., Zhao, T., Aizenstein, H. J., & Ibrahim, T. S. (2018). In-vivo and numerical analysis of the eigenmodes produced by a multi-level Tic-Tac-Toe head transmit array for 7 Tesla MRI. PloS one, 13(11), e0206127. https://doi.org/10.1371/journal.pone.0206127

[72] Pang, Y., Wong, E. W., Yu, B., & Zhang, X. (2014). Design and numerical evaluation of a volume coil array for parallel MR imaging at ultrahigh fields. Quantitative imaging in medicine and surgery, 4(1), 50–56. https://doi.org/10.3978/j.issn.2223-4292.2014.02.07

[73] Pang, Y., Xie, Z., Li, Y., Xu, D., Vigneron, D., & Zhang, X. (2011). Resonant Mode Reduction in Radiofrequency Volume Coils for Ultrahigh Field Magnetic Resonance Imaging. Materials (Basel, Switzerland), 4(8), 1333–1344. https://doi.org/10.3390/ma4081333

[74] Wang, C., Qu, P., & Shen, G. X. (2006). Potential advantage of higher-order modes of birdcage coil for parallel imaging. Journal of magnetic resonance (San Diego, Calif. : 1997), 182(1), 160–167. https://doi.org/10.1016/j.jmr.2006.06.015

[75] Graessl, A., Renz, W., Hezel, F., Dieringer, M.A., Winter, L., Oezerdem, C., Rieger, J., Kellman, P., Santoro, D., Lindel, T.D. and Frauenrath, T., 2014. Modular 32-channel transceiver coil array for cardiac MRI at 7.0 T. Magnetic resonance in medicine, 72(1), pp.276-290

[76] Thalhammer, C., Renz, W., Winter, L., Hezel, F., Rieger, J., Pfeiffer, H., Graessl, A., Seifert, F., Hoffmann, W., von Knobelsdorff-Brenkenhoff, F. and Tkachenko, V., 2012. Two-Dimensional sixteen channel transmit/receive coil array for cardiac MRI at 7.0 T: Design, evaluation, and application. Journal of Magnetic Resonance Imaging, 36(4), pp.847-857

[77] Hayes, C.E. and Axel, L., 1985. Noise performance of surface coils for magnetic resonance imaging at 1.5T. Medical physics, 12(5), pp. 604-607

[78] GE Healthcare. MR Field Notes: RF Coils...They've come a long, long way. 2005.

[79] Kumar A, Bottomley PA. Optimized quadrature surface coil designs. Magn Reson Mater Phy 2008; 21:41-52.

[80] J. l. Mispelter, M. Lupu, and A. Briguet, NMR probeheads for biophysical and biomedical experiments : theoretical principles & practical guidelines. London: Imperial College Press, Distributed by World Scientific, 2006.

[81] M. Rudin, In-Vivo Magnetic Resonance Spectroscopy I: Probeheads and Radiofrequency Pulses Spectrum Analysis. Berlin, Heidelberg: Springer Berlin Heidelberg,, 1992.

[82] Torrungrueng, D., & Mekathikom, T. (2015). Forbidden regions of L-section impedance matching networks on Meta-Smith charts for conjugately characteristic-impedance transmission lines. Microwave and Optical Technology Letters, 57(4), 874–879. https://doi.org/10.1002/mop.28977

[83] Vaughan, J. T., & Griffiths, J. R. (2012b). RF coils for MRI. John Wiley & Sons.

[84] Lee, R. F., Giaquinto, R. O., & Hardy, C. J. (2002). Coupling and decoupling theory and its application to the MRI phased array. Magnetic resonance in medicine, 48(1), 203–213. https://doi.org/10.1002/mrm.10186

[85] Sanchez-Heredia, J. D., Szocska Hansen, E. S., Laustsen, C., Zhurbenko, V., & Ardenkjær-Larsen, J. H. (2017). Low-Noise Active Decoupling Circuit and its Application to 13C Cryogenic RF Coils at 3 T. Tomography (Ann Arbor, Mich.), 3(1), 60–66. https://doi.org/10.18383/j.tom.2016.00280

[86] Yan, X., Gore, J. C., & Grissom, W. A. (2018). Self-decoupled radiofrequency coils for magnetic resonance imaging. Nature Communications, 9(1). https://doi.org/10.1038/s41467-018-05585-8

[87] Hurshkainen, A., Nikulin, A. V., Georget, É., Larrat, B., Berrahou, D., Neves, A. L., Sabouroux, P., Enoch, S., Melchakova, I. V., Belov, P. A., Glybovski, S., & Abdeddaïm, R. (2018). A novel Metamaterial-Inspired RF-Coil for preclinical Dual-Nuclei MRI. Scientific Reports, 8(1). https://doi.org/10.1038/s41598-018-27327-y

[88] Li, Y., Xie, Z., Pang, Y., Vigneron, D., & Zhang, X. (2011). ICE decoupling technique for RF coil array designs. Medical physics, 38(7), 4086–4093. https://doi.org/10.1118/1.3598112

[89] L. Sankey and Z. Popovic, “Adaptive tuning for handheld transmitters,” in Proc. IEEE MTT-S Int. Microw. Symp. Dig., 2009, pp. 225–228.

[90] J. De Mingo, A. Valdovinos, A. Crespo, D. Navarro, and P. Garcia, “An RF electronically controlled impedance tuning network design and its application to an antenna input impedance automatic matching system,” IEEE Trans. Microw. Theory Tech., vol. 52, pp. 489–497, 2004.

[91] J. Madic, P. Bretchko, Z. Shuyun, R. Shumovich, and R. McMorrow, “Accurate power control technique for handset PA modules with integrated directional

couplers,” in Proc. Radio Frequency Integrated Circuits Symp., 2003, pp. 715–718.

[92] H. Song, J. T. Aberle and B. Bakkaloglu, "A Mixed-Signal Matching State Search Based Adaptive Antenna Tuning IC," in IEEE Microwave and Wireless Components Letters, vol. 20, no. 10, pp. 581-583, Oct. 2010, https://doi.org/10.1109/LMWC.2010.2061222

[93] P. Sjoblom and H. Sjoland, "An adaptive impedance tuning CMOS circuit for ISM 2.4-GHz band," in IEEE Transactions on Circuits and Systems I: Regular Papers, vol. 52, no. 6, pp. 1115-1124, June 2005, https://doi.org/10.1109/TCSI.2005.849116

[94] G. Seigneuret, E. Bergeret and P. Pannier, "Auto-tuning in passive UHF RFID tags," Proceedings of the 8th IEEE International NEWCAS Conference 2010, 2010, pp. 181-184, https://doi.org/10.1109/NEWCAS.2010.5603749

[95] H. Wegleiter, B. Schweighofer, C. Deinhammer, G. Holler and P. Fulmek, "Automatic Antenna Tuning Unit to Improve RFID System Performance," in IEEE Transactions on Instrumentation and Measurement, vol. 60, no. 8, pp. 2797-2803, Aug. 2011, https://doi.org/10.1109/TIM.2011.2122390

[96] A. Mohan and S. Mondal, "An Impedance Matching Strategy for Micro-Scale RF Energy Harvesting Systems," in IEEE Transactions on Circuits and Systems II: Express Briefs, vol. 68, no. 4, pp. 1458-1462, April 2021, https://doi.org/10.1109/TCSII.2020.3036850

[97] P. Zhao, Y. Zheng and M. Glesner, "Automatic impedance matching in Microwave power harvesters," 6th Conference on Ph.D. Research in Microelectronics & Electronics, 2010, pp. 1-4.

[98] F. Hwang and D. I. Hoult, “Automatic probe tuning and matching,” Magn. Reson. Med., vol. 39, no. 2, pp. 214–222, 1998.

[99] Hirata, H., Yamaguchi, Y., Takahashi, T., & Luo, Z. W. (2003). Control characteristics of an automatic matching control system for in vivo EPR spectroscopy. Magnetic Resonance in Medicine, 50(1), 223–227. https://doi.org/10.1002/mrm.10487

[100] R. Pérez de Alejo, C. Garrido, P. Villa, I. Rodriguez, J. J. Vaquero, J. Ruiz-Cabello, and M. Cortijo, “Automatic tuning and matching of a small multifrequency saddle coil at 4.7 T,” Magn. Reson. Med., vol. 51, pp. 869–873, 2004.

[101] Muftuler, L. T., Gulsen, G., Sezen, K. D., & Nalcioglu, O. (2002). Automatic tuned MRI RF coil for multinuclear imaging of small animals at 3T. Journal of Magnetic Resonance, 155(1), 39–44. https://doi.org/10.1006/jmre.2002.2510

[102] S. -M. Sohn, L. DelaBarre, A. Gopinath and J. T. Vaughan, "Design of an Electrically Automated RF Transceiver Head Coil in MRI," in IEEE Transactions on Biomedical Circuits and Systems, vol. 9, no. 5, pp. 725-732, Oct. 2015, https://doi.org/10.1109/TBCAS.2014.2360383

[103] Mehmann, A., Vogt, C., Varga, M., Port, A., Reber, J., Marjanovic, J., Pruessmann, K. P., Sporrer, B., Huang, Q., & Troster, G. (2019). Automatic resonance frequency retuning of stretchable liquid metal receive coil for magnetic resonance imaging. IEEE Transactions on Medical Imaging, 38(6), 1420–1426. https://doi.org/10.1109/TMI.2018.2888959

[104] Jouda, M., Torres Delgado, S. M., Jouzdani, M. A., Mager, D., & Korvink, J. G. (2020). ArduiTaM: accurate and inexpensive NMR auto tune and match system. Magnetic Resonance, 1(1), 105–113. https://doi.org/10.5194/mr-1-105-2020

[105] Venook, R. D., Hargreaves, B. A., Gold, G. E., Conolly, S. M., & Scott, G. C. (2005). Automatic tuning of flexible interventional RF receiver coils. Magnetic Resonance in Medicine, 54(4), 983–993. https://doi.org/10.1002/mrm.20616

[106] M. Pavan and A. K. P. P. , “A modular automatic matching network system,” in Proc. 18th Int. Soc. Magnetic Resonance in Medicine Meeting, 2010, p. 647.

[107] Wu, S., Beck, B. L., Turner, W. J., Bashirullah, R., & Mareci, T. (2010). An Automatic Impedance Matching System for Multiple Frequency Coils. Proc. ISMRM, July, 3920.

[108] B. L. Beck, S. W. W. J. Turner, R. Bashirullah, and T. H. Mareci, “High Q reactive network for automatic impedance matching,” in Proc. 19th Int. Soc. Magnetic Resonance in Medicine Meeting, 2011, p. 1853.

[109] SK. Kandala, S. Sohn, “Wirelessly controlled stand-alone automatic RF tuning and matching system for preclinical imaging at 7T,” in Proc. 30th Int. Soc. Magn. Resonance Med., 2021, p. 2515

[110] M. Twieg, M. A. de Rooij and M. A. Griswold, "Active Detuning of MRI Receive Coils with GaN FETs," in IEEE Transactions on Microwave Theory and Techniques, vol. 63, no. 12, pp. 4169-4177, Dec. 2015, https://doi.org/10.1109/TMTT.2015.2495366

[111] Saha, S., Pricci, R., Koutsoupidou, M. et al. A smart switching system to enable automatic tuning and detuning of metamaterial resonators in MRI scans. Sci Rep 10, 10042 (2020). https://doi.org/10.1038/s41598-020-66884-z

[112] Kandala, S. K., & Sohn, S. (2022). Design of standalone wireless impedance matching (SWIM) system for RF coils in MRI. Scientific Reports, 12(1). https://doi.org/10.1038/s41598-022-26143-9

[113] Pozar, D. M. (2011). Microwave engineering. John Wiley & Sons.

[114] S. M. Sohn, A. Gopinath, and J. T. Vaughan, "Tunable and high directivity coupler for MRI applications," IEEE MTT-S Int. Microw. Symp. Dig., pp. 8–10, 2014, doi: https://doi.org/10.1109/MWSYM.2014.6848491

[115] S. M. Sohn, A. Gopinath, and J. T. Vaughan, "A Compact, High Power Capable, and Tunable High Directivity Microstrip Coupler," IEEE Trans. Microw. Theory Tech., vol. 64, no. 10, pp. 3217–3223, 2016, doi: https://doi.org/10.1109/TMTT.2016.260283 5

[116] M. Dydyk, "Accurate Design of Microstrip directional couplers with capacitive compensation," IEEE MTT-S Int. Microw. Symp. Dig., vol. 7, no. 1, pp. 37–72, 1990.

[117] M. Dydyk, "Microstripdirectional couplers with ideal performance via single-element compensation," IEEE Trans. Microw. Theory Tech., vol. 47, no. 6 PART 2, pp. 956–964, 1999, doi: https://doi.org/10.1109/22.769332

[118] K. Li, "FOR MICROWAVE INTEGRATED CIRCUITS," vol. 1, no. c, pp. 1041–1044, 1997.

[119] A. Alt, N. Schwerg, C. Wangler, and D. Gruner, "Concept for the implementation of very high directivity and decade bandwidth in compact microstrip directional couplers," Eur. Microw. Week 2016 "Microwaves Everywhere", EuMW 2016 - Conf. Proceedings; 46th Eur. Microw. Conf. EuMC 2016, pp. 210–213, 2016, doi: https://doi.org/10.1109/EuMC.2016.7824315

[120] L. Su, T. Itoh, and J. Rivera, "Design of an Overlay Directional Coupler by a Full-Wave Analysis," IEEE Trans. Microw. Theory Tech., vol. 31, no. 12, pp. 1017–1022, 1983, doi: https://doi.org/10.1109/TMTT.1983.1131655

[121] J. L. Chen, S. F. Chang, and C. T. Wu, "A high-directivity microstrip directional coupler with feedback compensation," IEEE MTT-S Int. Microw. Symp. Dig., vol. 1, pp. 101–104, 2002, doi: https://doi.org/10.1109/mwsym.2002.1011569

[122] Dubois M, Vergara Gomez TS, Jouvaud C, et al. Enhancing surface coil sensitivity volume with hybridized electric dipoles at 17.2 T. J Magn Reson2019;307:106567

[123] Garwood M, Uğurbil K. RF pulse methods for use with surface coils: Frequency-modulated pulses and parallel transmission. J Magn Reson. 2018 Jun;291:84-93. doi: https://10.1016/j.jmr.2018.01.012 Epub 2018 Apr 26. PMID: 29705035; PMCID: PMC5943143

[124] D. Hoult et al. "The NMR receiver: a description and analysis of design" Prog. Nucl. Magn. Reson. Spectrosc., 12 (1978), pp. 41-77.

[125] Hernandez D, Kim KN. A Review on the RF Coil Designs and Trends for Ultra High Field Magnetic Resonance Imaging. Investig Magn Reson Imaging. 2020 Sep;24(3):95-122. https://doi.org/10.13104/imri.2020.24.3.95

[126] Malko JA, McClees EC, Braun IF, Davis PC, Hoffman JC Jr. A flexible mercury-filled surface coil for MR imaging. AJNR Am J Neuroradiol. 1986 Mar-Apr;7(2):246-7. PMID: 3082157; PMCID: PMC8332679.

[127] Ruytenberg, T., Webb, A.G., & Zivkovic, I. (2019). Shielded-coaxial-cable coils as receive and transceive array elements for 7T human MRI. Magnetic Resonance in Medicine, 83, 1135 - 1146.

[128] J. R. Corea et al., "Screen-printed flexible MRI receive coils," Nature Commun., vol. 7, Mar. 2016, Art. no. 10839

[129] D. Mager et al., "An MRI receiver coil produced by inkjet printing directly on to a flexible substrate," IEEE Trans. Med. Imag., vol. 29, no. 2, pp. 482–487, Feb. 2010.

[130] A. Mehmann et al., "On the bending and stretching of liquid metal receive coils for magnetic resonance imaging," IEEE Trans. Biomed. Eng., to be published, doi: https://10.1109/TBME.2018.2875436

[131] Mehmann A, Vogt C, Varga M, Port A, Reber J, Marjanovic J, Pruessmann KP, Sporrer B, Huang Q, Troster G. Automatic Resonance Frequency Retuning of Stretchable Liquid Metal Receive Coil for Magnetic Resonance Imaging. IEEE Trans Med Imaging. 2019 Jun;38(6):1420-1426. doi: https://10.1109/TMI.2018.2888959 Epub 2018 Dec 20. PMID: 30582533.

[132] M. Varga et al., "Adsorbed eutectic gain structures on a neoprene foam for stretchable MRI coils," Adv. Mater., vol. 29, no. 44, p. 1703744, 2017, doi: https://10.1002/adma.201703744

[133] B. Kahraman-Agir, K. Yegin and E. Ozturk-Isik, "Wearable and Elastic Surface Coil for 1H Magnetic Resonance Imaging," in IEEE Microwave and Wireless Components Letters, vol. 31, no. 5, pp. 517-520, May 2021, doi: https://10.1109/LMWC.2021.3068930

[134] G. J. Hayes, J. So, A. Qusba, M. D. Dickey and G. Lazzi, "Flexible Liquid Metal Alloy (EGaIn) Microstrip Patch Antenna," in IEEE Transactions on Antennas and Propagation, vol. 60, no. 5, pp. 2151-2156, May 2012, doi: https://10.1109/TAP.2012.2189698

[135] Motovilova, E., Tan, E.T., Taracila, V. et al. Stretchable self-tuning MRI receive coils based on liquid metal technology (LiquiTune). Sci Rep 11, 16228 (2021). https://doi.org/10.1038/s41598-021-95335-6

[136] Pérez de Alejo, R. et al. Automatic tuning and matching of a small multifrequency saddle coil at 4.7 T. Magn. Reson. Med. 51, 869–873 (2004).

[137] Muftuler, L. T., Gulsen, G., Sezen, K. D. & Nalcioglu, O. Automatic tuned MRI RF coil for multinuclear imaging of small animals at 3T. J. Magn. Reson. 155(1), 39–44. https://doi.org/10.1006/jmre.2002.2510 (2002).

[138] Sohn, S.-M., DelaBarre, L., Gopinath, A. & Vaughan, J. T. Design of an electrically automated RF transceiver head coil in MRI. IEEE Trans. Biomed. Circuits Syst. 9(5), 725–732. https://doi.org/10.1109/TBCAS.2014.2360383 (2015).

[139] Jouda, M., Torres Delgado, S. M., Jouzdani, M. A., Mager, D. & Korvink, J. G. ArduiTaM: accurate and inexpensive NMR auto tune and match system. Magn. Reson. 1(1), 105–113. https://doi.org/10.5194/mr-1-105-2020 (2020).

[140] Venook, R. D., Hargreaves, B. A., Gold, G. E., Conolly, S. M. & Scott, G. C. Automatic tuning of flexible interventional RF receiver coils. Magn. Reson. Med. 54(4), 983–993.

[141] Wu, S., Beck, B. L., Turner, W. J., Bashirullah, R., & Mareci, T. An automatic impedance matching system for multiple frequency coils. In Proc. ISMRM, July, 3920 (2010).

[142] McVeigh ER, Henkelman RM, Bronskill MJ. Noise and filtration in magnetic resonance imaging. Med Phys. 1985;12(5):586-591. doi:10.1118/1.595679

[143] F. L. Goerner and G. D. Clarke, “Measuring signal-to-noise ratio in partially parallel imaging MRI,” Med. Phys., vol. 38, no. 9, pp. i5049–5057, 2011, doi: 10.1118/1.3618730.

[144] Henkelman RM. Measurement of signal intensities in the presence of noise in MR images. Med Phys. 1985 Mar-Apr;12(2):232-3. doi: 10.1118/1.595711. PMID: 4000083.

[145] Zones of the prostate | SEER training. (n.d.). https://training.seer.cancer.gov/prostate/anatomy/zones.html

[146] Lee, G. H., Oto, A., & Giurcanu, M. (2022). Prostate MRI: Is Endorectal Coil Necessary?—A review. Life, 12(4), 569. https://doi.org/10.3390/life12040569

[147] Oh, W. K. (2003). Biology of Prostate Cancer. Holland-Frei Cancer Medicine - NCBI Bookshelf. https://www.ncbi.nlm.nih.gov/books/NBK13217/#:~:text=There%20are%20four%20major%20zones,(Figure%20111%2D4).

[148] Dielectric properties » IT'IS Foundation. (n.d.-b). https://itis.swiss/virtual-population/tissue-properties/database/dielectric-properties/